TRANSMISSION DIFFRACTION GRATINGS FOR SOFT X-RAY SPECTROSCOPY AND SPATIAL PERIOD DIVISION

by

ANDREW MICHAEL HAWRYLUK

S.B. MASSACHUSETTS INSTITUTE OF TECHNOLOGY
(1977)

S.M. MASSACHUSETTS INSTITUTE OF TECHNOLOGY
(1977)

SUBMITTED IN PARTIAL FULFILLMENT OF THE REQUIREMENTS

FOR THE DEGREE OF

DOCTOR OF PHILOSOPHY

at the

MASSACHUSETTS INSTITUTE OF TECHNOLOGY

Signature of Author .....
Department of Electrical Engineering and Computer Science,
October 23, 1981

Certified by .....
Thesis Supervisor

Accepted by .....
Chairman, Department Committee on Graduate Students

TRANSMISSION DIFFRACTION GRATINGS

FOR SOFT X-RAY SPECTROSCOPY AND SPATIAL PERIOD DIVISION

by

ANDREW MICHAEL HAWRYLUK

SUBMITTED TO THE DEPARTMENT OF ELECTRICAL ENGINEERING AND COMPUTER SCIENCE ON OCTOBER 23, 1981, IN PARTIAL FULFILLMENT OF THE REQUIREMENTS FOR THE DEGREE OF DOCTOR OF PHILOSOPHY

ABSTRACT

Thick gold transmission diffraction gratings with spatial periods of 0.3 μm and 0.2 μm have been fabricated with thickness of 0.65 μm and 0.25 μm, respectively. These transmission gratings have a wide variety of applications, and have been used in x-ray spectroscopy and x-ray spatial period division. Fabrication techniques for these gratings include holographic lithography, "shadowing", x-ray lithography and gold microplating.

To demonstrate the use of these gratings to x-ray spectroscopy, a 0.3 μm period grating was coupled to a 22x Wolter type x-ray microscope, with $\sim$ 1 μm resolution, to produce a high resolution imaging spectrometer. At a wavelength of 0.69 nm, a spectral resolving power, $\lambda/\Delta\lambda$, of >200 was demonstrated. In this experiment, the measured resolving power was source size limited. The transmission diffraction efficiency (ratio of energy in one first order beam relative to the energy in the zeroth order diffracted beam) at λ = 0.69 nm was measured to be 100% ± 10%. This high efficiency was the result of the transmission and phase shift through the partially opaque gold grating lines.

The technique of spatial period division has the ability to produce a grating of period p/m, from a grating of period p (where "m" is an integer) by recording the near field diffraction pattern of the original ("parent") grating. An analysis of the near field diffraction pattern of a 200 nm period grating was performed and used to optimize the characteristics of the original grating to produce a spatial period division. Using this technique, a 99.5 nm period grating in PMMA was recorded using soft x-rays and also deep UV as the source of radiation. Fabrication of gratings with smaller spatial periods appears possible.

TABLE OF CONTENTS

LIST OF FIGURES

LIST OF SYMBOLS

A	Area of x-ray lithography masks
$A_o(k_x)$	Fourier transform of the electric field pattern at the plane of the grating
B_n	Fourier series coefficients
b	The amplitude, at $z = 0$, of the electric field transmitted through the thick gold grating lines
C_K	The carbon-K x-ray ($\lambda = 4.48$ nm)
C_m	Mask-substrate capacitance
C_n	Fourier series coefficients of a trial function
D	X-ray source to sample distance in x-ray lithography replications
d	X-ray source size, for replication purposes
d.o.f.	Depth of field of a spatial period division image
$\varepsilon_1(x)$	Electric field pattern of a trial function
$\varepsilon_2(x)$	Electric field pattern of a trial function
$\varepsilon_3(x)$	Electric field pattern of a trial function
$E_1(x)$	Part of the electric field diffraction pattern, $E(x,z)$
$E_2(x)$	Part of the electric field diffraction pattern
$E(x,z)$	The electric field diffraction pattern of a grating
F_e	Force on the x-ray membrane
I_o	Intensity of the zeroth order diffracted beam
I_1	Intensity of the first order diffracted beam
$I(x,z)$	The intensity pattern corresponding to $E(x,z)$
j	$\sqrt{-1}$
$\bar{k}$	Reciprocal wave vector, magnitude = $2\pi/\lambda$
K	Magnitude of the reciprocal grating vector, $2\pi/p$
L	Grating to film plane distance in the spectroscopic measurements

M_α	Characteristic tungsten line radiation at λ = 0.698 nm
M_β	Characteristic tungsten line radiation at λ = 0.676 nm
M_γ	Characteristic tungsten line radiation at λ = 0.609 nm
m	Spatial period division division factor
n	Index for summations
n_i	Index of refraction
n_o	Maximum value for n
p	Grating period
p_n	Grating period at point P_n
P_n	Location on the grating
q	Index for summations
S	Mask to substrate gap
t	Thickness of insulator between mask and substrate
t_r	Resist thickness
t_1	Odd integers
t_2	Even integers
t_g	Thickness of a gold grating line
V	Voltage applied to an x-ray lithography mask for electrostatic contact
$\hat{x}$	Unit vector in the plane of the grating and perpendicular to the grating lines
$\hat{y}$	Unit vector in the plane of the grating and parallel to the grating lines
$\hat{z}$	Unit vector perpendicular to the plane of the grating.
β	Variable which determines the width of the transmissive region of the grating (the spaces). Width = $2p/\beta$
Δh	Size of the x-ray source in the spectroscopic measurements
$\Delta\lambda$	Spectral resolution

$\Delta\lambda_{min}$	Minimum resolution
Δp	Difference in grating period between two points
Δy	Width of the recorded pattern in the spectrometer experiments
Δz	Distance between two successive planes where spatial period divisions occur
δ	Penumbra
Λ	Distance between "doubling" planes in the U.V. "doubling" work
ε_c	Dielectric constant of an insulator
λ	Wavelength
θ	Half angle between the two laser beams in holographic lithography
θ_c	X-ray collimation angle
θ_d	Diffraction angle
η	Grating diffraction efficiency
ϕ	The phase, at z = 0, of the electric field pattern transmitted by the grating lines

ACKNOWLEDGEMENTS

A number of people have contributed to the success of this dissertation through scientific and technical support. First and foremost, I would like to thank my advisor, Prof. Henry I. Smith, for providing the opportunity for me to work with him. I have learned a great deal through my contact with him, and most significantly, he has been a source of guidance and encouragement.

Through my studies, I have had the pleasure of working closely with the Lincoln Laboratory Microelectronics Group (Group 87), where a number of people have been particularly helpful. Special thanks go to Dr. D. Flanders for teaching me the basics of x-ray lithography, and "shadowing", and for collaborating on the early x-ray spatial period division work. Conversations with Dr. D. Shaver have been very helpful and stimulating. Many other members of the Microelectronics Group especially N. Efremow and P. DeGraff, have taught me the finer points of wafer preparation and SEM microscopy, and to them, and to the entire group, I will be forever grateful.

Many thanks go to the members of the MIT Submicron Structures Laboratory. Dr. John Melngailis, Manager of the Submicron Structures Laboratory, has been helpful to me at various times during this work. M. Griswold has provided fine microscopy. Special thanks go to James Carter for technical support throughout every aspect of the work described herein.

The spectroscopy work was performed at the Lawrence Livermore National Laboratory, with help from a number of people. This work was scientifically profitable and productive primarily due to the efforts of Dr. Natale M. Ceglio. His enthusiasm for x-ray spectroscopy and imaging, and his

encouragement were crucial. In addition, his dynamic personality provided for a very enjoyable atmosphere in which to work. The entire Lawrence Livermore Zone Plate "Swat" Team helped in many of the technical parts of this research, and to them, I am thankful.

I am also grateful to Gary Stone for preparing the thick (> 50 μm) layers of polyimide for Zone Plate Coded Imaging, and for gold plating the thick zone plate patterns. Also, Gary taught me the proper manner in which to expose and develop the x-ray sensitive film used in spectroscopy.

The deep U.V. spatial period division work was accomplished with the collaboration of Richard Osgood and Daniel Ehrlich of Lincoln Laboratory. I would like to thank them for many stimulating conversations and for the opportunity to use their equipment.

Special thanks go to my wife, Ann, for providing me with the encouragement, support and patience that I needed to continue with this work. I must also thank her for proofreading this manuscript, and to her, I will be forever grateful.

The list of acknowledgements should continue for several more pages, but to everyone else who has helped me, all I can say is "Thank You".

CHAPTER I

INTRODUCTION

Periodic and quasi-periodic surface relief structures, such as gratings and Fresnel zone plates, have played crucial roles throughout the growth of the physical sciences, especially during the past century. Diffraction gratings were essential elements in determining the fine and hyperfine structures in atomic and molecular spectra. The analysis of the emission spectrum of hydrogen in the early part of this century depended on grating technology. This led to Neil Bohr's famous breakthrough and subsequently, to the development of quantum theory. Peiter Zeeman in 1897, in a now famous experiment, observed the magnetic splitting of the two D lines in the sodium spectrum using a diffraction grating which was supplied by the renowned American physicist, Henry Rowland.[1] Rowland spent a major portion of his life perfecting grating fabrication technology and using these gratings in spectroscopy. In the early 1880's, Rowland developed a highly accurate ruling engine, with which he was able to produce gratings with approximately 1700 lines/mm (grating periods $\sim$ 590 nm).[1] By comparison, the finest gratings commercially available today are produced using holographic lithography, and have periods as fine as 300 nm, which is only slightly smaller than Rowland's century-old gratings.[1]

Recently, gratings have found applications in surface acoustic wave devices,[2] guided wave optics,[3] distributed feedback lasers[4] and x-ray spectroscopy.[5-10] In all of these applications, precise control of grating period and freedom from distortion are essential. Furthermore, applications such as x-ray spectroscopy demand gratings with greater dispersion

(finer grating periods) and higher contrast (higher attenuation in the grating lines) than the 300 to 500 nm period gratings that are considered available with current state of the art technology. Several groups around the world are working on the means of achieving gratings with finer spatial periods and higher contrast.[10-15] In addition to the problem of producing gratings with finer periods, a materials problem is encountered which limits the attenuation in the grating lines (the contrast of the grating). For example, for visible radiation ($\lambda \backsim$ 500 nm), a transmission diffraction grating can be fabricated with aluminum lines, which have a very high attenuation ($\backsim$ 300 dB/μm) in the visible regime.[16] Thus, a 10 nm thickness of aluminum is sufficient to produce a transmission grating with 3 dB contrast between the grating lines and spaces. Alternatively, a phase grating in the visible regime can also be produced by etching a grating into a lossless material with a relatively large index of refraction, such as quartz (index of refraction $\backsim$ 1.5).[16] By comparison, in the soft x-ray regime (0.4 nm $\lesssim \lambda \lesssim$ 10 nm), materials exhibit small indices of refraction (typically n $\backsim$ 0.90 to 1.0), and attenuation ranging from less than 1 dB/μm to over 150 dB/μm.[17] The inability to decouple the index of refraction of a material from the x-ray attenuation through the material makes it impossible to produce a lossless phase grating in the soft x-ray regime. Alternatively, a transmission diffraction grating requires a thick layer of dense material, such as gold or tungsten. For example, greater than 100 nm of gold is required to attenuate 1 nm radiation by 3 dB[17] which corresponds to a thickness-to-wavelength ratio of > 100:1. In the visible regime, this same thickness-to-wavelength ratio is 1:50.

In this dissertation, the ability to produce thick gold diffraction gratings, using a combination of several sub-micron fabrication techniques, will be presented. These techniques, which will be discussed in Chapter 2, include photolithography,[18] holographic lithography,[18,19] ion-beam etching[18,20] (milling), reactive ion etching,[21] "shadowing",[22] x-ray lithography[18,23-26] and gold microplating.[27] For some of the applications to be discussed, precise control of the linewidths of the gratings to 10 nm tolerances was essential, and the fabrication techniques for this have been demonstrated. The far field diffraction pattern of these gratings was recorded, using a soft x-ray source, Chapter 3, and the diffraction efficiency and resolving power of the gratings were measured. Finally, these thick gold gratings were used to experimentally demonstrate spatial-period-division,[28,29] Chapters 4 and 5, and thereby produce a sub-100 nm period grating. This technique can be extended to produce large areas of uniform gratings with final periods limited by fundamental lithography restraints. The theory of spatial-period-division is presented in Chapter IV, along with the complications imposed by the non-ideal nature of the original ("parent") gratings in terms of both transmission and phase shift through the grating lines. Finally, Chapter 6 presents the conclusions of this research and include suggestions for future experimental work.

CHAPTER II

FABRICATION OF THICK GOLD GRATINGS

II-A INTRODUCTION

In this chapter, the requirements for a transmission diffraction grating and the traditional methods of grating fabrication and their limitations will be reviewed. The procedure that is used for the production of thick gold gratings is then explained, and scanning electron micrographs are shown to depict the results after each successive fabrication step. Finally, a procedure to produce thicker gold gratings is outined.

II-B REQUIREMENTS FOR A SOFT X-RAY TRANSMISSION DIFFRACTION GRATING

For x-ray spectroscopy, a transmission diffraction grating with maximum contrast (ratio of the intensity transmitted by the grating spaces relative to the intensity transmitted by the grating lines) is desirable. In the soft x-ray regime, the relatively small finite attenuation of materials[17] will limit this contrast, but a reasonable figure-of-merit for the contrast is to require that there be less than 10% transmission (greater than 10 dB attenuation) through the grating lines, defining unity transmission as the transmission through the grating spaces, Figure II-1. It is further required that this be true throughout the entire soft x-ray range of interest. A plot of attenuation of soft x-rays through gold,[30-33] Figure II-2, reveals that a minimum of 0.5 μm of gold is required for the grating to exhibit > 10 dB attenuation through the range 1 nm $\leq \lambda \leq$ 10 nm. In addition, other requirements for the thick gold grating include:

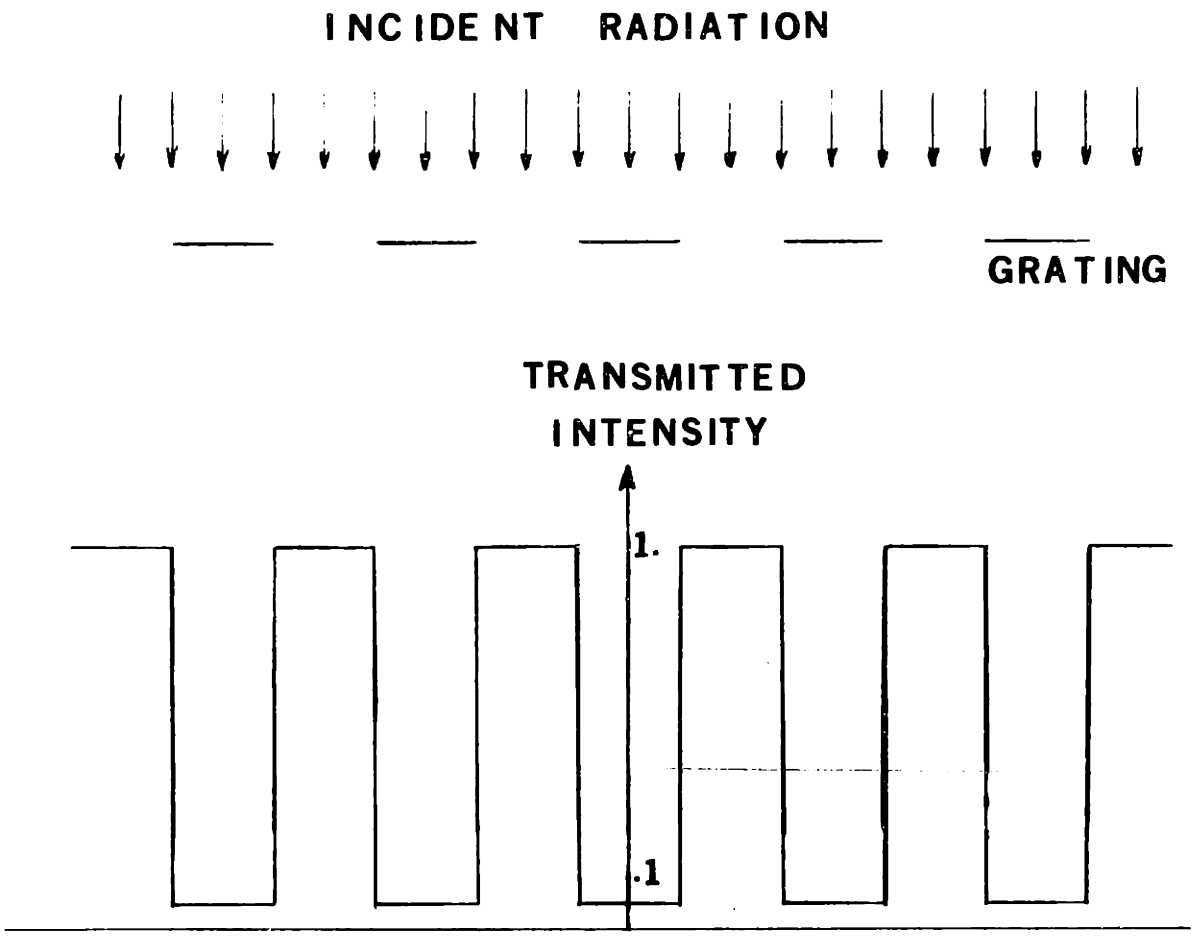

Figure II-1 For x-ray spectroscopy, the ratio, at the plane of the grating, of the x-ray intensity transmitted by the grating spaces, to the transmitted x-ray intensity attenuated by the grating lines, should be $\gtrsim$ 10:1.

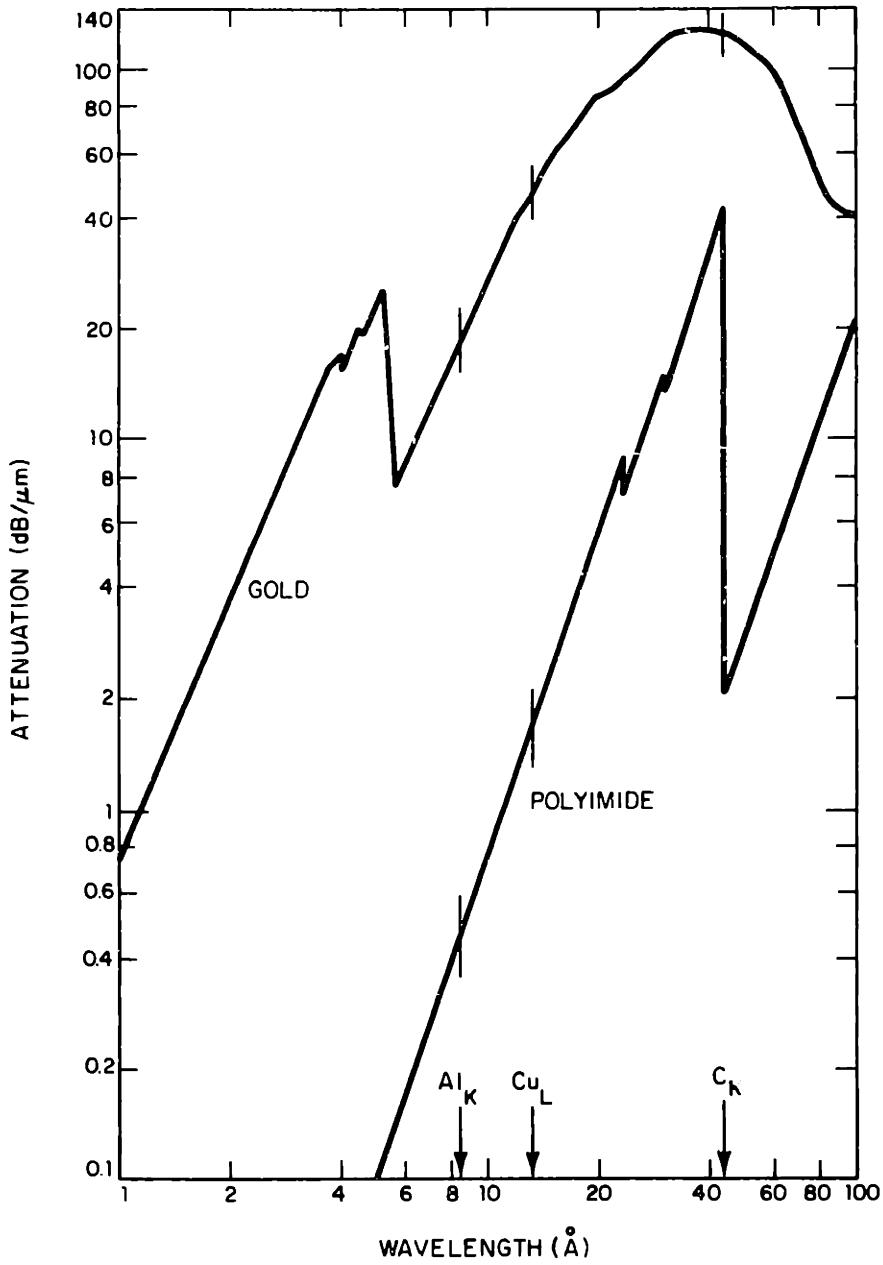

Figure II-2 X-ray attenuation (dB/μm) versus wavelength for gold and polyimide.

(a) Vertical sidewalls;

(b) Finest spatial periods for maximum dispersion (gratings with periods $\lesssim$ 300 nm);

(c) Large areas which are free from distortion (for maximum resolving power).

Finally, these gratings must be mounted onto an x-ray transparent support membrane, so that the grating can function as a transmission diffraction grating, Figure II-3.

II-C TRADITIONAL METHODS OF GRATING FABRICATION

Currently, there are three approaches to grating fabrication: ruling,[34] holographic lithography[18,19] and electron beam lithography.[18] Each of these approaches is very useful, but each has limitations. Ruling engines are machines which draw a diamond-tip scribe across a surface to either engrave the surface or to scratch a surface film, such as aluminum or silver. Gratings are then produced by repetitively drawing the scribe across the surface. The advantages of the ruling engine are that it is capable of producing gratings over very large areas, and also that the gratings made by a ruling engine can be blazed by properly cleaving the diamond-tip scribe. Unfortunately, these gratings have some limitations; specifically, the gratings can be only as accurate as the mechanical motion that guides the scribe across the sample. Any periodic flaw in the mechanical motion will result in a periodic defect in the grating. Whereas the flaw may be negligible for large (> 1 μm) period gratings, this defect will become increasingly more pronounced for the smaller grating periods. The periodic flaw in Rowland's ruled gratings exhibited a modulation ("side-

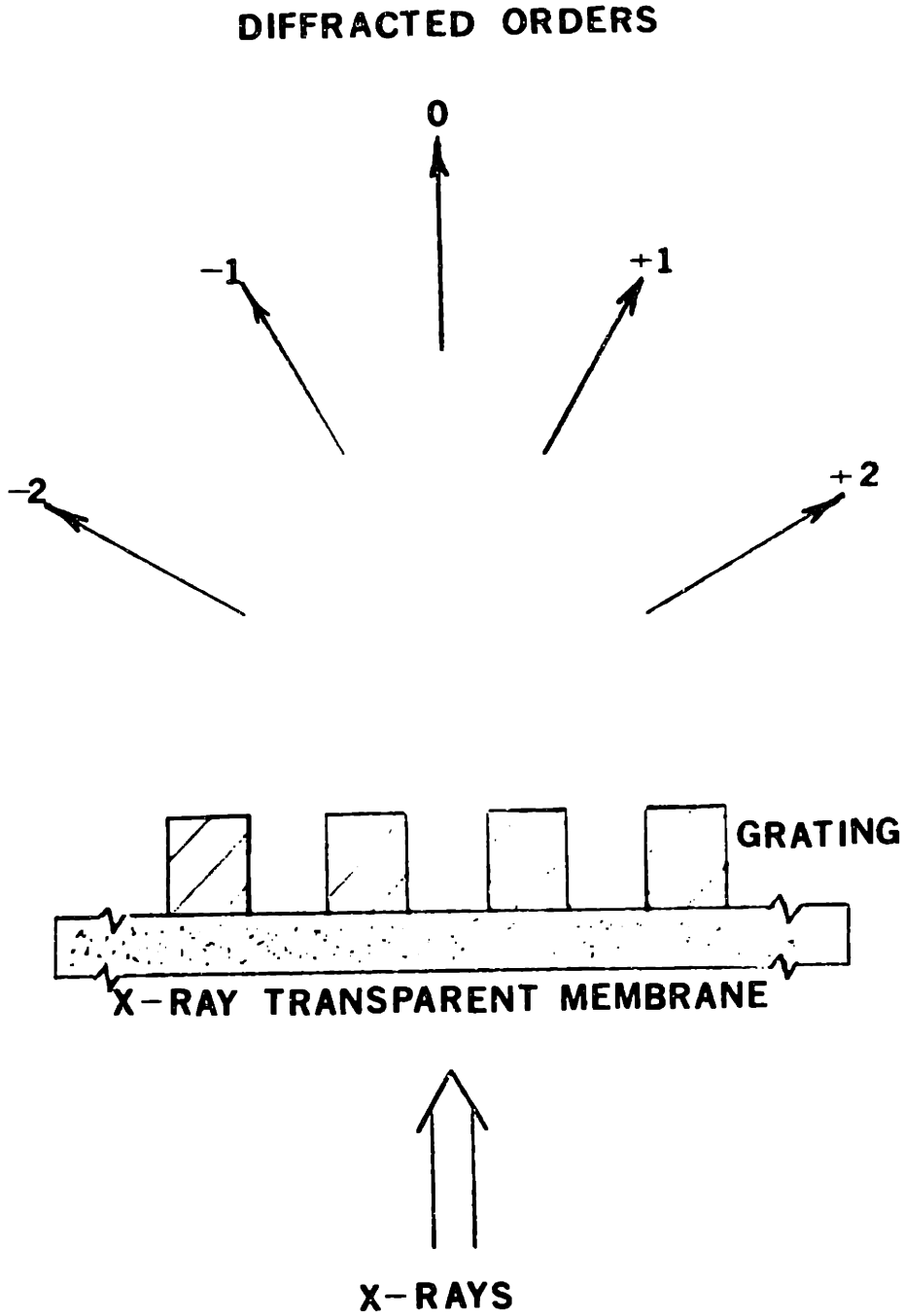

Figure II-3 An illustration indicating how an x-ray transmission diffraction grating can be used to obtain spectral information of an x-ray source. The grating is mounted on an x-ray transparent membrane, and the incident x-rays are diffracted into various orders. The angle of diffraction is wavelength dependent.

bands") in the far-field diffraction pattern. These sidebands eventually became known as "Rowland ghosts".[35] Finally, in ruling, there is no control over the raggedness of the lines produced by scratching the sample surface, and the sidewalls of the grooves tend not to be vertical.

A second method of producing gratings is through holographic lithography, which is the recording in a photosensitive film (usually called a "resist") the standing wave pattern produced by the interface of two mutually coherent laser beams (usually obtained by splitting one laser beam into two with a beam splitter). The period of the grating that is produced in this fashion is given by:

$$p = \frac{\lambda}{2 \sin\theta} \qquad (2\text{-}1)$$

where θ is the half angle between the two laser beams and λ is the wavelength of the laser. For commercially available lasers, such as a helium cadmium laser, or an argon-ion laser, grating periods are generally restricted to be greater than $\sim$ 180 nm. The standing wave pattern can then be recorded in a photosensitive medium, such as photoresist, either directly onto substrates of interest, or onto intermediate substrates, such as x-ray lithography masks, which can be later replicated.[18,36] Holographic lithography in a high index medium has been used to expose gratings with periods as fine as 110 nm,[37] but this technique is cumbersome, and cannot be extended to much finer periods. One major advantage of holographic lithography is that gratings produced in this fashion can be essentially distortion free, relative to other methods of grating fabrication.[18] However, gratings produced by holographic lithography have their own disadvantages. Specifically, reflections of the incident radiation from the sub-

strate interfere with the two incoming beams to produce standing waves with planes of maxima and minima parallel to the substrate.[38] This produces a variation of exposure with depth which limits the resist thickness to less than half the wavelength of the incident radiation in the resist. Typically, commercially available photoresists have an index of refraction of approximately 1.6 in the visible spectrum,[39] which limits the resist thickness to approximately less than $\sim$ 100 nm. Hence, holographic lithography has fundamental limitations which constrain both the grating period and the resist thickness. Furthermore, the cross-sectional profile of the grating lines produced holographically are not vertical, but rounded, which is undesirable. Lastly, the transmission diffraction gratings for use in the soft x-ray regime need to be made in a high density material, such as gold, for sufficient attenuation. Gratings in photoresist do not satisfy this requirement.

The third method of producing submicron period gratings is with scanning electron beam lithography.[18] In this method, an electron beam is used to "write" a pattern in an electron sensitive resist. One major problem that is encountered with electron beam lithography is the long exposure times which, for a 300 nm period grating, can be as long as one hour per square millimeter.[18] Other problems can be the distortions introduced into the gratings due to fluctuations in the electron-beam power supplies and electronics, and the limited accessible field of view, typically one to two square millimeters. To produce gratings larger than this would require producing several smaller gratings and "stitching" them together. Any error in the stitching of these small gratings would cause severe problems in the performance of the larger grating. Again, as in holographic litho-

graphy, the gratings produced in this manner are in a resist, and further processing is needed to achieve the thick gold gratings needed for x-ray spectroscopy.

II-D PROCEDURE TO PRODUCE THICK GOLD GRATINGS

II-D-1 Introduction

With the traditional methods of grating fabrication, the desired soft x-ray transmission diffraction gratings are impossible to produce. The basic reason for their failure is that the traditional methods cannot yield fine period gratings in thick absorber over large areas. Ruling engines cannot be used to produce high quality, low distortion, sub-micron period gold gratings, and the techniques of holographic lithography and electron beam lithography produce gratings in resist, not in gold. Further processing can be used to transfer the resist pattern into thin gold ($\sim$ 100 nm), but not into the thick gold that is desired. Hence, a new procedure, capable of producing high aspect ratio (ratio of feature height to minimum lateral feature size) structures with vertical sidewalls was needed. A multistep process, involving soft x-ray lithography, was such a procedure.

X-ray lithography has been shown to be capable of producing extremely high aspect ratio (> 5:1) structures[18,29,30,40] in an x-ray sensitive resist, such as polymethylmethacrylate (PMMA), with a resolution $\sim$ 20 nm.[22,56] The approach used in this dissertation to produce high aspect ratio gold gratings was to first define a high aspect ratio grating in PMMA on a thin, $\sim$ 10 nm, gold plating base, and then to gold microplate the surface, using the PMMA as a mold. This process would produce a thick gold grating, Figure II-4.

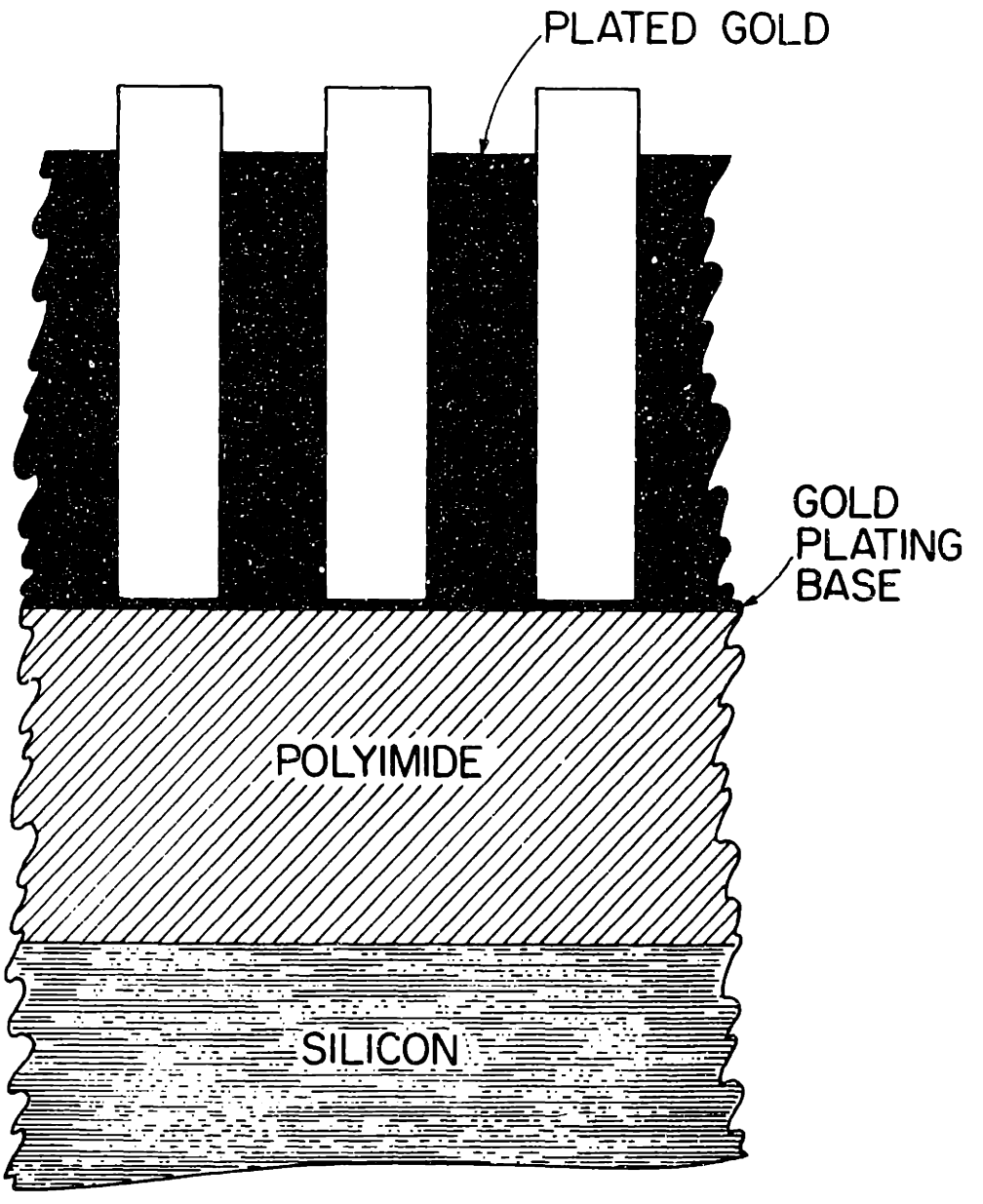

Figure II-4 A cross-sectional diagram of a thick gold grating, produced by gold microplating, and using a thick PMMA grating as a mold. The polyimide serves as the x-ray transparent membrane, and the silicon is etched away prior to spectroscopic use.

The problem addressed is how to produce a thick PMMA grating. Obviously, a master (mask) grating is required to expose the PMMA. Fortunately, the high contrast of the PMMA permits a thin ($\sim$ 60 nm) gold grating to be used as the x-ray lithography mask for exposing $\gtrsim$ 1 μm thick PMMA. To produce the thin gold mask, holographic lithography was used to define the grating pattern, which was then transferred into a thin gold layer ($\sim$ 100 nm thick) by ion etching. This thin gold x-ray mask was supported by a thin ($\sim$ 1 μm) x-ray transparent membrane.

In summary, the procedure outlined above requires:

(1) Mask pattern generation using holographic lithography;

(2) Transfer of the pattern into thin gold by ion beam etching;

(3) Pattern replication into thick PMMA by x-ray lithography;

(4) Gold microplating.

For the fabrication of the thick gold gratings needed for spatial period division, chapters 4 and 5, the procedure outlined above was expanded to include a means of controlling the line-to-period ratio of the plated gold grating. This expanded technique will be described in detail in Chapter 5.

II-D-2 Mask Pattern Generation Using Holographic Lithography and Ion Etching

To generate the grating in PMMA by x-ray lithography, an x-ray mask must first be fabricated. Holographic lithography is a technique which is capable of producing $\lesssim$ 200 nm period gratings in a photosensitive resist. It also has the added advantage of being capable of exposing large (>1 cm^2) areas of gratings in under one minute of exposure time when a low power (10-50 milliwatts) near U.V. or U.V. laser is used. However, the grating

lines produced by holographic lithography have rounded resist profiles, which are caused by reflections from the substrate. Fortunately, holographic lithography can be used to produce the original pattern necessary for an x-ray lithography mask.

The actual experimental arrangement used for the holographic lithography exposures is depicted in Figure II-5. A laser beam from a helium-cadmium laser (λ = 325 nm) is incident upon a beam splitter to produce two beams of nearly equal intensity. These two beams are each reflected by a front surface mirror, and each beam passes through a spatial filter. The filters are the final optical elements in the interferometer arms. The two spherical beams that result are incident upon a resist coated substrate, where the two beams interfere to produce a sinusoidal standing wave pattern in space, with period p given by equation 2-1. Because two spherical beams are interfering (as opposed to two plane waves), the period of the standing wave pattern increases as the distance from the pattern center increases, and this can introduce a distortion into the grating. This distortion can be kept arbitrarily small by simply increasing the distance from each of the spatial filters to the resist coated substrate. In the exposures performed, the difference in the grating period relative to the desired grating period, $\Delta p/p$, was kept at $\lesssim 1 \times 10^{-4}$ over approximately one centimeter diameter grating dimensions (APPENDIX E).

The reflected beams in holographic lithography interfere with the two incoming beams to produce standing waves with planes of maxima and minima parallel to the substrate.[38] This leads to a variation in the development rate of the exposed resist versus depth. Consequently, it is necessary to

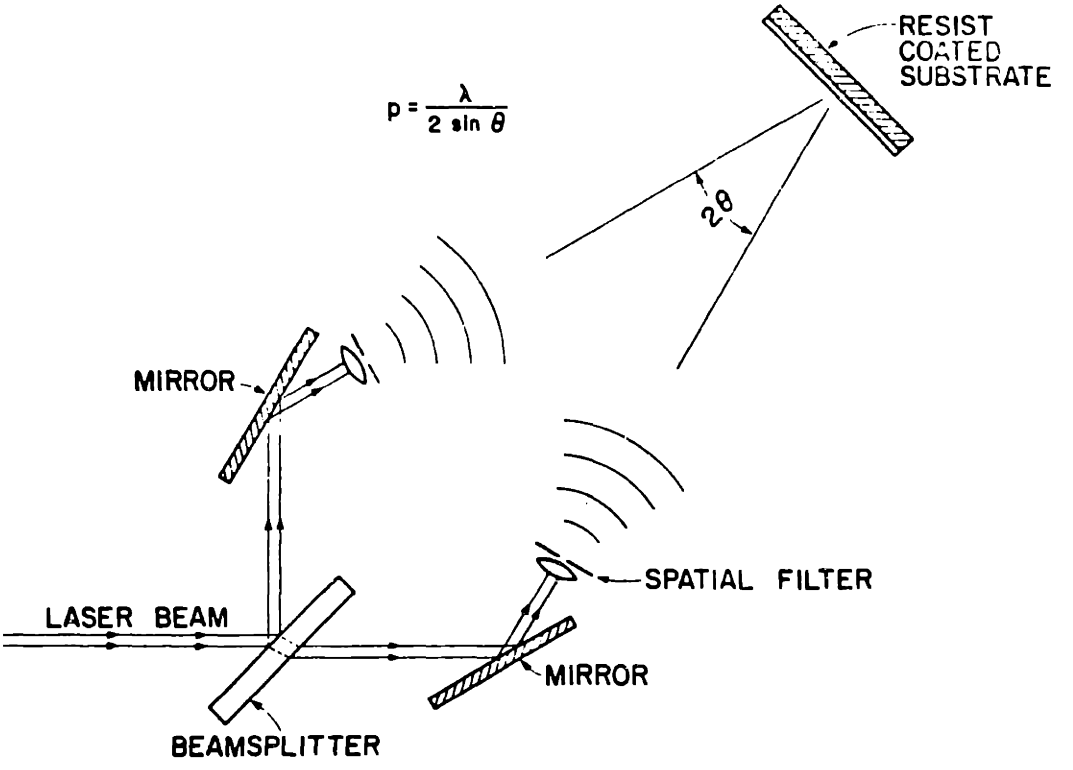

Figure II-5 A diagram of the holographic lithography exposure system. Two spatial filters are the final optical elements in the interferometer arms, and the two resulting spherical beams overlap to produce a standing wave pattern. This pattern is recorded on a resist coated substrate.

limit the resist thickness, t_r, to less than one-half the spatial period of this intensity pattern. The resist thickness is then limited by:

$$t_r \lesssim \frac{\lambda}{4} \sqrt{\left(\frac{1}{n_i^2 - \sin^2 \theta}\right)} \qquad (2\text{-}2)$$

where n_i is the index of refraction of the photoresist.

By varying the half angle between the incident laser beams, it is possible to produce gratings with spatial periods ranging from several microns to nearly half the wavelength of the laser beam. Using a helium cadmium laser, (λ = 325 nm) and a half angle of 75°, a grating with a spatial period of 168 nm in thin (60 nm) resist was produced, Figure II-6. This resist pattern can then be used as a mask to transfer the grating pattern into a thin gold layer through ion beam etching.

Ion beam etching is a sputter etch technique which bombards the surface of a sample with energetic ions.[18] A line drawing of an ion beam etching apparatus is shown in Figure II-7. A beam of energetic argon ions (500 eV) bombards the sample and the exposed gold is sputter etched, with the photoresist grating being used as a mask. Therefore, a holographically exposed photoresist grating pattern can be transferred into a thin (60 to 120 nm) layer of gold by ion beam etching. However, since the original photoresist pattern does not have a vertical sidewall structure, and is also etched in the ion beam, and since some of the sputtered gold redeposits onto the grating sidewalls, the gold grating produced in this manner will also have a non-vertical sidewall. Figure II-8 is a scanning electron micrograph of a 300 nm period grating, ion beam etched into a $\sim$ 100 nm film of gold, using $\sim$ 60 nm of photoresist as the mask. Note that the gold

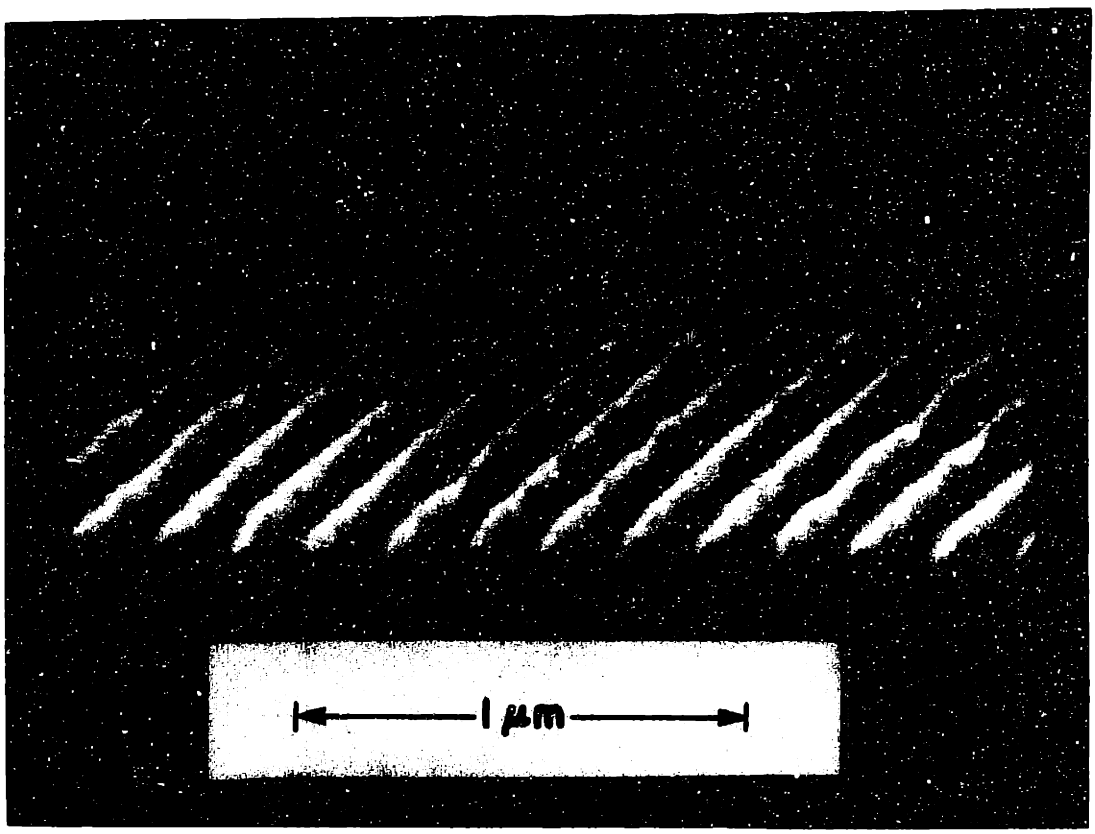

Figure II-6 A scanning electron micrograph of a 168 nm period grating, holographically exposed, in ∿60 nm photoresist, using the holographic lithography set-up in Figure II-5.

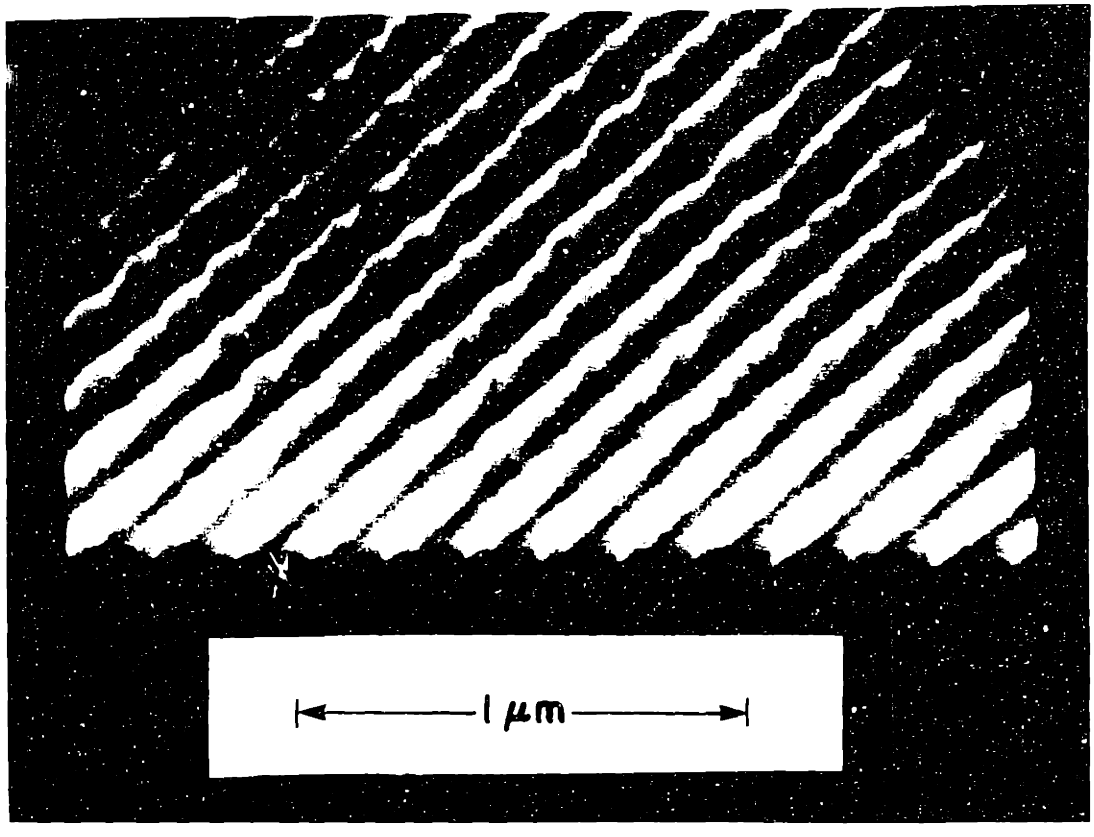

Figure II-6 A scanning electron micrograph of a 168 nm period grating, holographically exposed, in ~60 nm photoresist, using the holographic lithography set-up in Figure II-5.

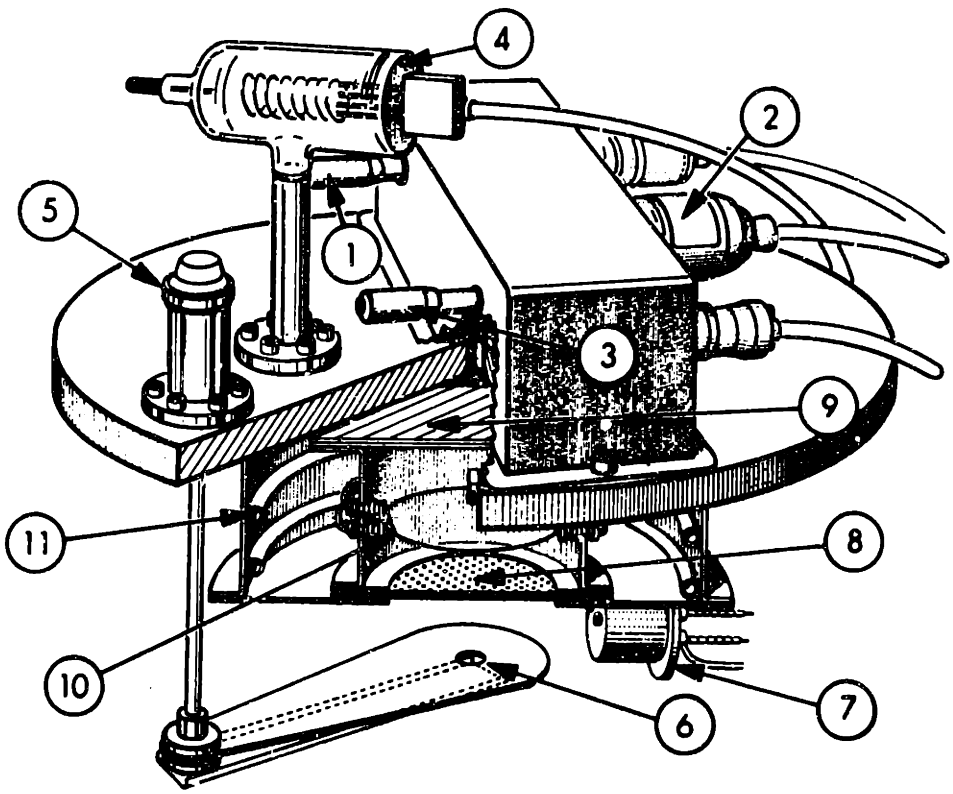

Figure II-7 Line drawing on an ion-etch apparatus

1) gas valve
2) high voltage connections
3) gas bleed
4) ionization gauge tube
5) rotary feed-thru for blank off plate
6) faraday cup
7) neutralizer
8) acceleration grids
9) anode housing
10) cathode
11) water cooling lines

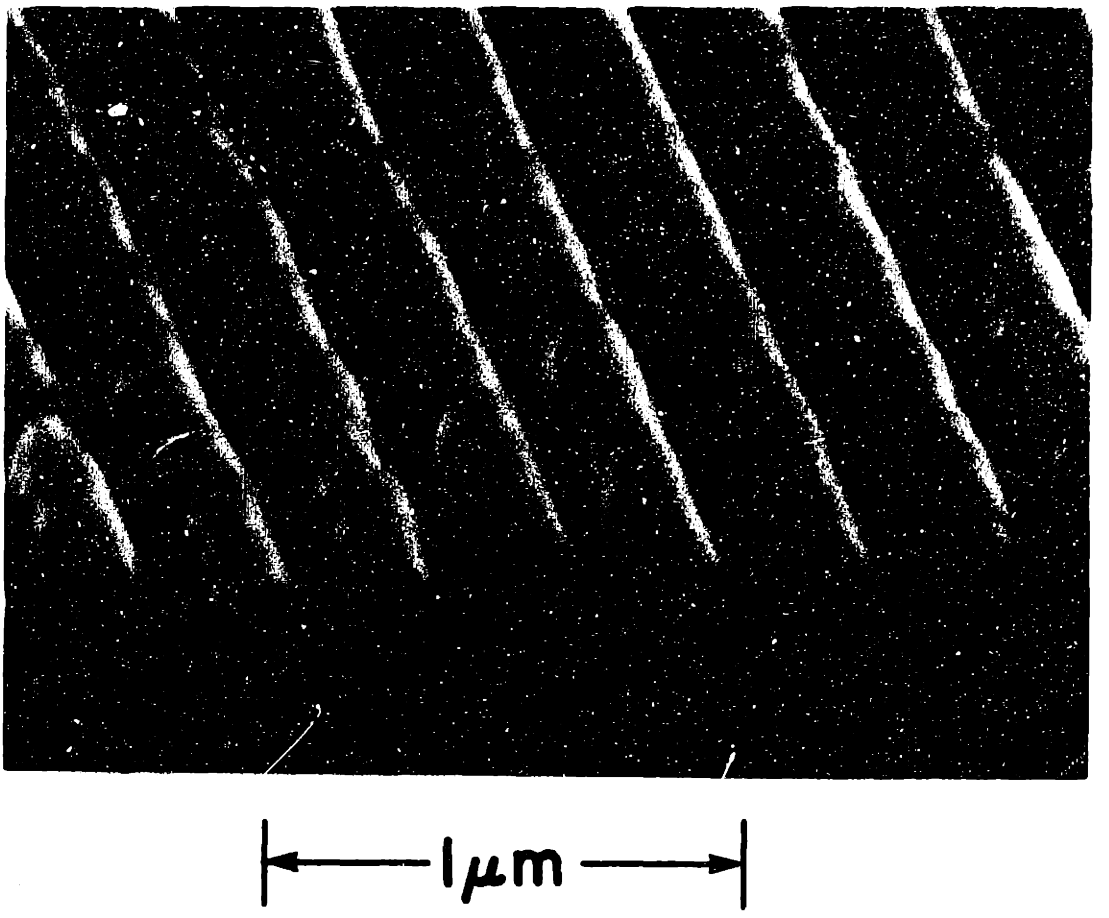

Figure II-8 A scanning electron micrograph of a ∿ 100 nm thick gold grating, suitable for x-ray lithography replications. The pattern was produced by holographic lithography and ion etching.

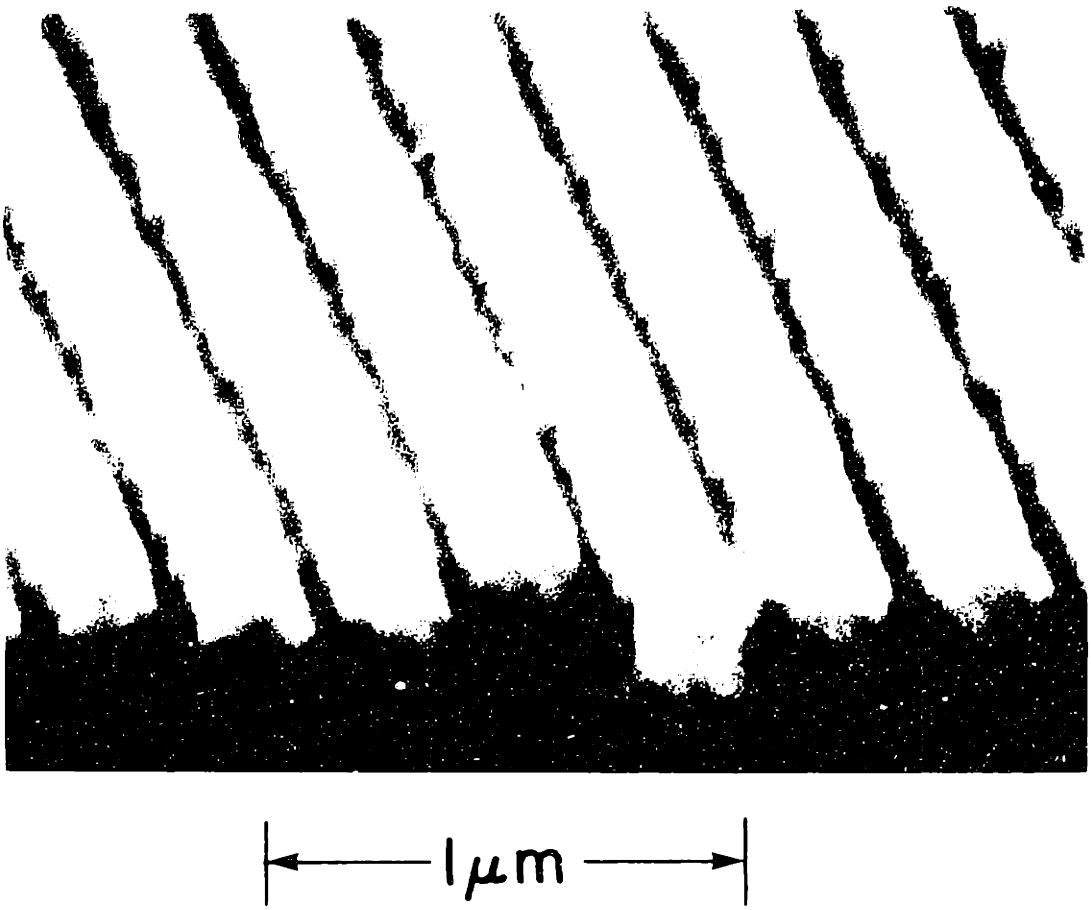

Figure 11- A scanning electron micrograph of [illegible] gold grating, suitable for use [illegible] applications. The pattern was produced by [illegible] lithography [illegible].

tends to stretch slightly during the cleaving and hence, the cleaved edge is not sharp. However, this micrograph clearly shows the grating pattern replicated into thin gold, and also shows the rounded sidewalls of the gold grating. This effect will not degrade the x-ray lithography replications because of the extremely high contrast of the PMMA, as will be discussed in the next section.

II-D-3 Pattern Replication Using X-ray Lithography

II-D-3-a High Resolution Considerations

X-ray lithography has been shown to have several properties which are desirable for the pattern replication process needed in this work. Specifically, under appropriate conditions the patterns produced by x-ray lithography can have extremely sharp sidewalls and are capable of high aspect ratios (> 5:1).[18,23,29,30] The high aspect ratios are due, in part, to the absence of back reflections of x-rays from the substrate. X-ray lithography also offers high resolution because of the x-rays' short wavelength and reduces diffraction effects (dependent upon the wavelength and the mask to substrate gap, S). These properties, along with the high resolution recording capabilities of PMMA, make it possible to produce a high aspect ratio grating in PMMA. The diffraction limitations on resolution indicate an increase in resolution with decreasing wavelength. However, the range of photoelectrons produced in the PMMA by the incident x-rays increases with decreasing wavelength, Figure II-9.[30,41,42] The optimum wavelength for high resolution work is then determined a trade-off between by the wavelength, diffraction effects and the photoelectron range. Diffraction effects can be made negligible by placing the mask and substrate into

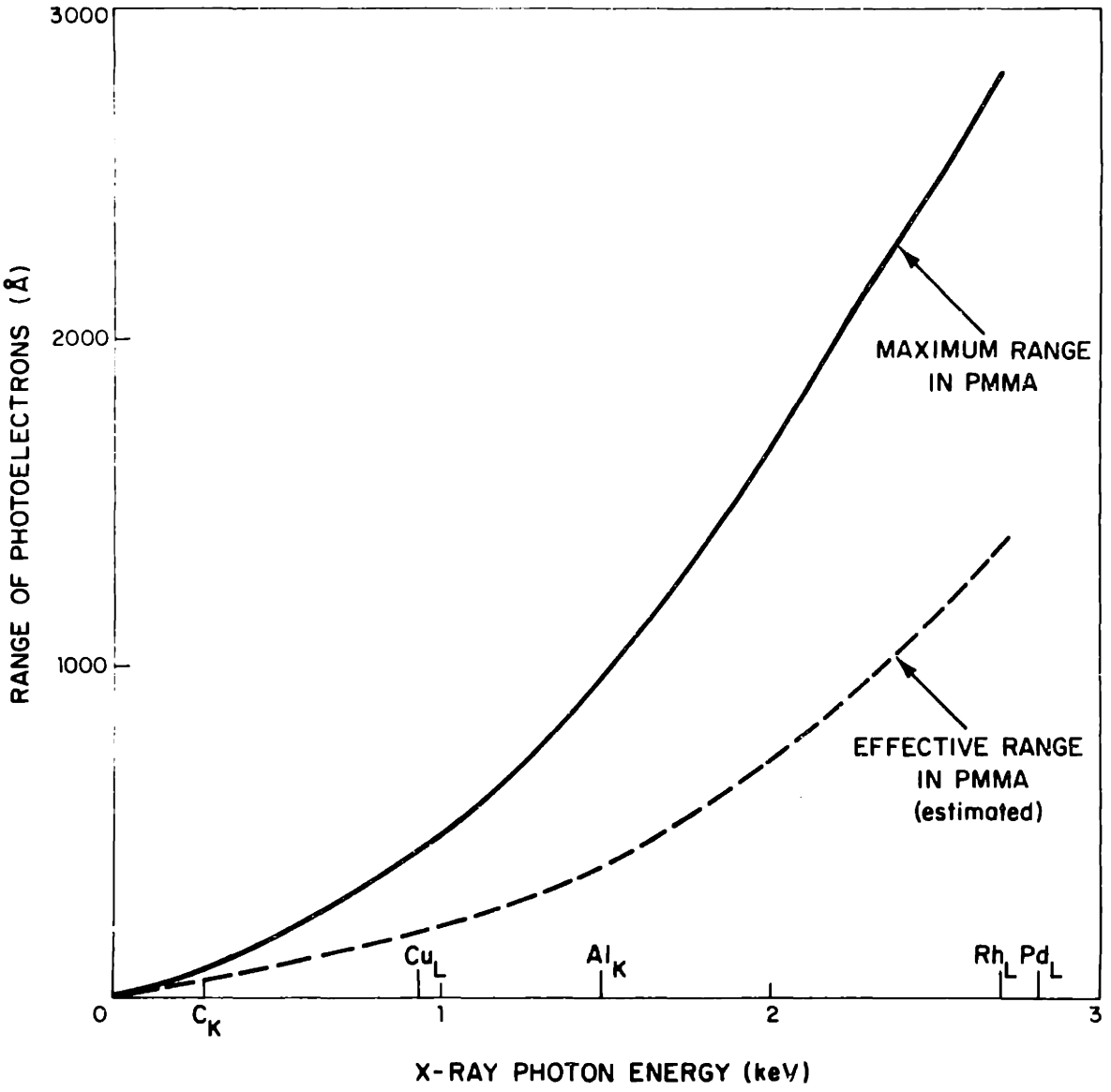

Figure II-9 The maximum and effective range of photoelectrons in PMMA, as a function of incident x-ray energy. For optimum resolution, the C_K x-ray is used.

intimate contact. The best resolution is obtained when the range of photoelectrons in the PMMA is approximately equal to the incident x-ray wavelength. This match occurs at approximately 5 nm, and hence, the carbon-K (C_K) x-ray (λ = 4.5 nm) was used for the high resolution work discussed in this dissertation.

Ultimately, the resolution of x-ray lithography is limited by the intrinsic resolution of the x-ray sensitive resist used. The x-ray sensitive resist with the highest known resolution is PMMA, and has been extensively studied by several workers.[43-46] In this work, samples were coated with PMMA (molecular weight $\sim$ 950,000) and were exposed to the C_K rays. The molecular weight of the exposed PMMA is reduced by chain scission. The samples were then developed in a mixture of 60% isopropyl alcohol and 40% methyl isobutyl ketone (MIBK) which dissolves the lower molecular weight PMMA, leaving the higher molecular weight resist unaffected. The high nonlinearity of the dissolution rate of the PMMA versus absorbed energy,[46] Figure II-10, produces extremely sharp vertical sidewalls in the PMMA, even when the mask pattern has curved or tapered sidewalls, such as those which are produced by holographic lithography and ion etching, Figure II-8.

II-D-3-b X-Ray Mask Materials

The choice of materials and material thicknesses to be used for the x-ray mask must be coupled with the choice of the x-ray wavelength to be used. It is desirable that the mask support structure (membrane) absorb a minimum of the incident x-rays, and that the material used as the x-ray absorber attenuate the incident x-rays by a minimum of 3 dB. Following the work of D.C. Flanders,[30] polyimide was chosen as the x-ray mask membrane,

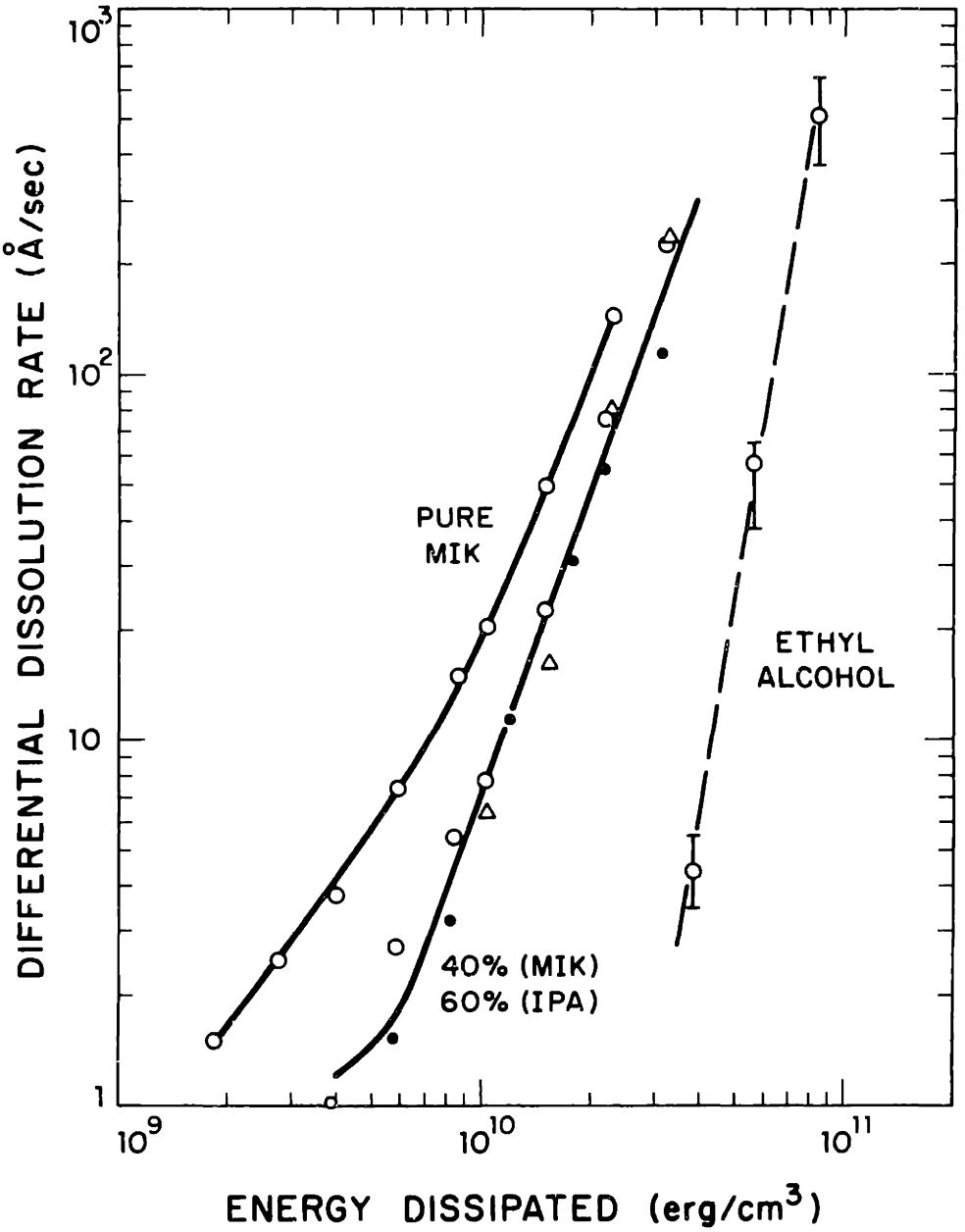

Figure II-10 Differential dissolution rate of PMMA versus dissipated energy for three developers. The steep slope of the curves indicate that a factor of two increase in the dissipated energy gives rise to a $\sim$10x increase in development rate. (Reference 46).

because polyimide absorbs approximately 2 dB/μm of the incident carbon-K x-ray.[33] In addition, gold is an excellent mask material because of its high attenuation[30] ($\sim$ 128 dB/μm at $\lambda = C_K$) and its ease of patterning. Thus, a 30 nm thick gold pattern ($\sim$ 4 dB) on a one micron thick polyimide membrane meets the requirements for an x-ray mask. Obviously, thicker gold patterns will increase the contrast of the mask, and subsequently increase the differential dissolution rate between exposed and unexposed regions on the PMMA. This will yield straighter sidewalls and permit the exposure of thicker resist layers.

The process of producing x-ray masks can now be summarized in Figure II-11. First, a one micron layer of polyimide was spun onto either a thin glass or silicon substrate, followed by an evaporation deposited layer of 10 nm of chrome and 70 to 120 nm of gold. Lastly, a 60 nm layer of photoresist was spun onto the sample, Figure II-11a. Holographic lithography was then used to produce a grating in photoresist, Figure II-11b. Subsequently, the photoresist was used as a mask to transfer the grating into the thin gold film by ion etching, Figure II-11c. After ion etching, the photoresist was removed and the polyimide membrane was bonded to a cylinder. The substrate was etched away in an appropriate liquid etch, and a tapered, one inch outside diameter, 0.75 inch inside diameter aluminum ring was bonded to the polyimide membrane. After epoxy curing, the cylinder was removed by cutting through the polyimide membrane outside the aluminum ring with a razor blade.

II-D-3-c The X-Ray Source

A diagram of the apparatus used for the x-ray lithography exposures is

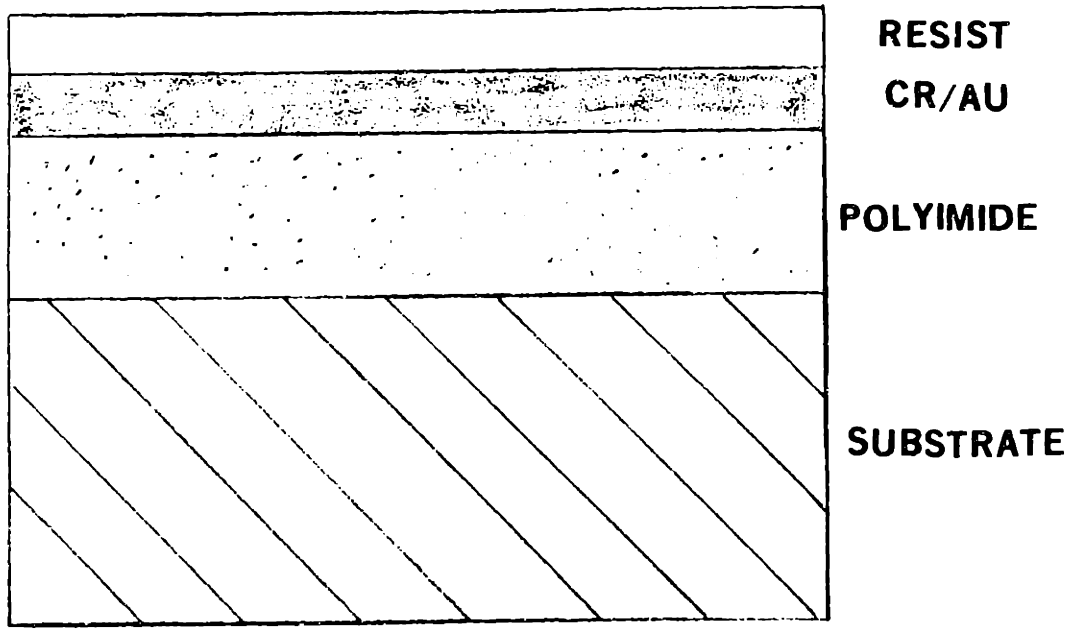

(A)

Figure II-11 (A) Cross-sectional view of samples used to fabricate an x-ray lithography mask. Substrates were coated with ∿ 1 μm polyimide, 10 nm Cr, ∿ 1000 nm Au and ∿ 60 nm photoresist.

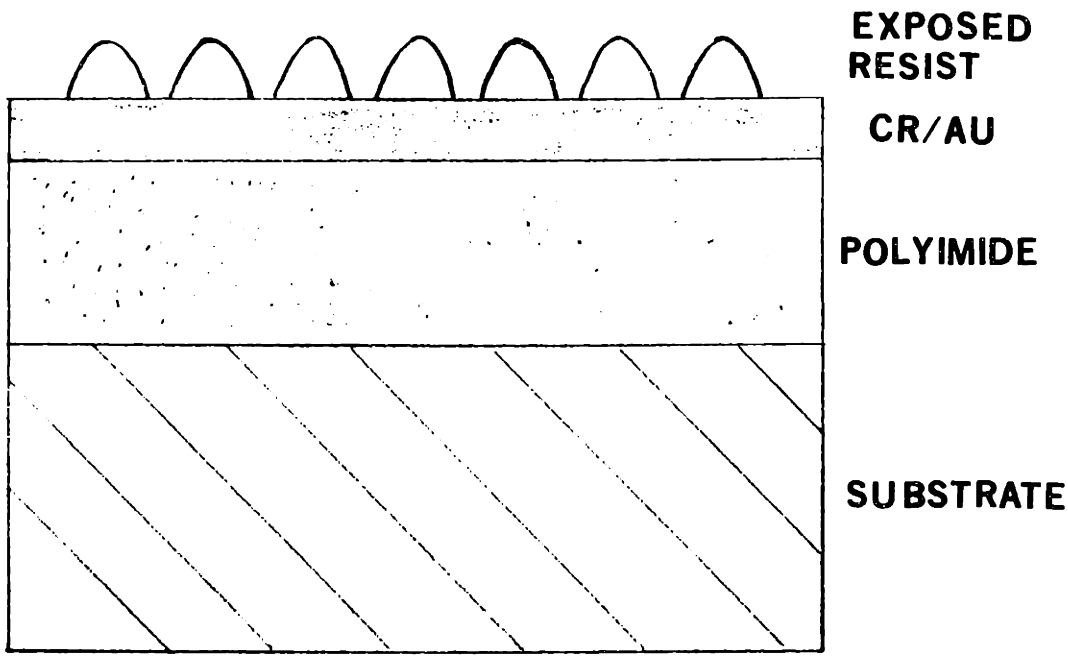

(B)

Figure II-11 (B) Resist pattern after holographic exposure.

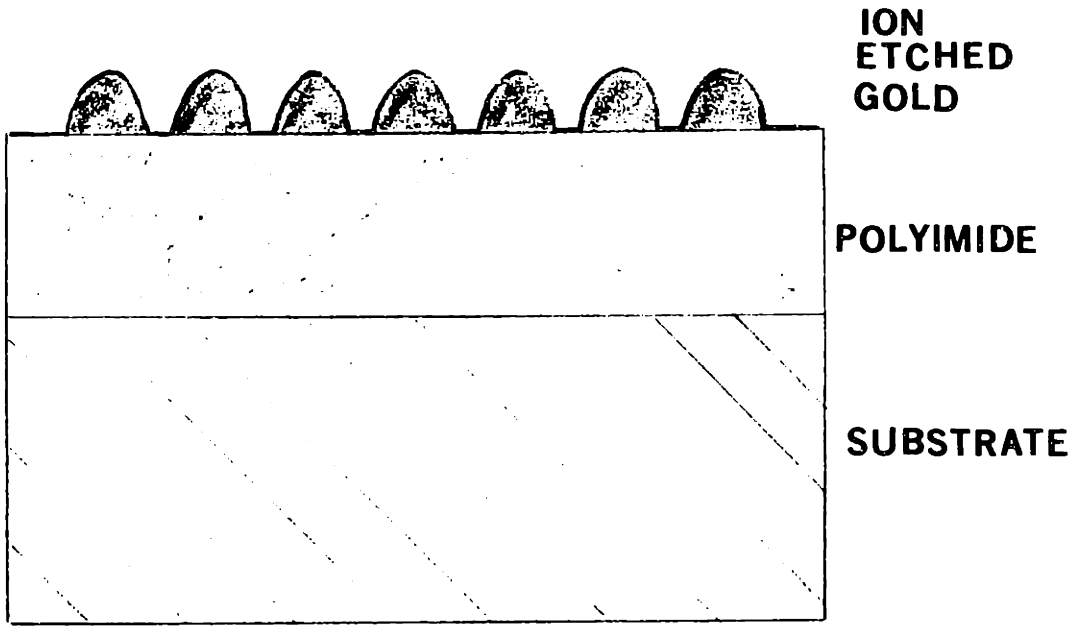

(C)

Figure II-11 (C) Gold pattern after ion etching, and subsequent resist removal.

shown in Figure II-12, and this closely follows the work of D.C. Flanders.[30] The x-ray source is a converted electron beam evaporator.[47] X-rays are generated by bombarding a carbon anode with electrons emitted from a hot filament. Both the circular filament and the cylindrical cathode shield are at a negative potential, typically -6 kV, and electrons are accelerated onto the water-cooled anode. Because the geometry is circularly symmetric, it is possible to focus the electron beam into a spot with a diameter between one and two millimeters. Between 200 and 300 watts of power are focused onto the anode. Higher powers are possible, but tend to "pit" the carbon anode.

The carbon anode is a carbon insert,[30] machined to fit inside a copper hearth, Figure II-13. To cool the carbon anode during exposures, the back surface of the copper hearth is water cooled. The carbon insert is held in thermal contact with the copper hearth by first heating the copper hearth with a hand-held "heat gun". A small amount of 99.99% pure indium was placed inside the copper hearth and was also heated until it melted. Since indium "wets" both copper and carbon, it makes a good interfacial layer between the two surfaces, and insures a high thermal conductivity. When the indium is molten, the polished carbon insert is placed into the copper hearth, and a restraining copper cap is screwed into place to hold the assembly together.

To insure that electrons, which may be back-scattered from the anode, do not contribute to the exposure of the resist, it is necessary to incorporate an electron deflector into the x-ray lithography apparatus. This electron deflector is a long aluminum strip which is at the negative cathode potential, and which also protrudes through a hole in a grounded alumi-

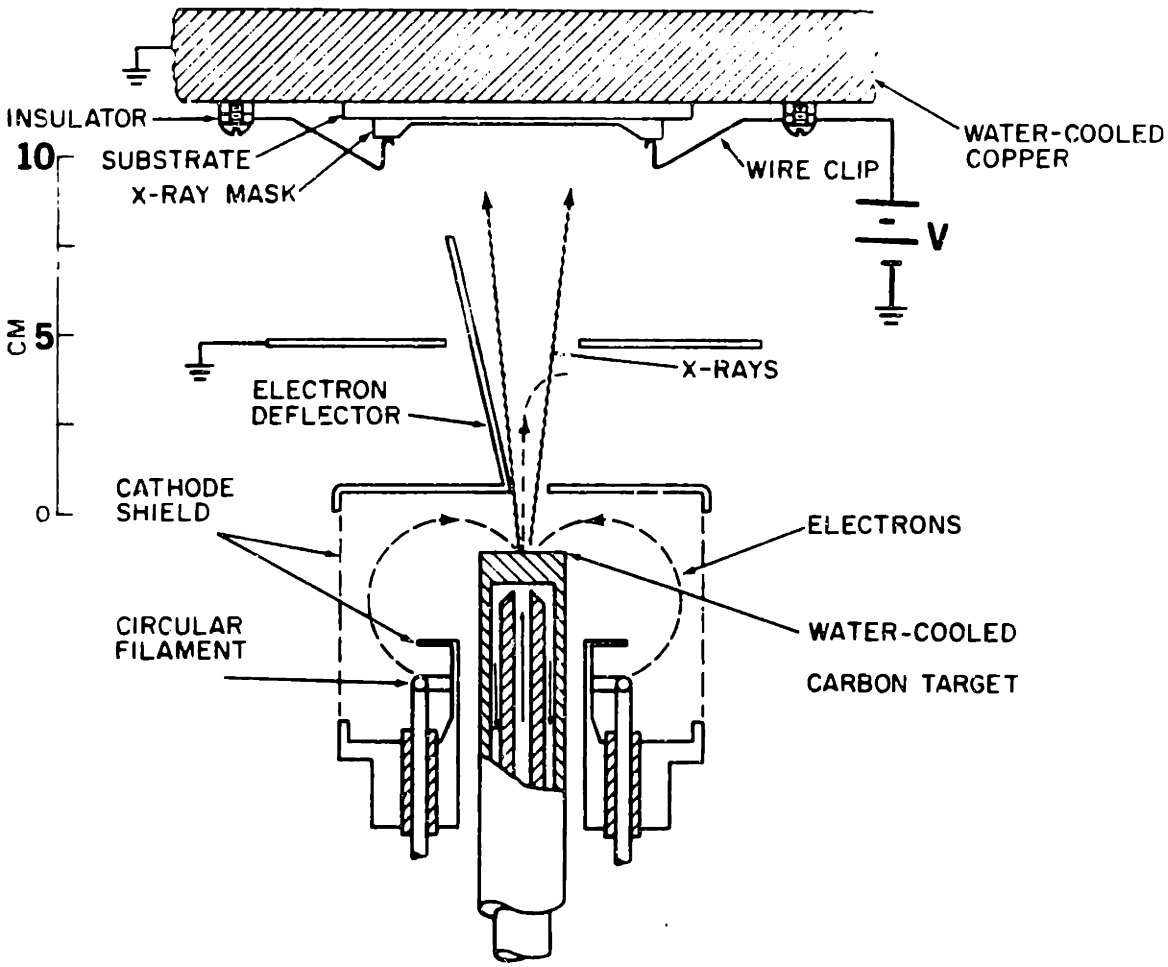

Figure II-12 Line drawing of the x-ray lithography apparatus. Typical operating parameters for the electron gun were -6.5 KeV and 45 ma emission current.

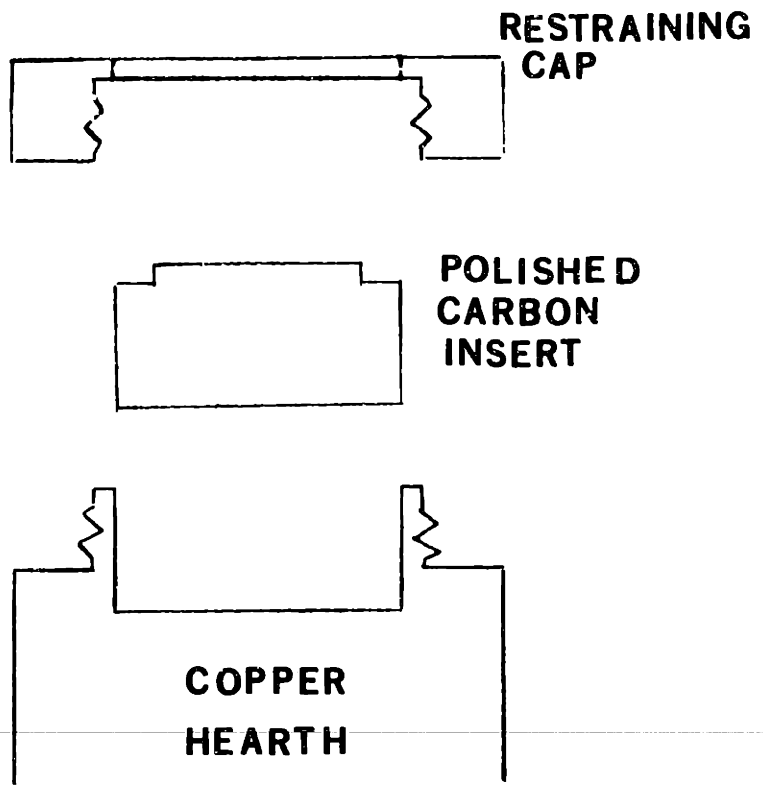

Figure II-13 The carbon anode for x-ray lithographic replications was fabricated by inserting a polished carbon disk into a water-cooled copper hearth. A restraining cap held the carbon insert securely in the copper hearth.

num block (Figure II-12). In this way, backscattered electrons are electrostatically deflected to the side, and only x-rays are incident upon the PMMA coated substrate. The substrate is kept in thermal and electrical contact with a water cooled copper block. This contact is necessary to prevent heating of the mask and substrate, as well as for the electrostatic clamping of the mask to the substrate, as explained in section II-D-3-d.

II-D-3-d Intimate Contact Replications

Due to the finite size of the x-ray source, penumbral blurring can degrade the replication of the x-ray mask into the PMMA. Penumbral blurring can be illustrated quite easily, and is shown schematically in Figure II-14, where the penumbra, δ, is given by

$$\delta = \frac{S\ d}{D} \qquad (2\text{-}3)$$

where S is the mask to substrate gap, d is the source diameter, and D is the source to sample distance. To illustrate this point, a 2 mm diameter source placed 5 cm away from the sample, with a sample to mask gap of 1 μm, will have a penumbra of 40 nm, which is unacceptable for the replication of sub-100 nm feature sizes.

To deal with penumbral blurring, the mask and substrate were held in intimate contact. For thin ($\lesssim$ 1/4 μm) resists, with a source to sample distance of 6 cm, and a source diameter of 1 mm, the resulting penumbra of 4 nm is acceptable. For thicker resists ($\gtrsim$ 1 μm), the anode to substrate distance was increased to 10 cm, to keep the penumbra $\lesssim$ 10 nm. To maintain the mask and sample in intimate contact, an electrostatic hold-down scheme was used.[23,24,30] Two electrically conducting films (one on the mask and

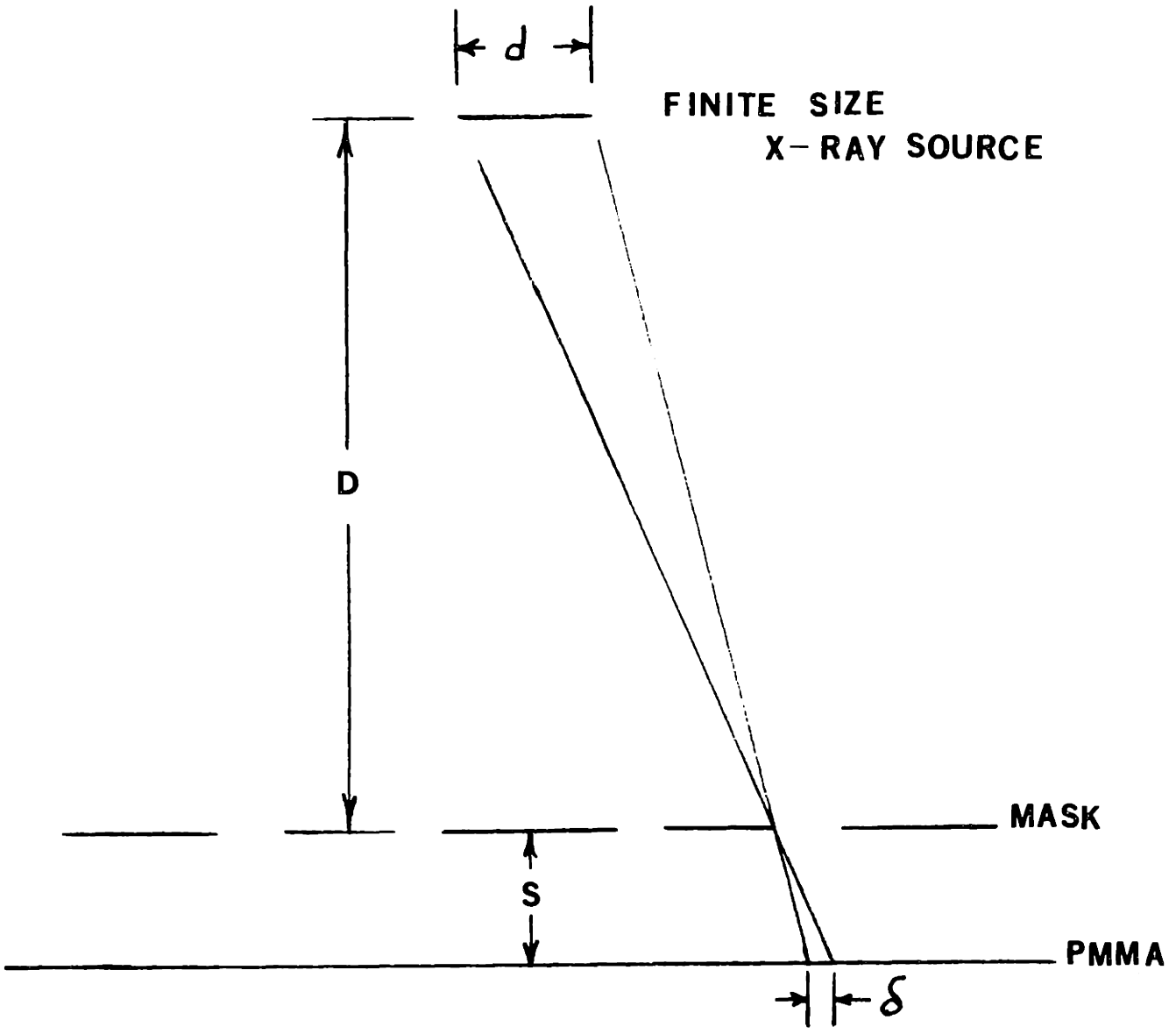

$$\delta = \frac{s\,d}{D}$$

Figure II-14 The penumbra, δ, associated with a finite size x-ray source, leads to a "blurring" of the exposed resist pattern.

one on the substrate) with a suitable dielectric between them (to form a capacitor), were connected to a d.c. voltage. The electrostatic field between the two films then held the mask and substrate together. Unfortunately, PMMA is an unreliable insulator between the two films of this capacitor, perhaps because pinholes may develop in the PMMA, which can then cause a short circuit between the two conducting films of the capacitor. Hence, the mask membrane, or some other insulator, had to be used as the insulator in the capacitor. Several configurations of the mask, sample and appropriate insulator to maintain intimate contact were described by D.C. Flanders,[30] and are reproduced in Figure II-15.

For a given insulator thickness t, area A, dielectric constant ε_c, of the insulator, and an applied voltage V, the force on the x-ray membrane, F_e, is:[48]

$$F_e = \frac{\varepsilon_c V^2 A}{2t^2} \qquad (2\text{-}4)$$

For typical values of t = 1 μm, V = 50 volts, A ∿ 2 cm^2, and $\varepsilon_c = 3\varepsilon_o$, the resulting force of approximately 6 Newtons was sufficient to maintain contact.

To monitor the contact between the mask and substrate, a capacitance meter was placed across the capacitor formed by the mask and substrate. The capacitance, C_m, is given by:

$$C_m = \frac{\varepsilon_c A}{t} \qquad (2\text{-}5)$$

where A is the area in contact. For a typical area of ∿ 2 cm^2 and a mask to wafer gap ∿ 1 μm, a capacitance of ∿ 5 nf is measured, which agrees with calculated values for the capacitance.

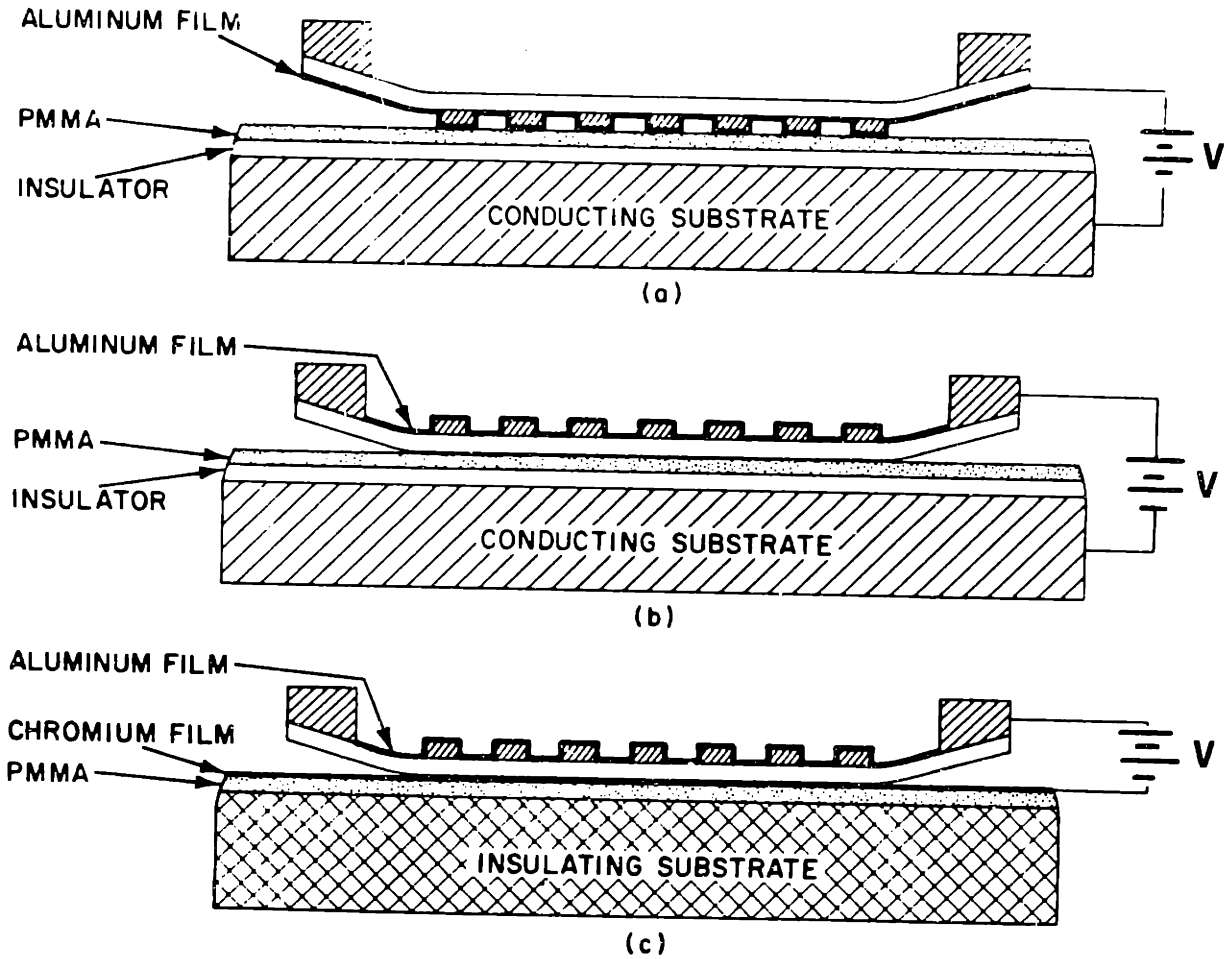

Figure II-15 To maintain contact between an x-ray mask and substrate, several electrostatic "hold-down" orientations are possible, three of which are illustrated above. (Reference 30).

In order to maintain intimate contact between the x-ray lithography mask and a conducting substrate (such as a gold plating base) it was necessary to utilize a new configuration between the mask and substrate. Because PMMA itself is a poor insulator, it was necessary that the polyimide membrane of the x-ray mask act as the insulator between the conducting plating base on the sample, and the conducting layer on the mask. It was desired to keep the mask grating on the "front" surface of the x-ray mask to minimize penumbral blurring and diffraction effects. Finally, it was also necessary to electrically isolate the individual gold lines that form the grating mask. This is because if there exists a conductive path through the PMMA, then the conducting plating base and a gold grating line on the front surface of the mask will be in electrical contact. If all the gold grating lines are electrically continuous, then this entire "front" surface of the x-ray mask will be at ground potential (the same potential as the plating base) and any voltage applied to the "back" side of the x-ray mask will result in an electric field from the "back" side of the mask through the membrane to the "front" side of the mask. There will be a negligible field between the mask and substrate and the result will be a loss in contact. However, if the gold grating lines on the mask are electrically isolated (Figure II-16), the mask will remain in contact, even if some of the grating lines short through the PMMA and are at ground potential, because a majority of the mask will not electrically short through the PMMA.

An x-ray lithography mask produced by first defining the pattern holographically and then transferring the pattern into thin gold by ion etching, was unsuitable for replications into PMMA on a conducting base. This

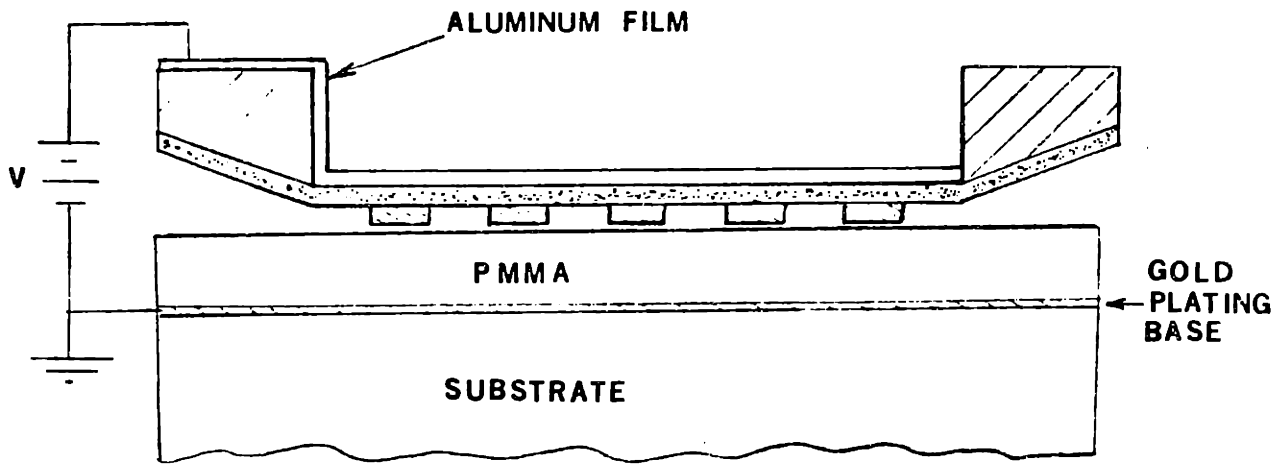

Figure II-16 The orientation between an x-ray mask and PMMA on a conducting substrate, necessary to replicate gratings with minimal penumbral distortion, and to maintain contact through an electrostatic "hold-down".

is presumably due to some finite conductivity between the gold grating lines. However, an x-ray mask produced by liftoff was suitable for the desired replications. This necessitated the intermediate step of producing a gold grating through a liftoff process, Figure II-17.

II-D-3-e Experimental Results -- Pattern Replication Into PMMA

To test the x-ray replication process, grating patterns of 300 and 199 nm spatial periods were replicated into 0.25 μm thick PMMA. The test exposures were done on silicon wafers with 500 nm of silicon dioxide on the front surface. PMMA was then spun onto the SiO_2. A 1.5 μm thick polyimide membrane with a 70 nm thick gold grating pattern defined by the holographic lithography and ion etching process, was used as the x-ray mask. The mask and substrate were held in intimate contact using the configuration in Figure II-15a. Proper exposure times were determined by the amount of x-ray flux needed to develop the PMMA at a rate of ∿ 100 nm/min. Approximately one joule/cm^2 of C_K x-ray incident radiation was required to develop the PMMA in two minutes, using a mixture of 60% isopropyl alcohol and 40% methyl-isobytul-ketone (MIBK). During development, the sample was monitored by observing the development of exposed PMMA in a large (∿ 3x10 mm) region (monitor area) adjacent to the grating area. This region had no mask pattern, and the development of the PMMA could be easily observed. When the PMMA in the monitor area was developed completely, further development was discontinued.

To analyze the PMMA grating pattern, it was necessary to use a scanning electron microscope (SEM). To observe an insulating material such as PMMA, the surface must first be coated with a thin conducting gold layer

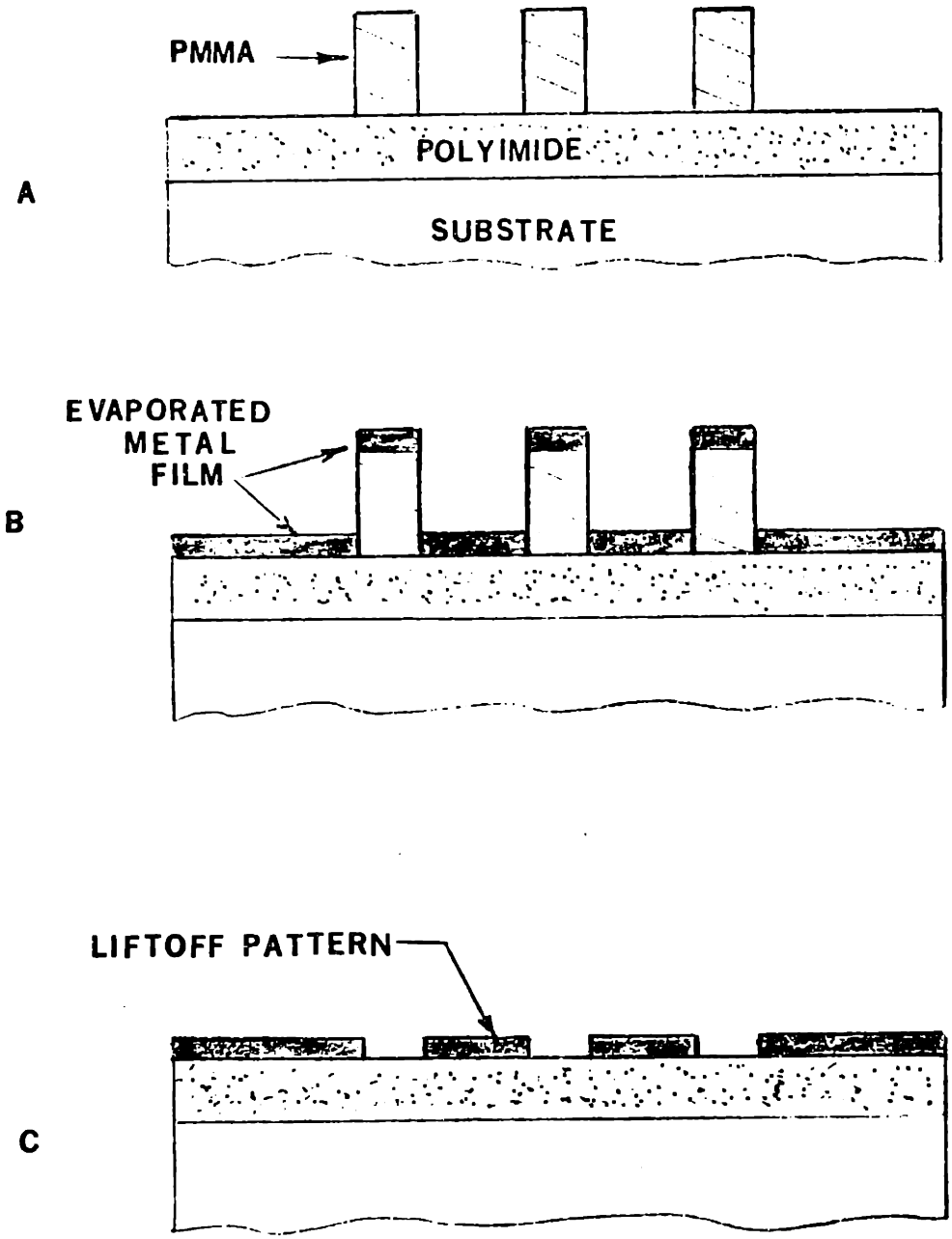

Figure II-17 Illustration of the "lift-off" process. In (A), a PMMA structure with straight sidewalls is defined by an x-ray lithographic process. (B) A metal film is evaporated onto the surface. (C) The PMMA is dissolved away.

for electrical continuity to ground (to avoid charging of the sample) and for enhanced secondary electron emission.[49] The gold coating is accomplished by bombarding a gold target plate with a 500 eV argon-ion beam, which sputters gold off the target plate. This produces an extended source of gold ions. The sample to be coated is placed near the target plate so as to allow the sputtered gold to deposit onto the sample. After an initial coating, the sample is rotated so that a second gold coating will deposit gold onto any surface that may not have been coated during the initial coating. In this way, a thin ($\sim$ 10 to 15 nm) continuous gold layer over the entire grating surface is achieved, Figure II-18.

Figures II-19 and II-20 are scanning electron micrographs of the replications of 300 and 199 nm period gratings into 0.25 μm thick PMMA. Note the straight sidewalls of the PMMA and the high aspect ratios achieved (> 3:1). In both cases, the lines of the PMMA are approximately 70 nm wide. The roughness of the sidewalls is believed to reflect edge roughness in the original mask.

As already mentioned in section II-D-3-d, to expose a grating into PMMA on a conducting surface, it became necessary to use the mask-wafer orientation in Figure II-16, and to produce the mask grating by a liftoff process. To properly expose $\sim$ 1 μm thick layers of PMMA, greater than 6 dB of contrast is required in the mask. To achieve this, an x-ray mask of a 300 nm period grating was made by lifting off 10 nm chromium and 60 nm of gold. Typical grating areas on the x-ray mask produced by liftoff were in excess of one square centimeter. This mask was then replicated into 0.7 μm thick PMMA on a 10 nm chromium, 10 nm gold plating base. Figures II-21 and II-22 are electron micrographs of the resulting PMMA structure.

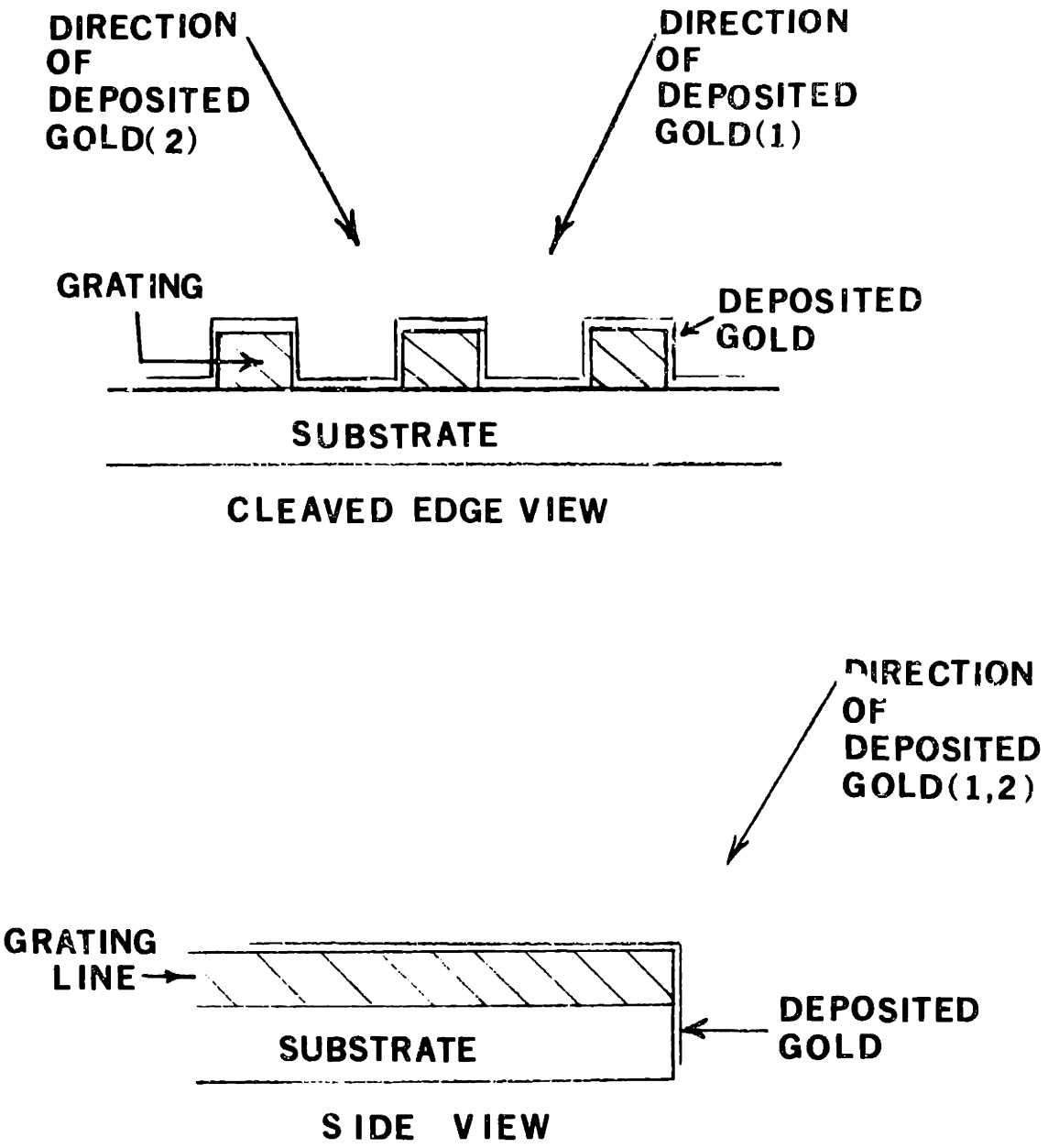

Figure II-18 Samples are coated with gold for scanning electron microscopy. Two coatings are used, with the sample oriented at different angles to the "beam" of gold ions, to guarantee sufficient gold coverage over the entire surface.

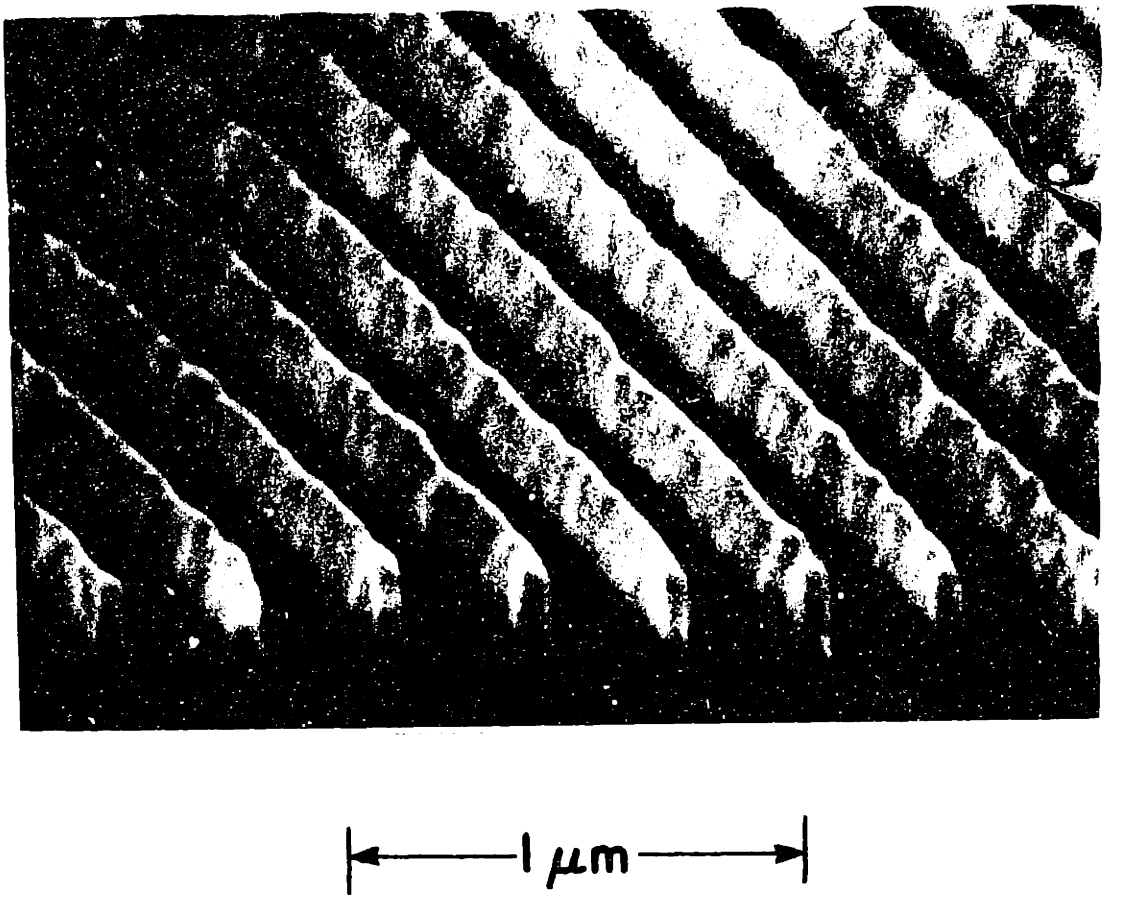

Figure II-19 A scanning electron micrograph of a 300 nm period grating with ∿ 70 nm wide lines in ∿ 0.25 μm PMMA.

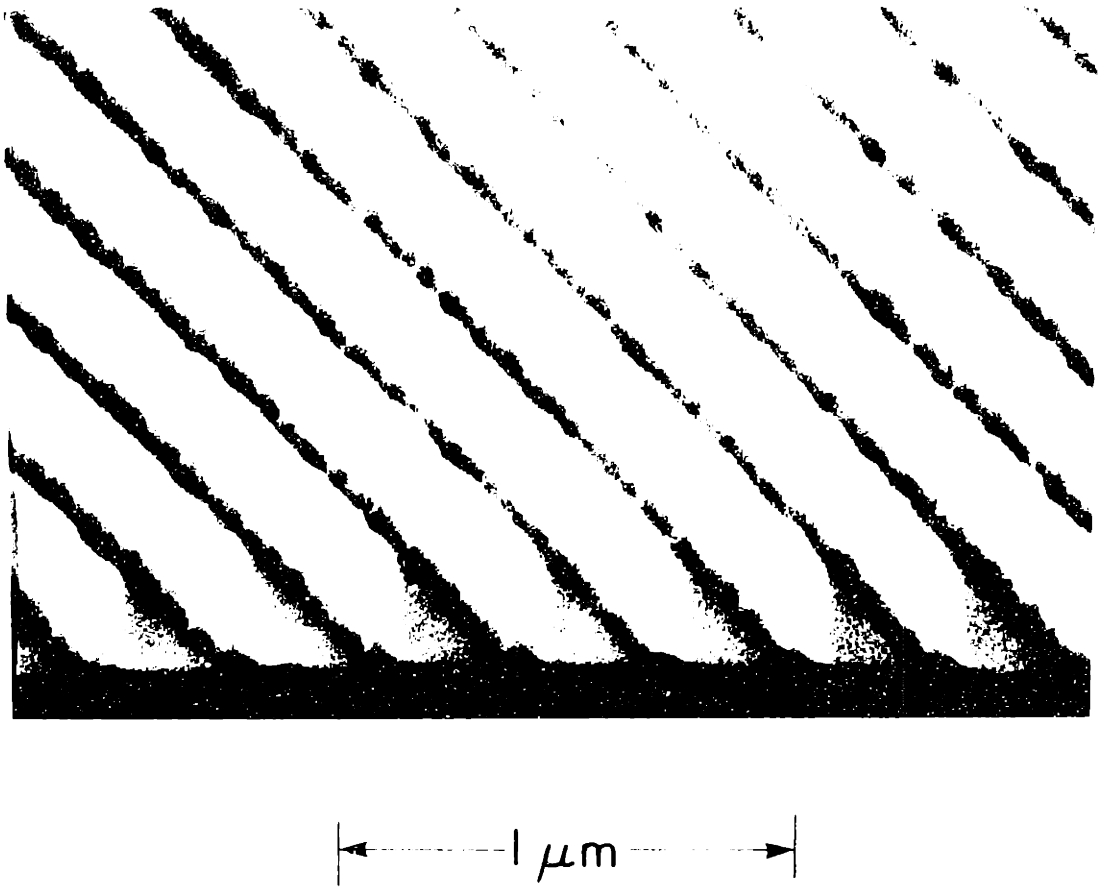
1 μm

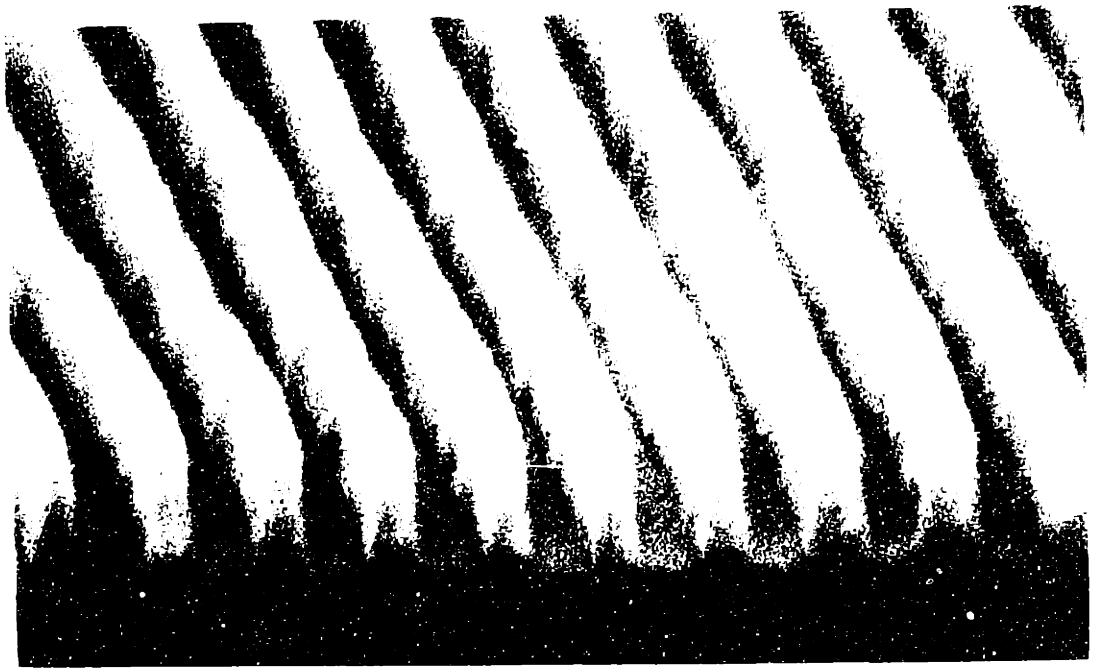

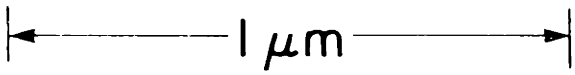
1 μm

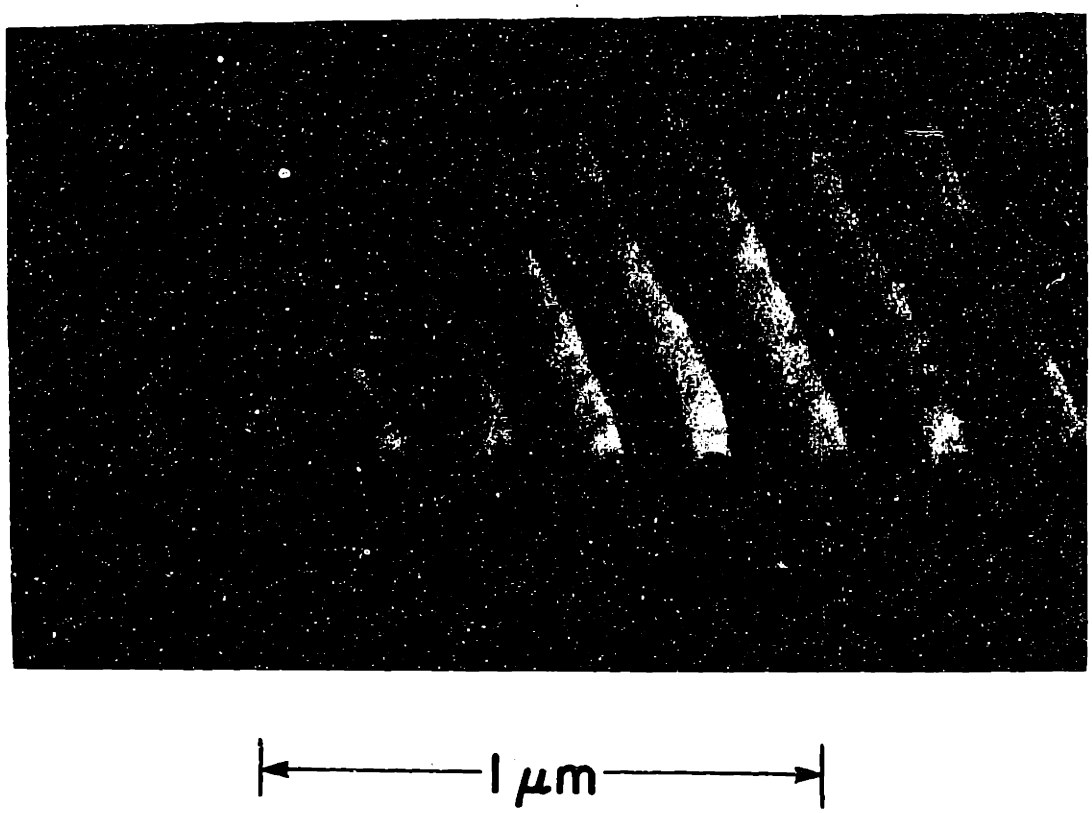

Figure II-20 A scanning electron micrograph of a 199 nm period grating with ∿ 70 nm wide lines, in ∿ 0.25 μm PMMA.

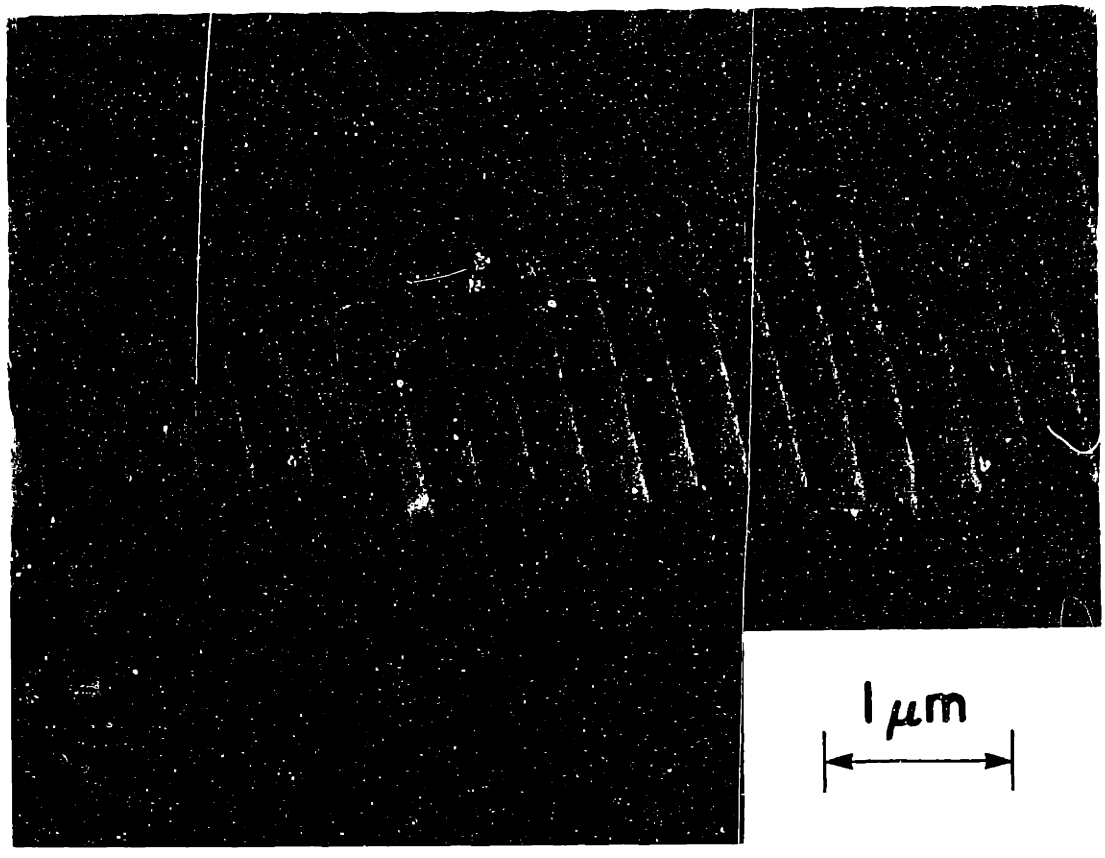

Figure II-21 A scanning electron micrograph of a 300 nm period grating, with ~ 150 nm wide lines, in ~ 0.7 μm PMMA.

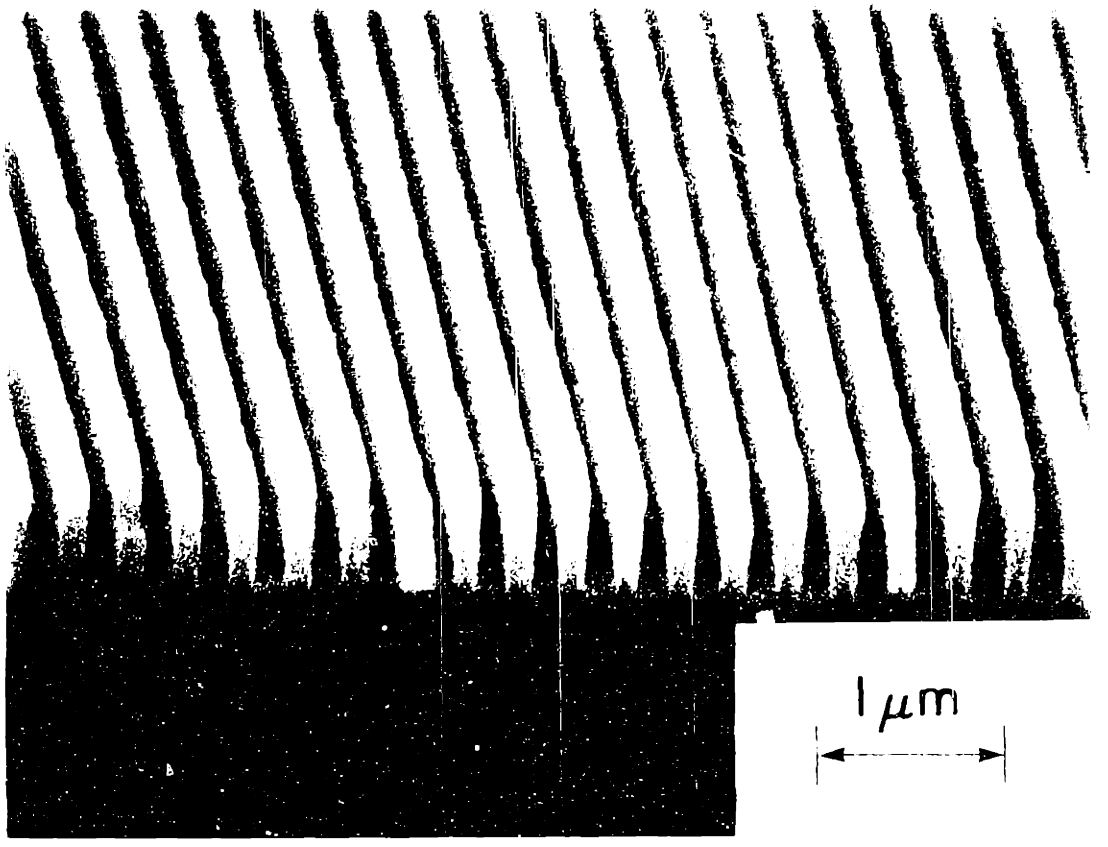

Figure II-21 A scanning electron micrograph of a 600 nm period grating, with 150 nm wide lines, in [illegible].

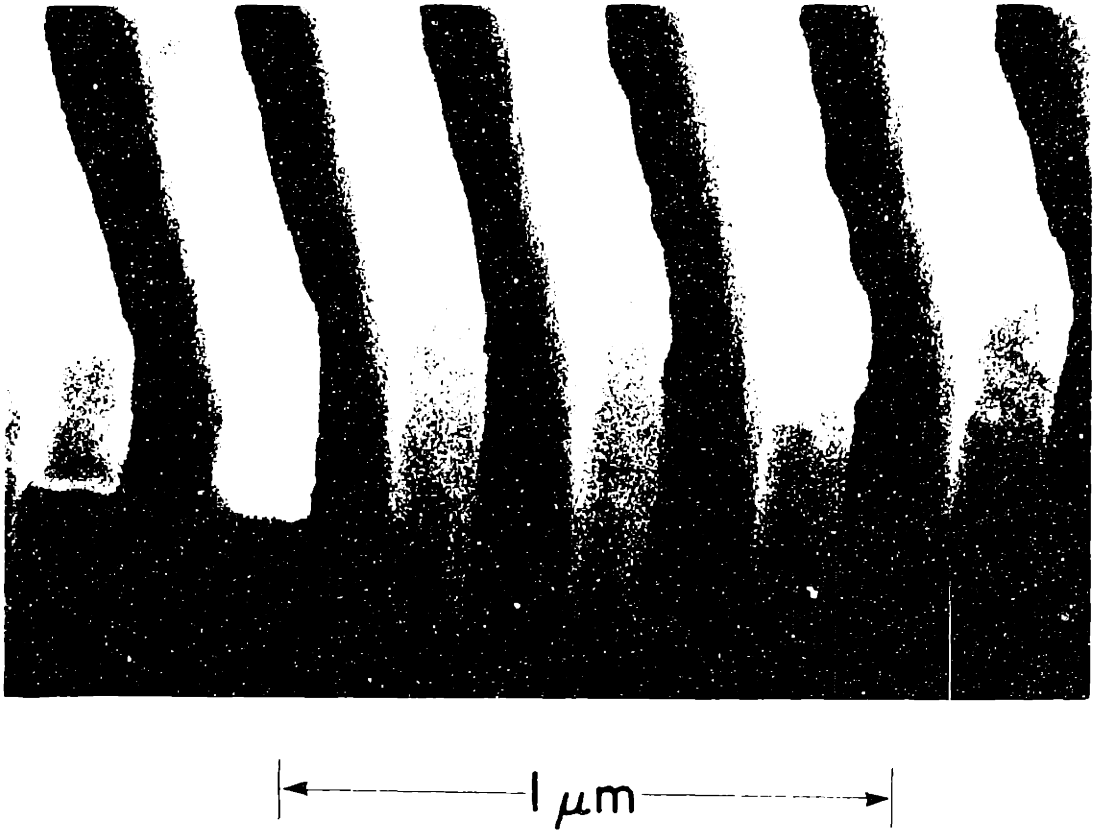

Figure II-3 High-magnification scanning electron micrograph of the grating in Figure II-2. Note the straightness of the sidewalls and the high aspect ratio of the structure.

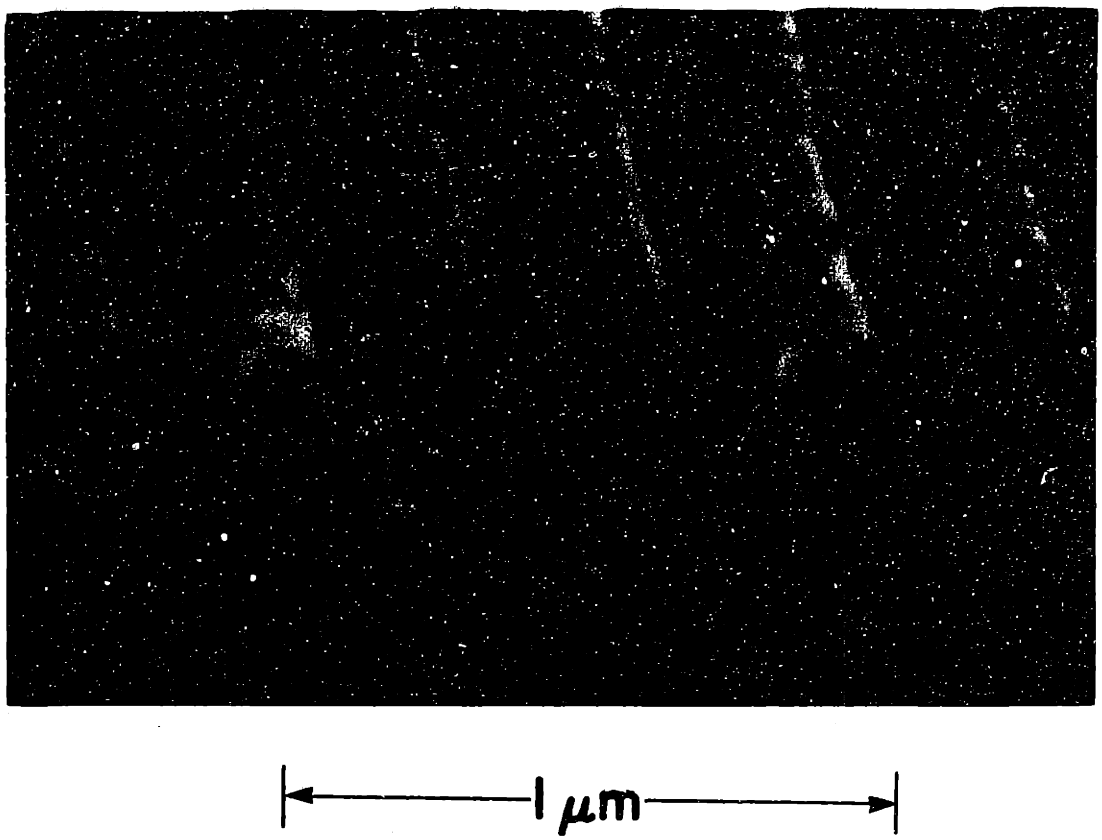

Figure II-22 High-magnification scanning electron micrograph of the grating in Figure II-21. Note the straightness of the sidewalls and the high aspect ratio of the structure.

II-D-4 Microplating (Electroplating) to Produce Thick Gold Gratings

Electroplating is a century-old technique that has been used extensively in a number of areas ranging from decorative jewelry to electrical contacts for semi-conductor devices.[27] Electroplating allows one to produce thick gold films by placing the sample to be plated into an appropriate bath, and electrically driving gold ions from the bath solution onto the sample. This is done by making the sample electrically more negative than the intrinsic (zero bias voltage) potential between the sample and the bath solution, Figure II-23. When a gold surface is initially placed into the plating solution, with no external voltage applied, gold ions diffuse off the surface and into the solution. This process continues until the surface charge becomes sufficiently negative to prevent further diffusion from the surface, and a steady state condition is achieved. To plate gold, the surface is simply driven more negative, and the gold ions in the plating solution are now attracted to the cathode. This process is continued until the desired plating thickness is achieved.

For the purpose of producing thick gold gratings, a PMMA grating "mold" was used. The PMMA grating was first placed in an oxygen plasma for 5 seconds to remove any organic contamination that may be residual on the surface of the gold plating base. When a substrate with a PMMA grating structure on the surface was subjected to gold plating, gold plated at all locations where the gold plating base was exposed, specifically between the PMMA grating lines. This process was continued until the desired gold thickness was achieved. Obviously, the PMMA lines must be taller than the desired gold grating. When the desired gold thickness was achieved, the PMMA lines were dissolved in chlorobenzene, followed by another 60 seconds

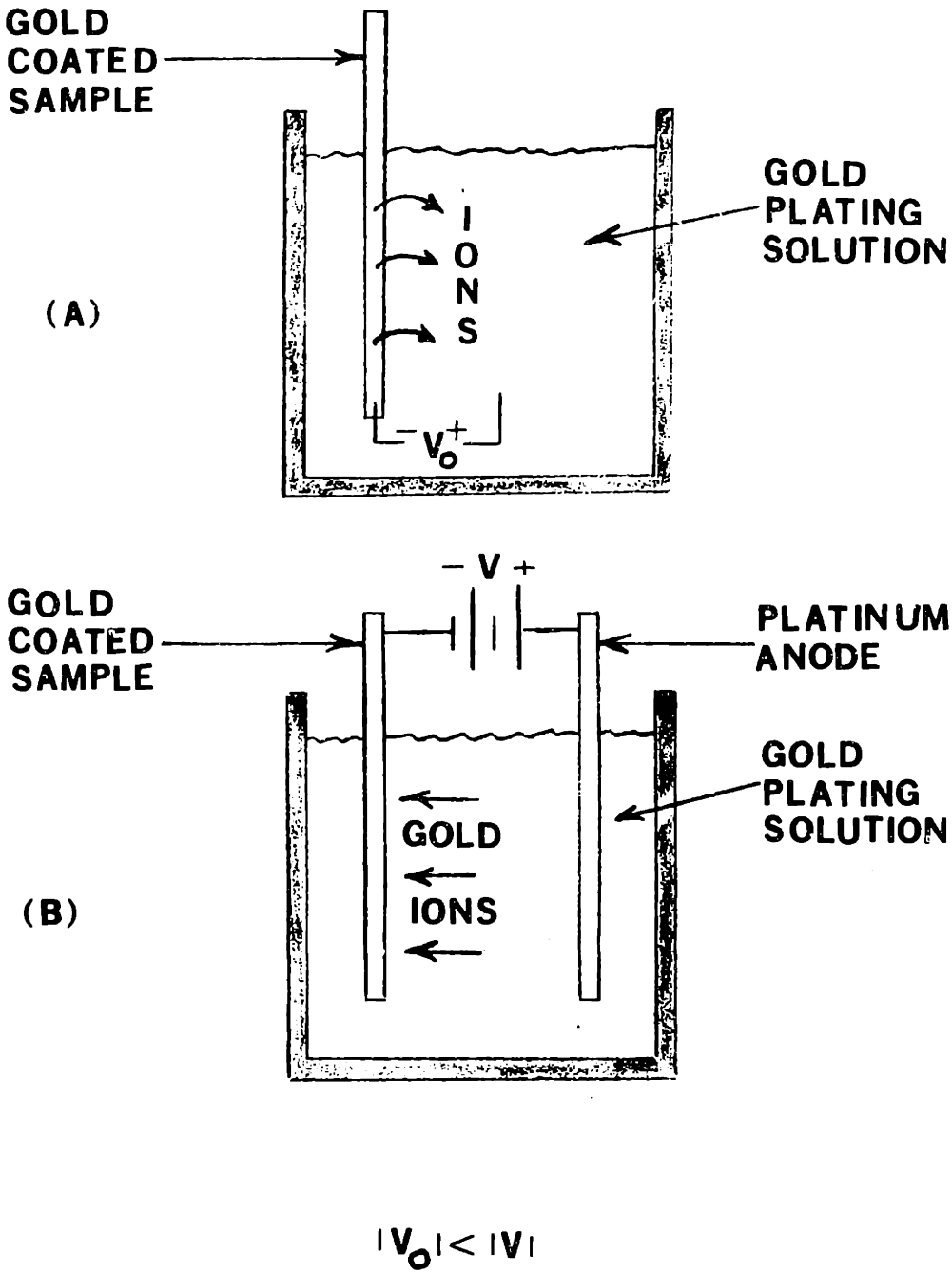

Figure II-23 Placing a gold coated sample into a plating solution drives some gold ions from the surface and into the solution (A). When a bias voltage is applied (B), gold from the solution is driven onto the sample surface.

in an oxygen plasma. Figure II-24 shows a 300 nm spatial period gold grating that was microplated to a gold thickness of 0.65 μm. This result was obtained by using a commercial plating bath, Sel-Rex BDT-510 gold plating solution,[50] with a current density ∿ 1 ma/cm^2, a bath temperature of 45°C, and a bath pH of ∿ 8.5. A slow (∿ 10 nm/min) plating rate gave the best results. Plating at faster rates tended to result in non-uniform plating rates over the surface of the sample.

II-E SUPPORT STRUCTURE FOR THICK GOLD GRATINGS

For obvious reasons, the support structure for the thick gold transmission diffraction gratings must itself be transmissive to the incident x-rays. There are two ways to achieve this; the first utilizes a thin, x-ray transparent membrane and the second uses a grid or random array support pattern. The advantage of the membrane is that none of the actual grating area is obstructed, but there are problems associated with the absorption in the membrane. Any strong absorption edges in the membrane will degrade the overall performance of the grating; membrane transmission is, of course, wavelength dependent. The second support structure uses a coarse gold grid network to hold the submicron period grating together. This will obstruct some fraction of the grating area, and hence the overall transmission will be lowered, but the performance will be wavelength independent. Both support structures have been made.

Polyimide was used as the support membrane for a thick gold diffraction grating on an x-ray transparent substrate. A silicon wafer was first spun with a 0.5 μm thick layer of polyimide, and then coated with a 10 nm chromium and 10 nm gold layer for the plating base. A 0.7 μm thick PMMA

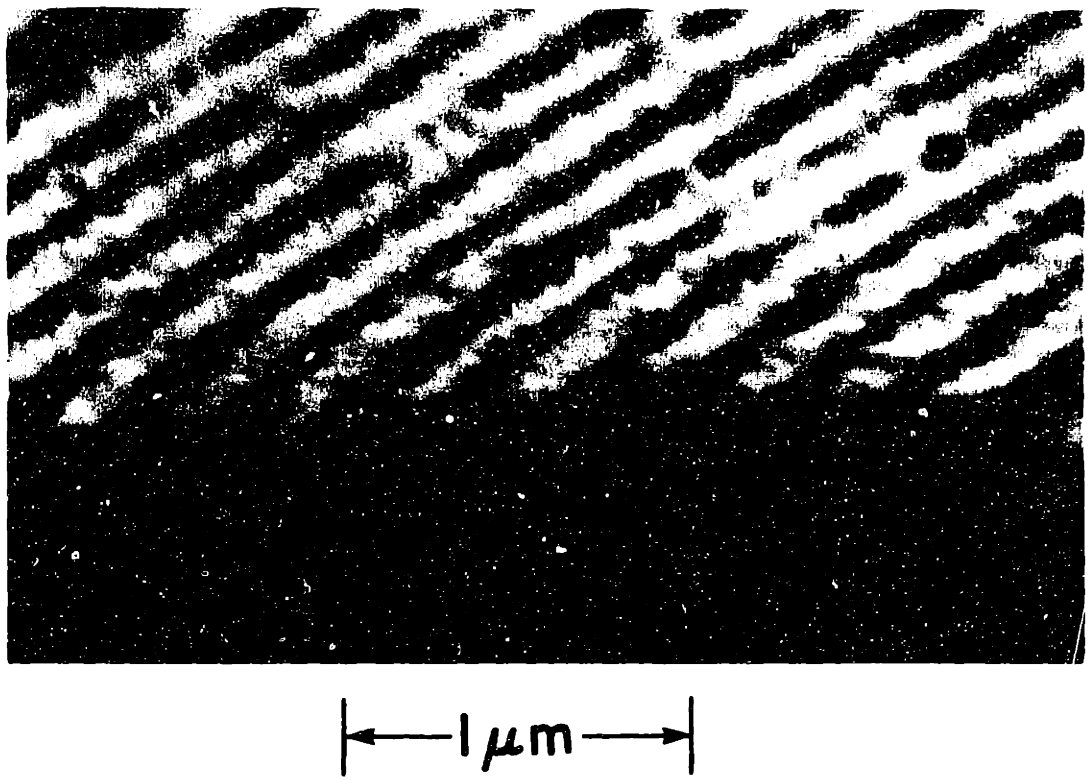

Figure II-24 A scanning electron micrograph of a 300 nm period gold grating, 0.65 μm thick. The PMMA grating mold has been dissolved away.

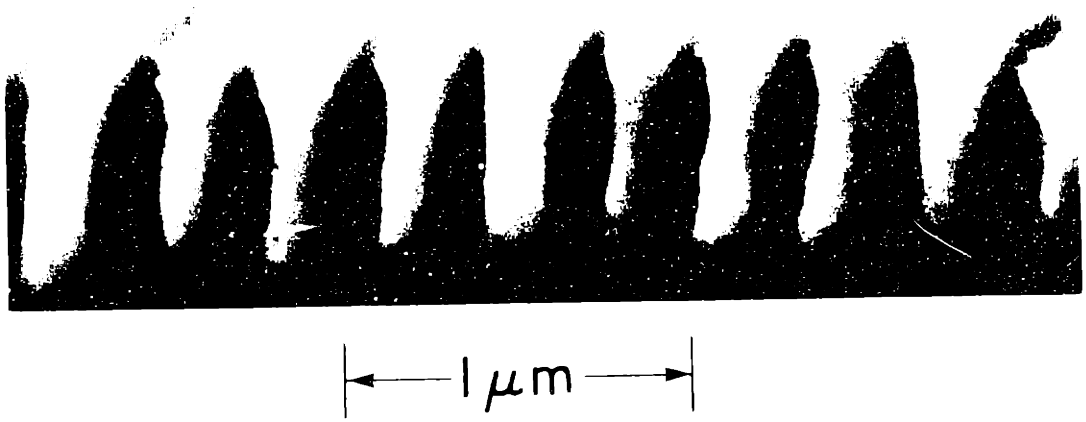
1 μm

layer was then spun onto the gold. Subsequent x-ray exposure and development and gold microplating resulted in the thick gold grating seen in Figure II-24. The polyimide was then epoxy bonded to a PVC tube, leaving the back side of the silicon wafer exposed. Black wax was painted onto the silicon at all locations where the removal of the silicon was not desired. The wafer was then placed in a solution of 97% hydrofluoric acid and 3% nitric acid, to etch the silicon from behind the gold grating area and in an annular pattern with a one inch inside diameter. When the etching was completed, a razor blade was used to cut through the polyimide in the annular ring to release the center structure. The final result was a gold grating on a polyimide support membrane on a one inch diameter silicon ring. The exposed gold grating area was approximately 7 millimeters in diameter.

To produce a "free-standing" grating without a support membrane, it was necessary to add a coarse grid structure to the pattern. This was done, in collaboration with D. Ciarlo of the Lawrence Livermore Laboratory, by producing a thick gold grating on a silicon wafer as before, but without any intermediate polyimide layer. A 0.5μm thick layer of AZ 1350B photoresist, followed by a 3 μm thick layer of AZ 1350J photoresist was spun onto the gold grating. The first layer of resist was a low viscosity resist, and this insured that resist would flow in between the gold grating lines. The second layer was spun to obtain the desired resist thickness. A 6 μm period grating and a 160 μm period grating with lines oriented perpendicular and parallel to the 300 nm period gold grating respectively, were exposed photolithographically. This resist pattern was then gold microplated to a thickness of approximately 3 μm, to produce a gold grid

pattern with approximately 30% of the area of the 300 nm period grating unobstructed, Figure II-25. The line-to-period ratio of the 6 μm and 160 μm gold plated gratings were ∿ 5:8 and 1:8, respectively. The silicon support wafer was then etched as before (using 97% HF and 3% HNO_3) to remove the silicon from behind the grating area.

II-F PROCEDURE TO PRODUCE VERY THICK (> 1 μm) GOLD GRATINGS

II-F-1 Exposing Thick (> 1 μm) PMMA

With the success achieved with the 0.65 micron thick, 300 nm spatial period gold gratings, an attempt was made to produce far thicker (1 to 2 μm) gold gratings with the same spatial period. This would produce a grating with more contrast for soft x-ray spectroscopy, and would extend the useful range of the grating to include x-ray energies in excess of 10 eV. Towards this goal, the same procedure already outlined in this chapter was followed with the exception that the PMMA thickness was increased from 0.7 to 1.8 μm. When the PMMA was exposed and developed, lack of optical diffraction from the sample indicated that the quality of the grating was severely compromised. An SEM study of the sample revealed that the individual PMMA lines were no longer structurally capable of supporting these extremely high aspect ratios (> 10:1), and the PMMA lines were leaning on their nearest neighbors, Figure II-26. Clearly, this is undesirable, and cannot be used for further processing. In general, PMMA structures with aspect ratios greater than $\gtrsim$ 7:1 could not be produced reliably. For a 300 nm period grating (150 nm lines) this limited the PMMA thickness to ∿ 1 μm.

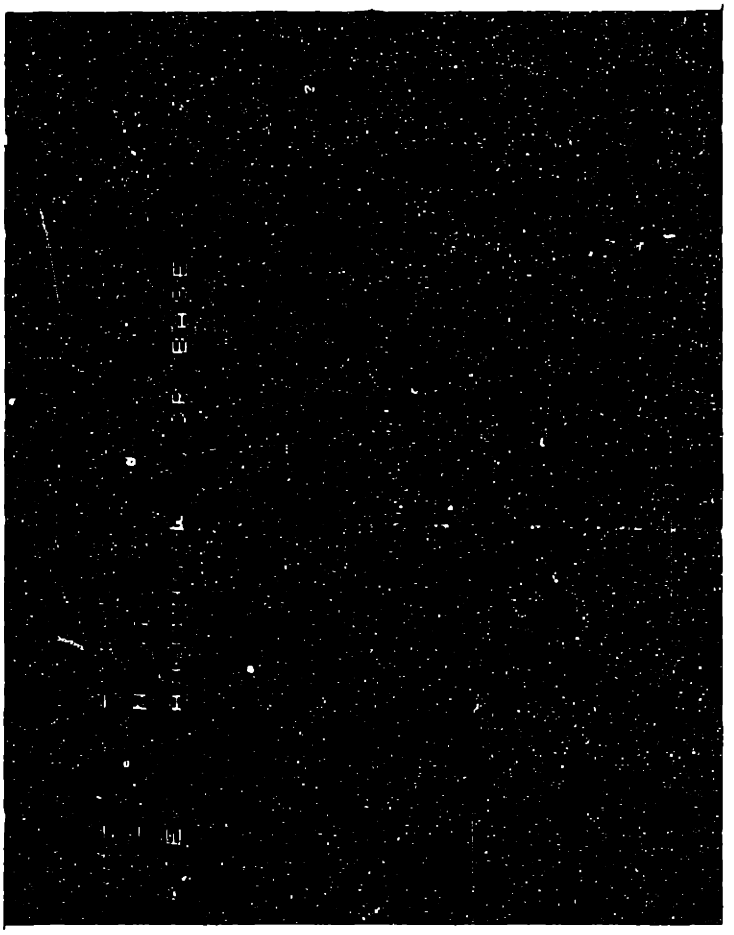

Figure II-25a SEM micrograph of a 0.3 μm period, ∿ 0.5 μm thick, gold transmission diffraction grating, with a gold grid pattern for the support structure. At this magnification the 0.3 μm period grating lines can be seen orthogonal to the 6 μm period grating lines.

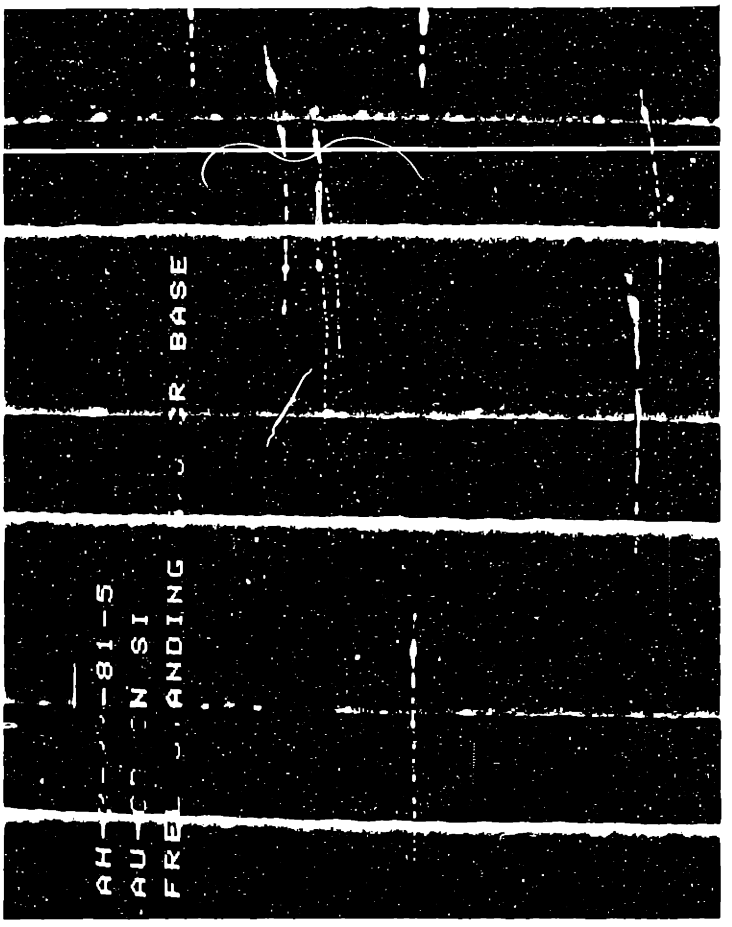

Figure II-3a SEM micrograph of a 0.3 μm period, 0.5 μm thick, gold transmission diffraction grating, with a gold grid pattern for the support structure. At this magnification the 0.3 μm period grating lines can be seen orthogonal to the 6 μm period grating lines.

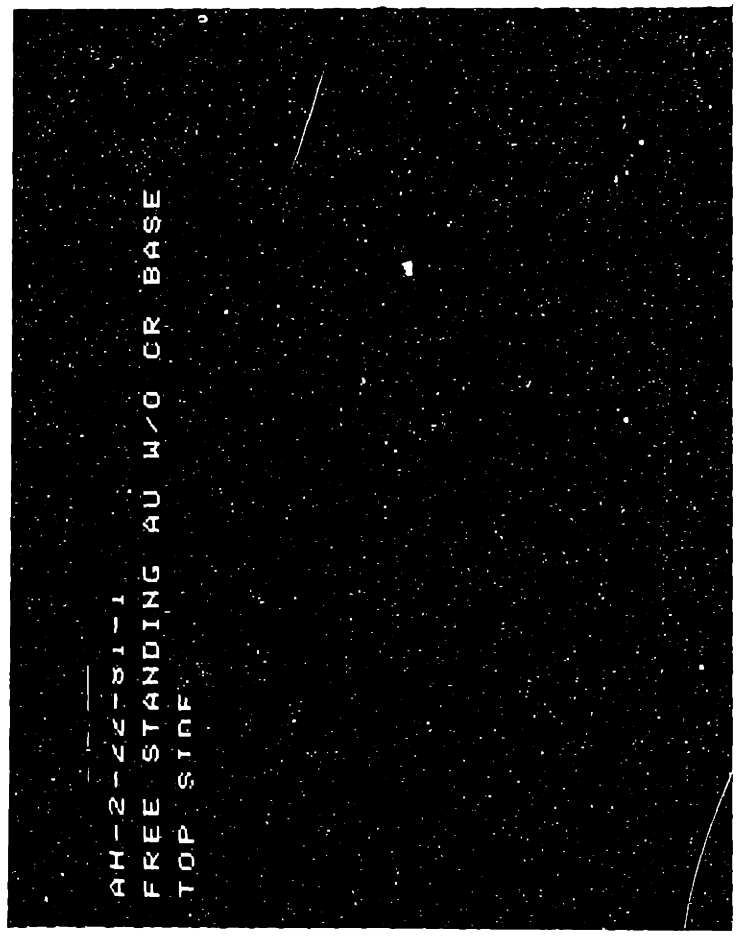

Figure II-20b An SEM micrograph of a 0.3 μm period, 0.5 μm thick, gold transmission diffraction grating, with a gold grid pattern for the support structure. At this magnification the 0.3 μm period grating cannot be seen. The 100 μm period grating lines are seen as being orthogonal to the 6 μm period grating.

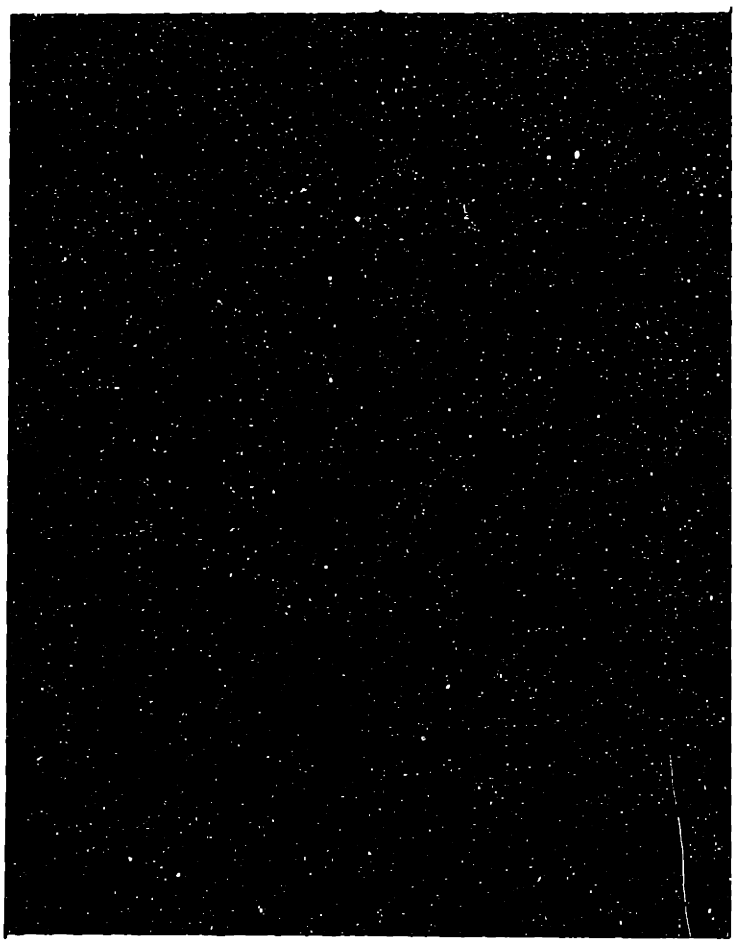

Figure II-25b An SEM micrograph of a 0.3 μm period ∿ 0.5 μm thick, gold transmission diffraction grating, with a gold grid pattern for the support structure. At this magnification the 0.3 μm period grating cannot be seen. The 160 μm period grating lines are seen as being orthogonal to the 6 μm period grating.

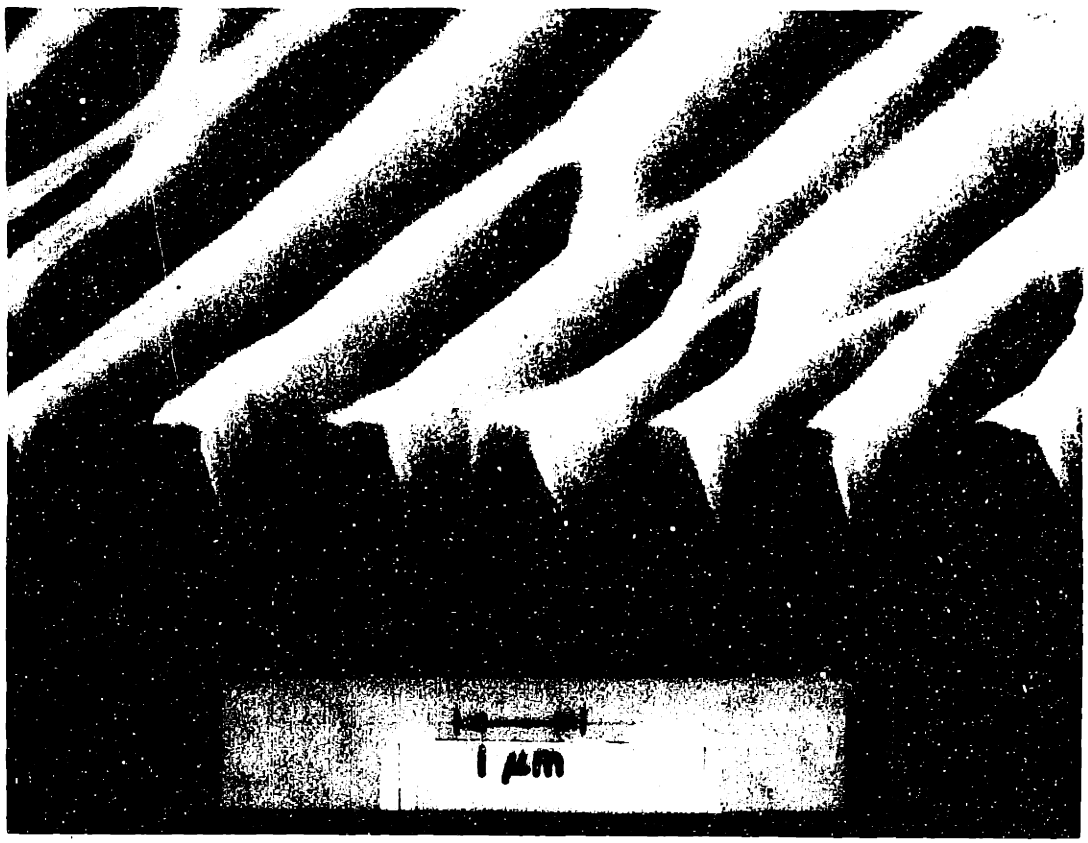

Figure II-26 A scanning electron micrograph of a 300 nm period grating in 1.8 μm thick PMMA. The high aspect ratio lines do not have the structural integrity to support themselves.

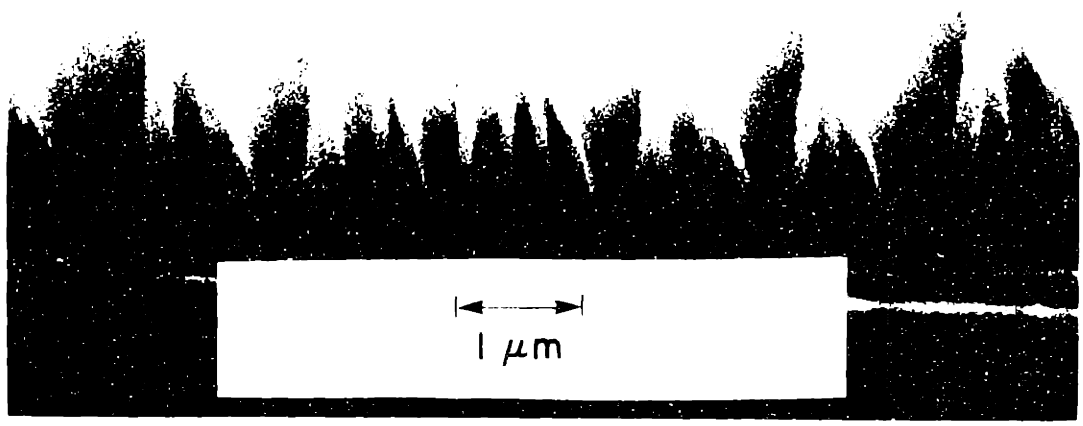
1 μm

II-F-2 Reactive Ion Etching of Polyimide

To produce gratings with aspect ratios > 10:1, a material with more structural integrity than PMMA had to be used as the mold for microplating. Towards this end, a series of experiments designed to characterize the etching properties of polyimide were conducted. The technique of reactive-ion-etching (RIE) was shown by several workers to yield extremely straight sidewall structures in carbonaceous materials, when etched in an oxygen plasma.[51,57]

A schematic illustration of the RIE apparatus is shown in Figure II-27. Reactive ions are accelerated toward the target plate by a negative self-bias voltage. A sample placed on the target plate (the cathode) will then be etched by the ions. The by-products of the reaction are gaseous and are pumped out of the chamber by the vacuum pump.

To test this approach, a sample was prepared with a 10 nm chrome, 10 nm gold plating base, a 1.8 μm thick layer of polyimide spun onto the plating base, and a 0.25 μm thick layer of PMMA spun onto the polyimide. Using x-ray lithography, a 300 nm spatial period grating was replicated into the PMMA. A 50 nm chromium liftoff was then performed, so that a 300 nm period, 50 nm thick chromium grating would act as the mask for the subsequent polyimide etch. The sample was then etched in the RIE for 10 minutes at a power density of 0.25 W/cm^2, a 500 volt bias voltage, a pressure of 10 microns and an oxygen flow into the chamber of 15 standard cubic centimeters per second. The polyimide was etched until it was removed from a large monitor area adjacent to the grating area, at which point, the sample was cleaved, gold coated and observed in the SEM. Polyimide tends to stretch during cleaving, and it is necessary to cool the sample to liquid

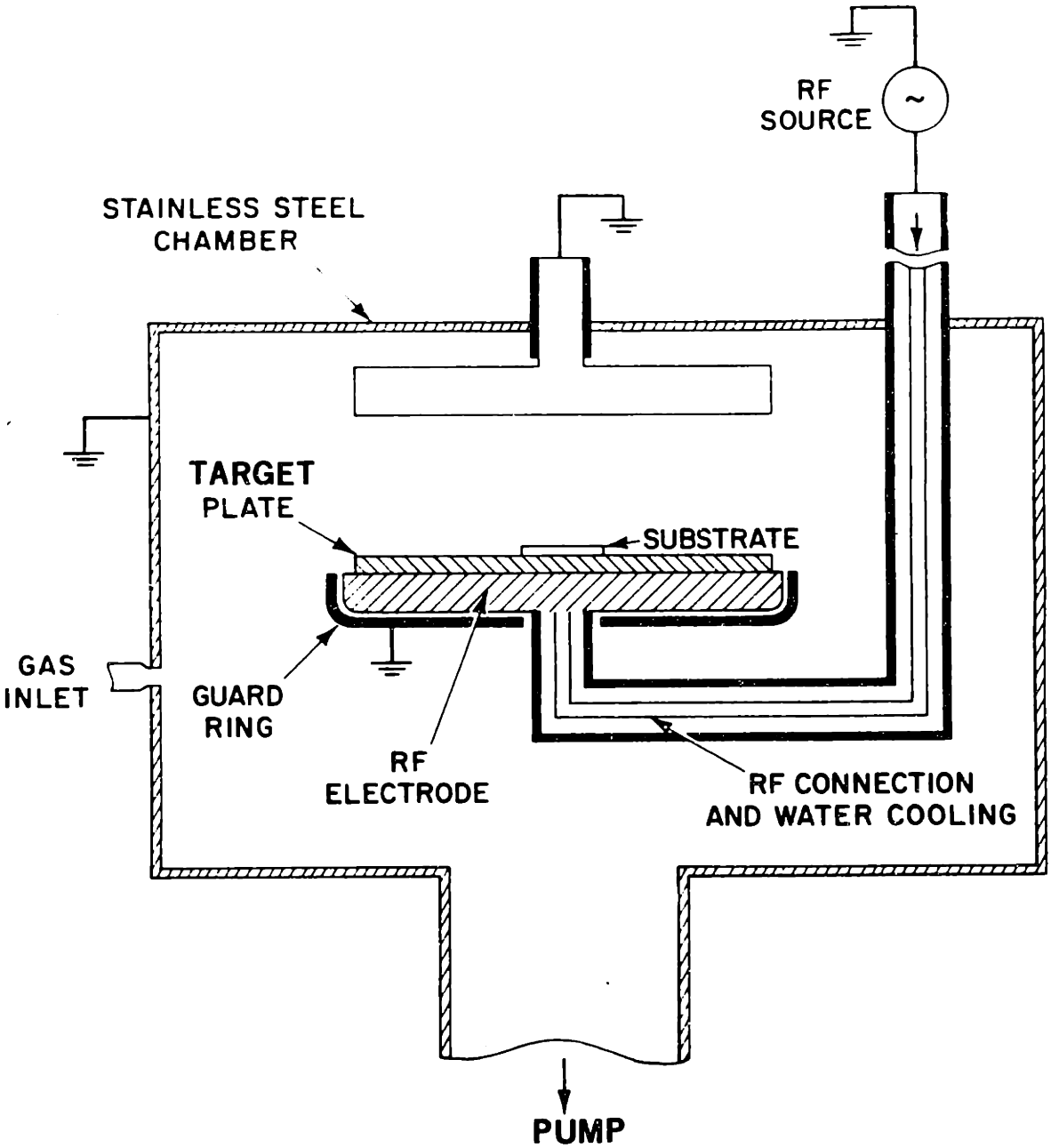

Figure II-27 Line drawing of a conventional reactive-ion etch apparatus.

nitrogen temperatures prior to cleaving, but even when this precaution is followed, the cleaved edge is still not sharp. However, Figure II-28 shows that the polyimide is capable of extremely high aspect ratios (> 10:1) and would make an ideal structure for the mold to produce thick gold gratings.

When gold microplating was attempted on this sample, it became clear that the plating process could not be initiated in the grating area. It was felt that a residual layer of material not readily etched by oxygen had contaminated the surface and was masking the gold plating base from the plating bath. This contamination layer would have to be removed before any plating could occur. Several attempts to remove the residual layer with an oxygen plasma, and with ion etching failed.

In an attempt to determine the cause of the residual layer, a series of experiments with structures of larger dimensions were performed. A zone plate pattern was an ideal test pattern for these etching tests because the zone plate lines become continually narrower at larger distances from the center. This will result in an etched pattern with a continually varying aspect ratio. In collaboration with N.M. Ceglio and G. Stone of the Lawrence Livermore National Laboratory, very thick ($\sim$ 50 μm) polyimide samples were prepared with a 1 μm thick aluminum zone plate pattern on the polyimide surface. The minimum linewidth of this zone plate was 5 μm. This sample was etched in the RIE until all the polyimide was removed from the large monitor areas. The sample was then observed in the SEM, where mesas were seen throughout the sample, Figure II-29. It was felt that the formation of the mesas could be attributed to redeposition of material which is not readily etched in oxygen. Upon careful examination of the RIE system, it was evident that the quartz target plate was also being etched by

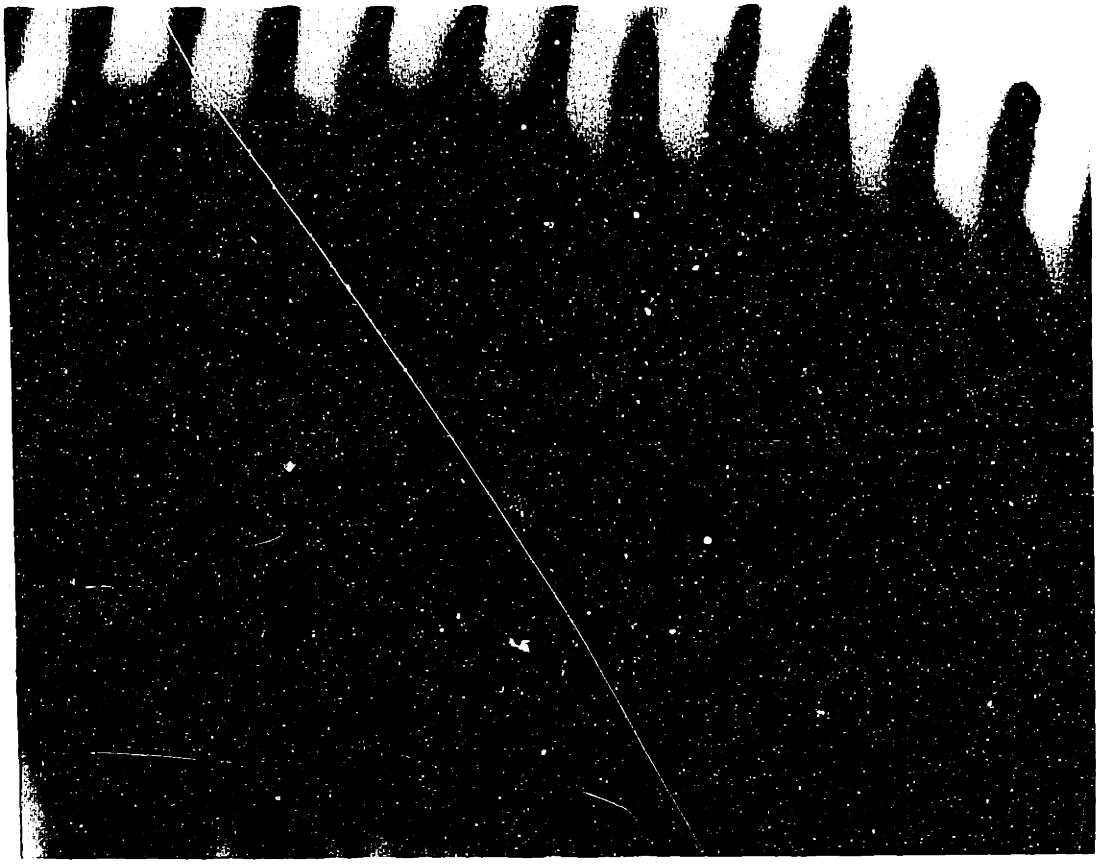

Figure II-28 Scanning electron micrograph of a 300 nm period grating etched by reactive ion etching into 1.8 μm polyimide.

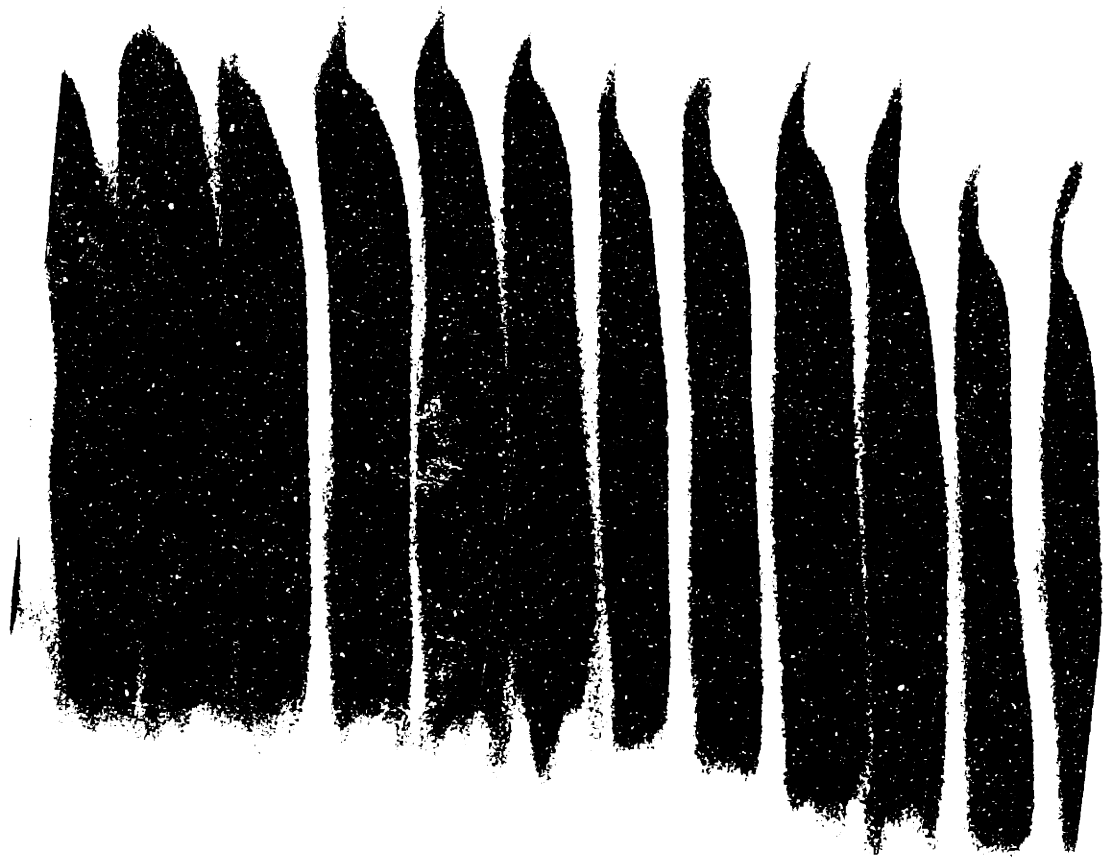
1 μm


SAMPL

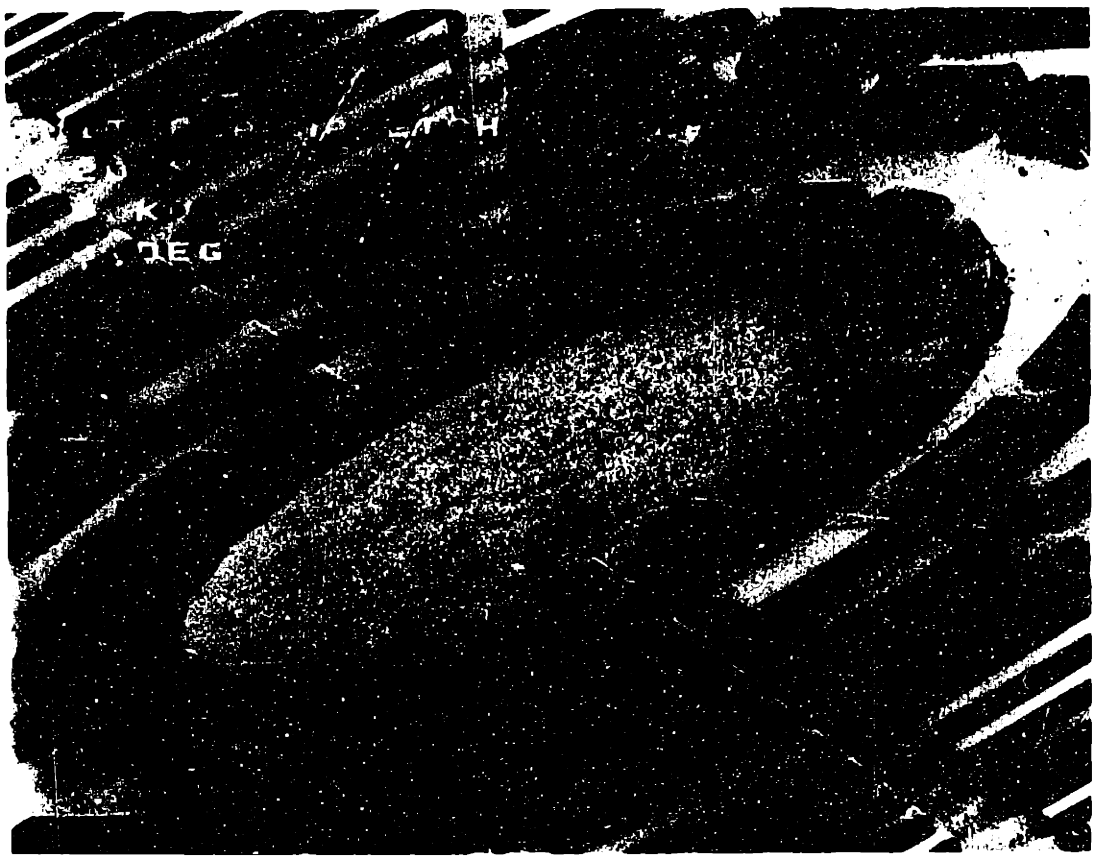

Figure II-29a Scanning electron micrograph of the center zones of zone-plate pattern, reactive ion etched into ∿ 50 μm of polyimide. Notice the mesas in the center of the pattern.

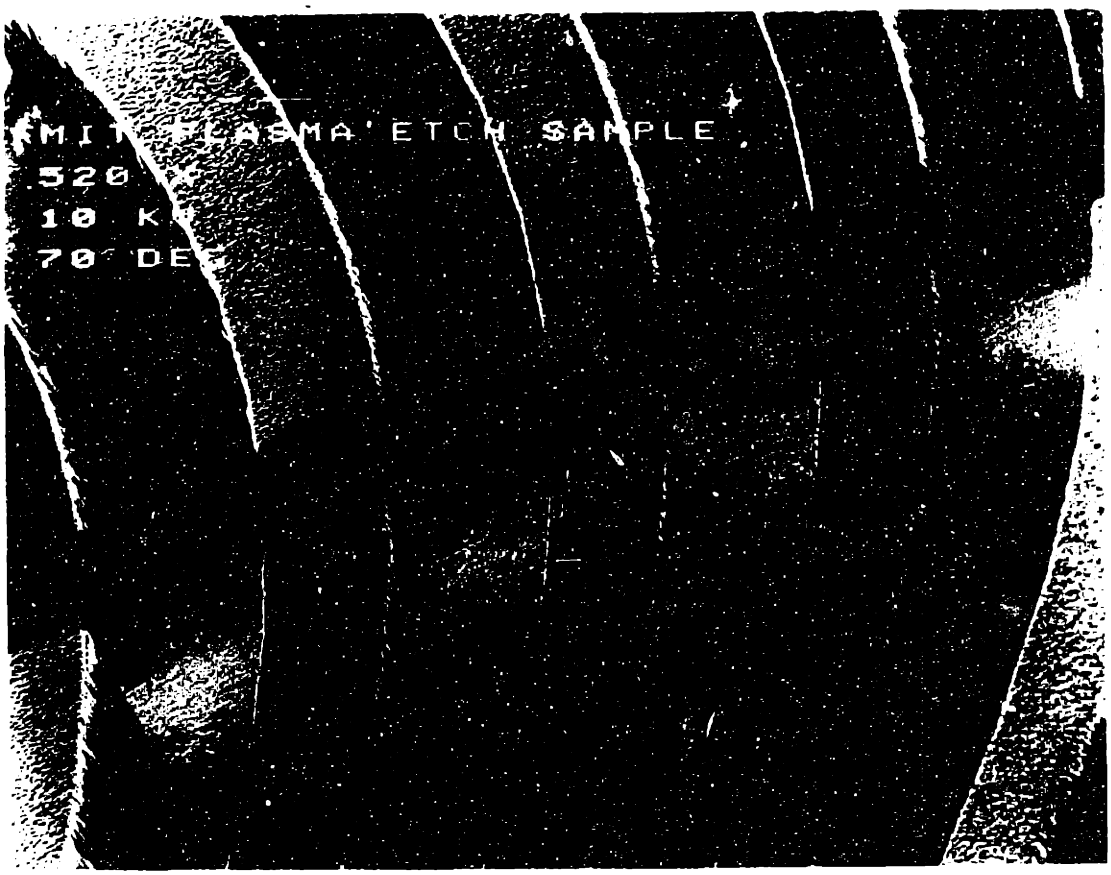

Figure II-29b Scanning electron micrograph of the zones in the middle of the zone plate pattern in Figure II-29a.

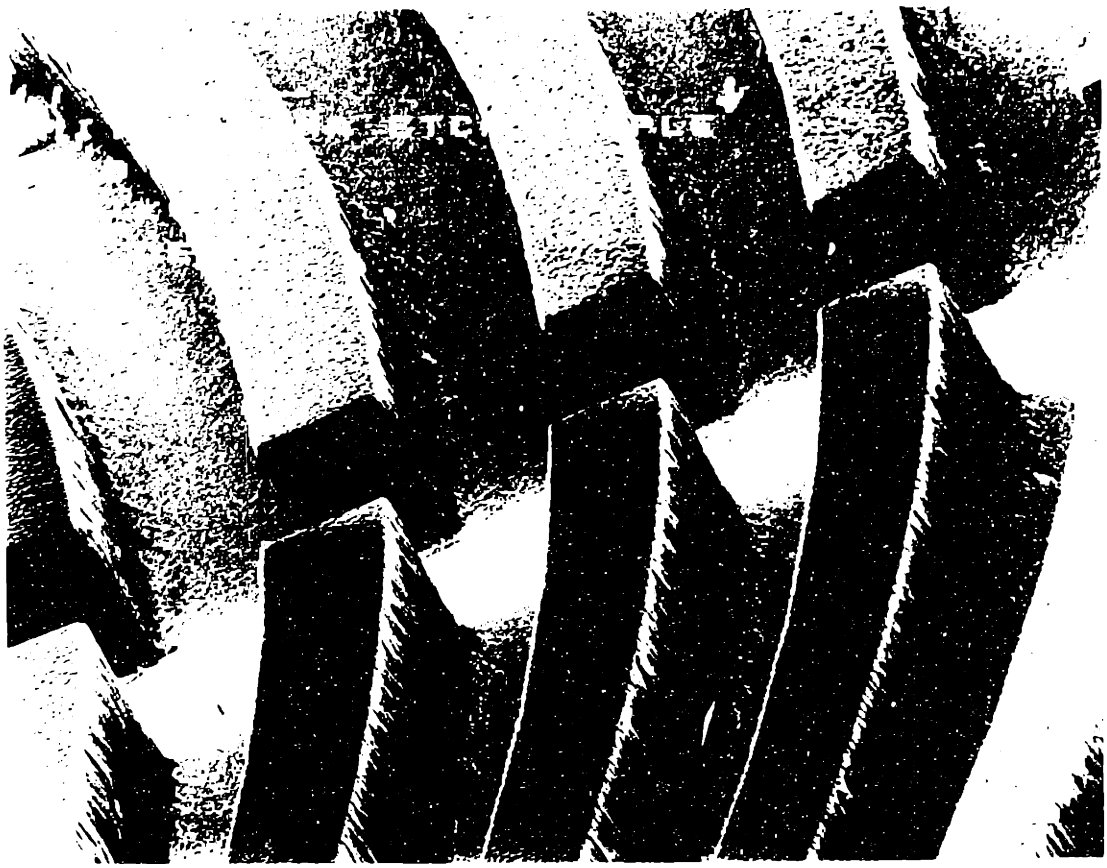

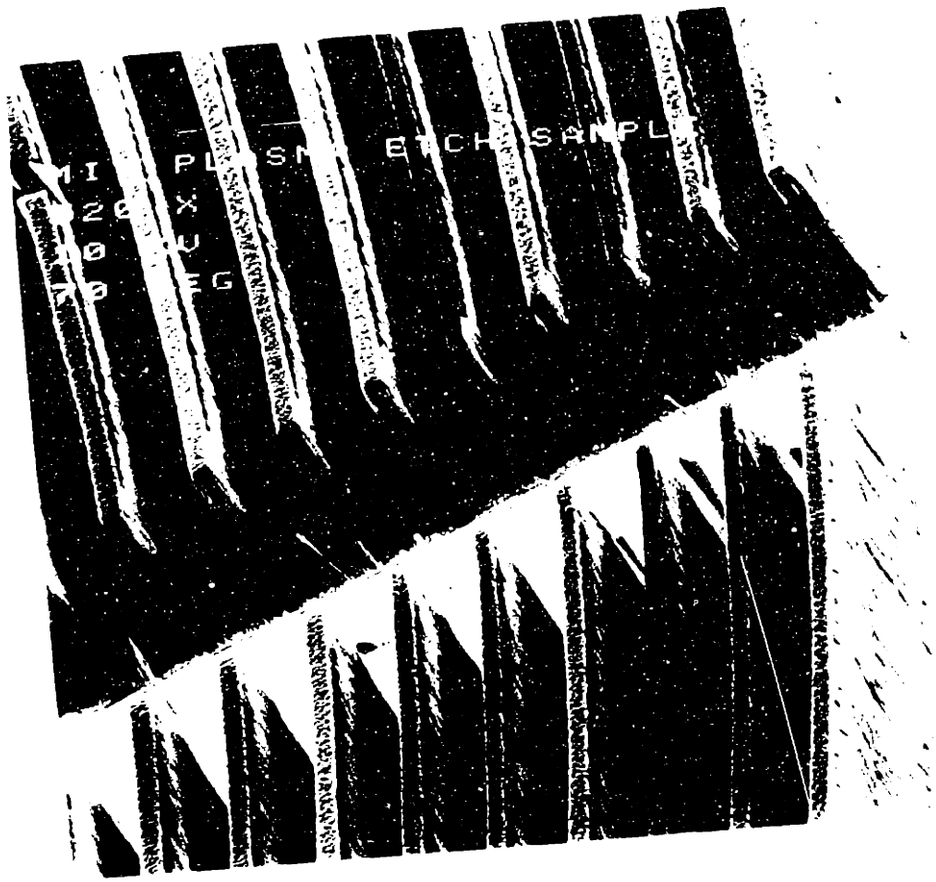
PLASMA ETCH SAMPLE
MIXED

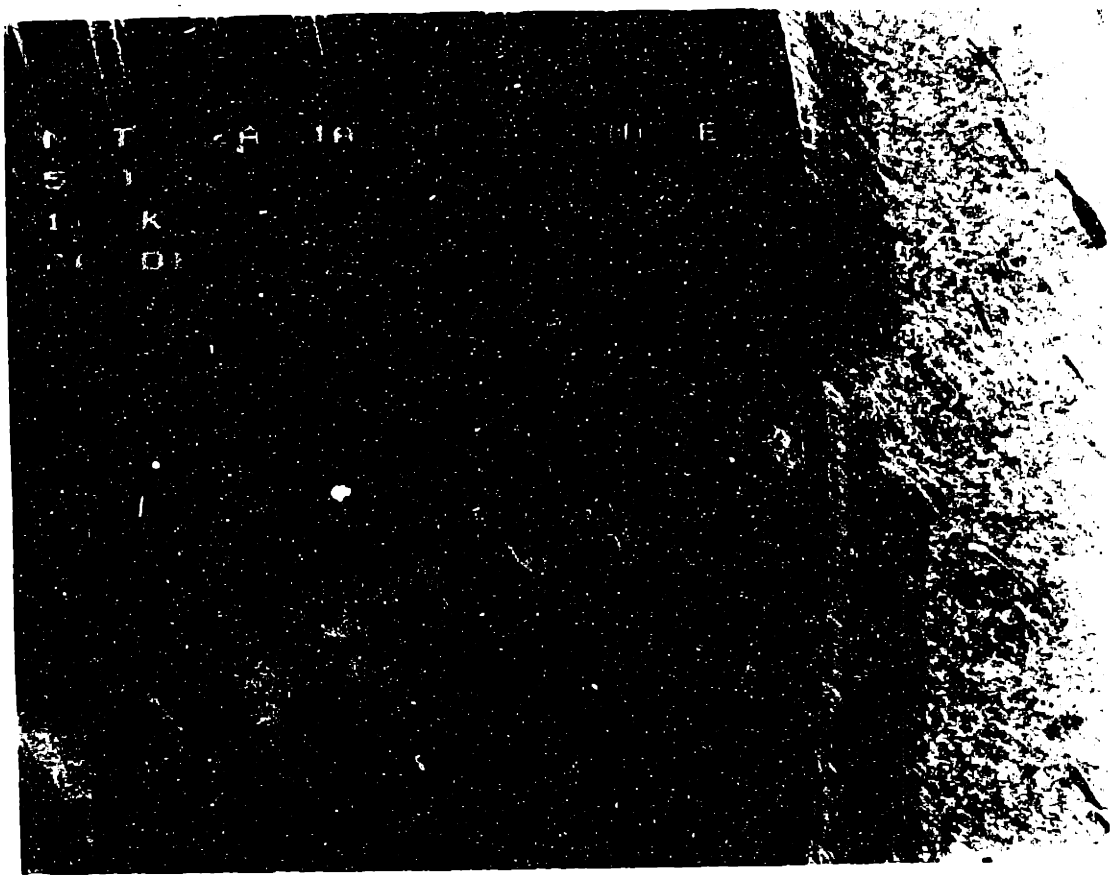

Figure II-29c Scanning electron micrograph of the outer most zones of the zone plate pattern in Figure II-29a. In this view, mesas are clearly evident.

sputtering, and the observed mesas could be a by-product redeposition of the sputtered quartz plate. Replacing tne quartz plate with an aluminum plate, coated with a 1 mm thick layer of polyimide, completely removed the mesas/redeposition problem, Figure II-30, and plating was later performed successfully on a similar sample,[57] Figure II-31. It is thought that this process can now be used to produce very thick gold gratings with aspect ratios > 10:1.

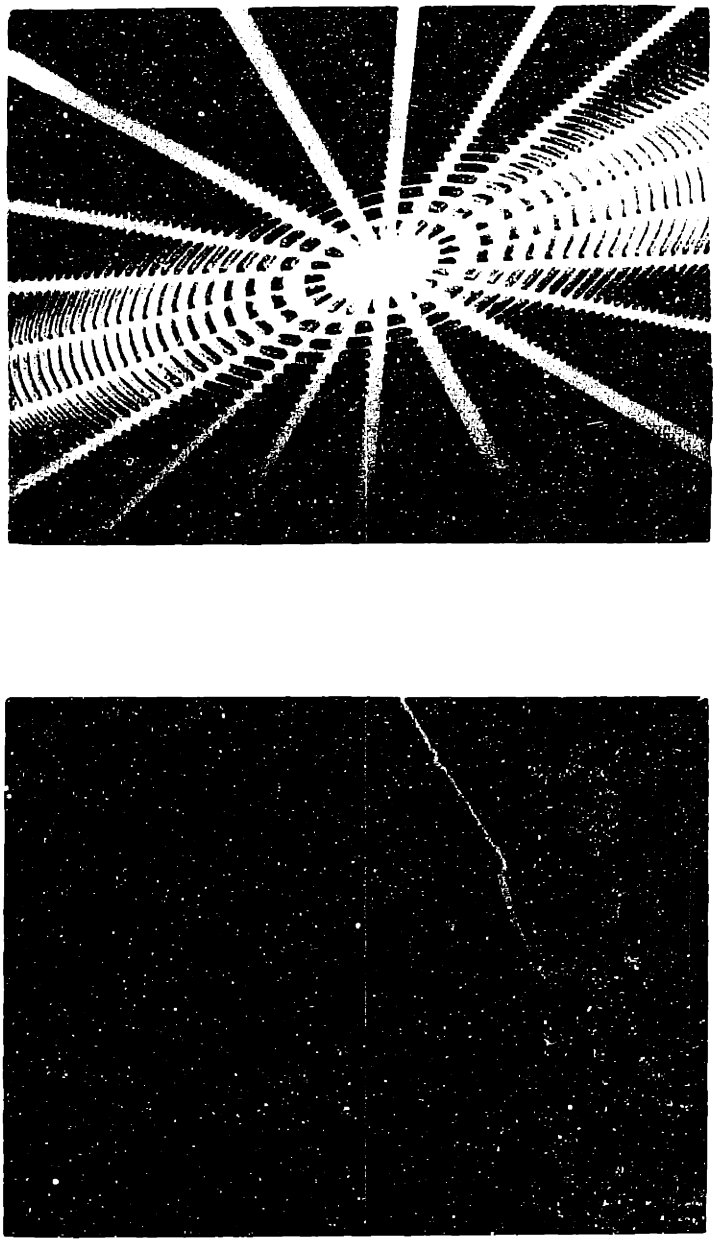

Figure II-30a Scanning electron micrograph of a zone plate pattern, reactive ion etched into 10 μm of polyimide, using a polyimide coated target plate in the R.I.E. Top: center zones, Bottom: outer most zones. Notice absence of mesas.

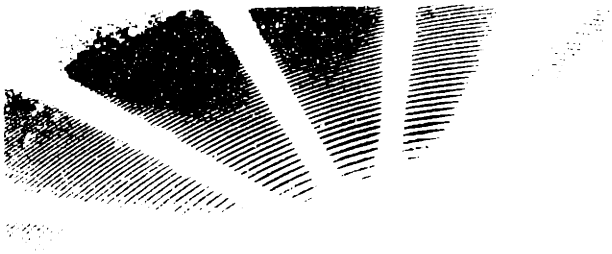

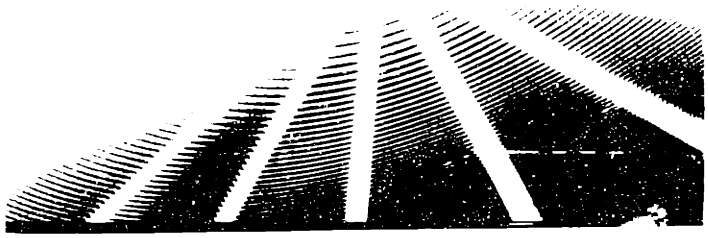

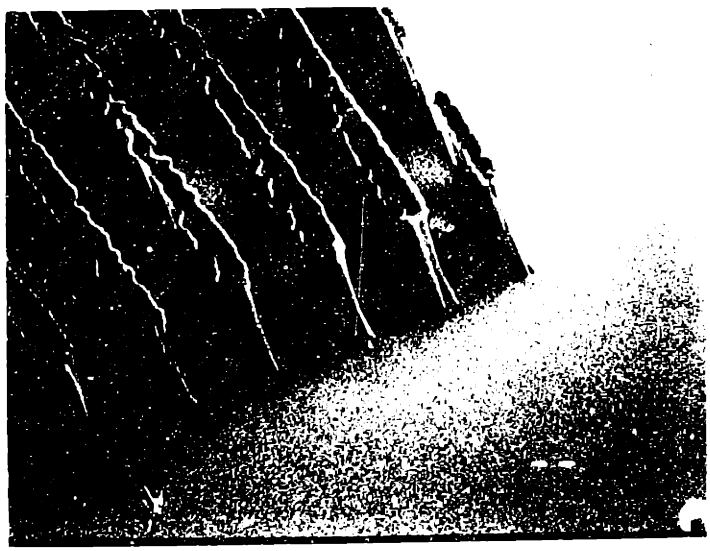

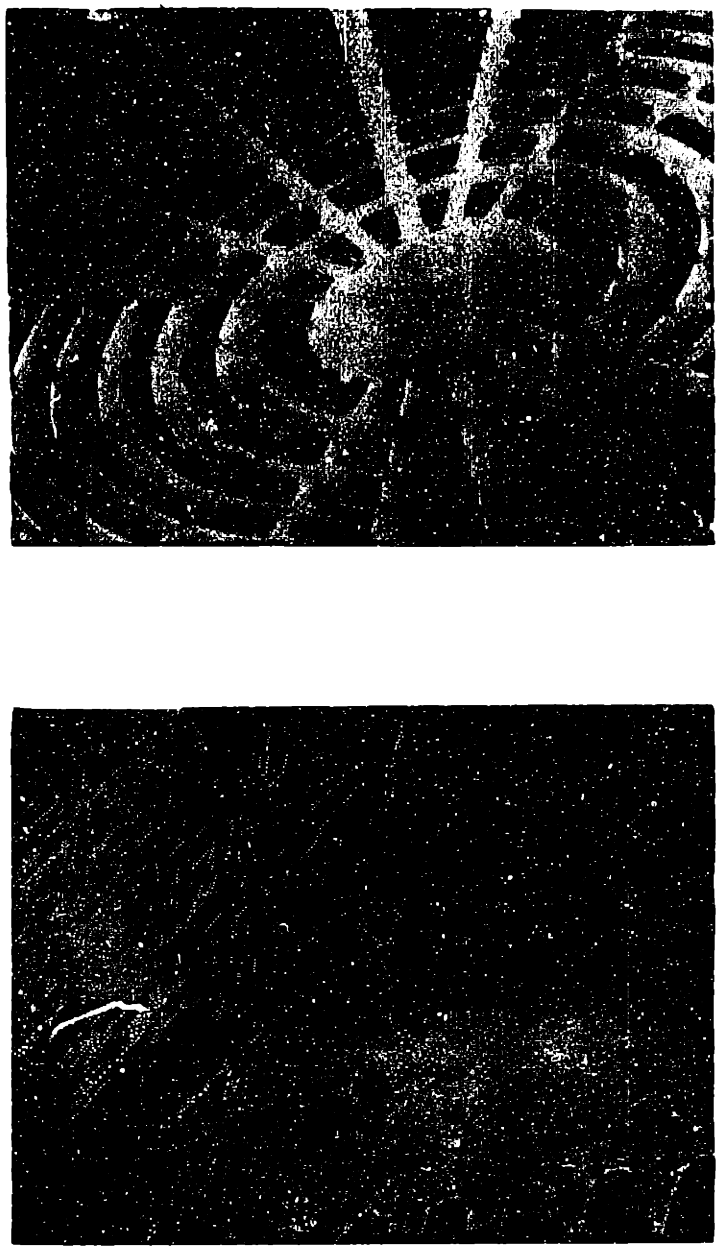

Figure II-30b Scanning electron micrographs of a zone plate pattern, reactive ion etched into 20 μm of polyimide, using a polyimide coated target plate. Top: center zones, Bottom: outermost zones. Notice absence of mesas.

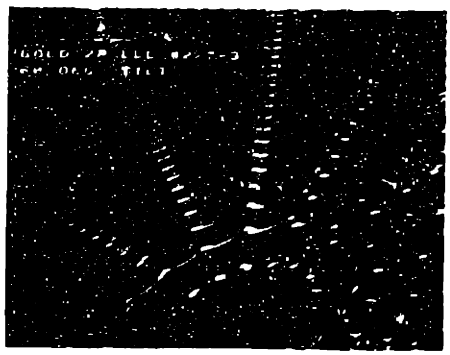

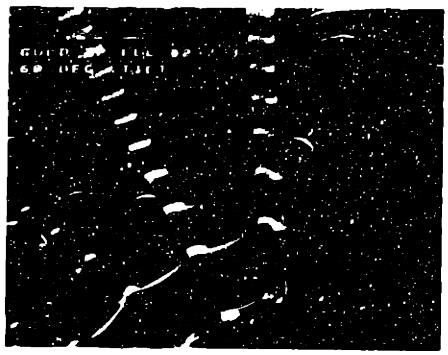

Zone plate parameters:

Thickness: 65 μm
Number of zones: 250
Min. zone width: 15 μm
Material: Electroplated gold

Figure II-31 Three SEM micrographs of a gold plated zone plate pattern, showing different areas of the zone plate. Gold plating was accomplished using reactive ion etched polyimide as the mold.

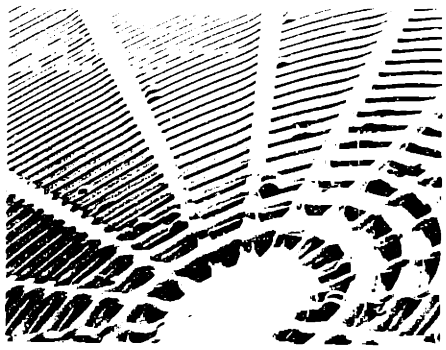

Zone plate parameters:

Thickness: 65 μm
Number of zones: 250
Min. zone width: 15 μm
Material: Electroplated gold

Figure II-8. Three SEM micrographs of a gold plated zone plate lens, showing different areas of the zone plate. Gold plating was accomplished using resist for etched silicon mold.

CHAPTER III

EXPERIMENTAL CHARACTERIZATION OF GRATING PROPERTIES

III-A INTRODUCTION

One of the purposes of producing thick gold gratings is to use them as a diagnostic tool to obtain spectral information of soft x-ray sources. By illuminating the grating with an x-ray source, it is possible to obtain the desired information from an analysis of the resultant diffraction pattern.[34,35,52] Before a grating can be used as a diagnostic tool, it must first be tested and characterized. Towards this end, it is necessary to measure the diffraction efficiency and the resolving power of a grating in the wavelength range of interest.

III-B CONSIDERATIONS FOR GRATING EVALUATIONS

When a grating is illuminated with some source of radiation, the observed far field diffraction pattern will be a convolution of the finite source size, finite source collimation, spectral linewidth and spectral resolution of the grating. A typical experimental arrangement is as depicted in Figure III-1, where the source consists of 3 distinct wavelengths and linewidths. Under the condition that the x-ray source is infinitesimally narrow in spatial extent, the width in the "y" direction of the zeroth order diffracted beam would be zero, and the width (Δy) of the individual spectral lines seen at the film plane would exactly correspond to the convolution of the finite linewidth of the source and the resolution of the grating. An ideal source for characterizing the performance of the gratings would be a collimated source with well-separated, narrow band

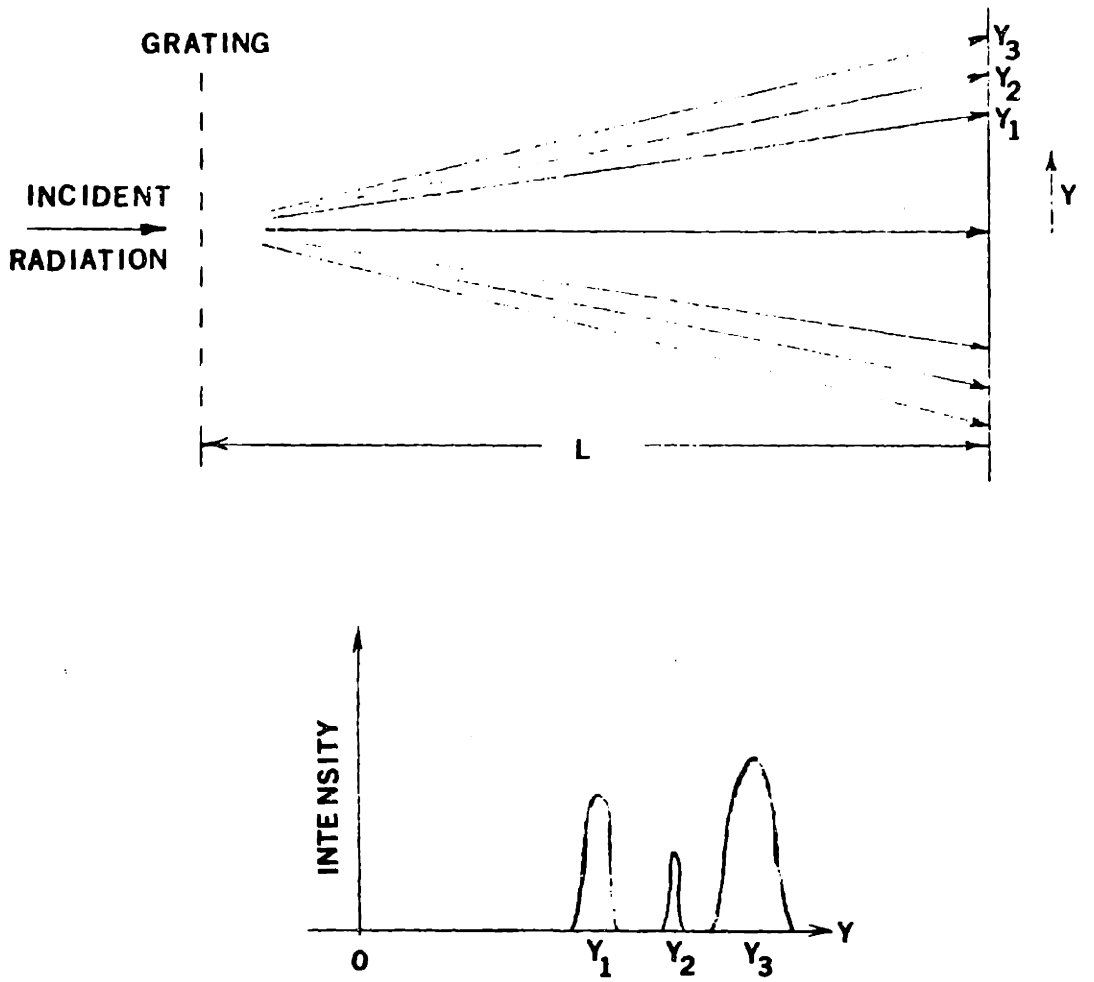

Figure III-1 Typical experimental conditions for grating evaluations and use. Incident x-ray radiation is diffracted by the grating and the far field diffraction pattern is observed on some x-ray sensitive device. In the above figure, the incident radiation consists of three distinct wavelengths with three different intensities and bandwidths.

spectral lines and with an infinitesimally small source size. Unfortunately, these goals are, in general, unattainable, and the diffracted beams that are recorded are a convolution of all the effects previously mentioned. These effects make it difficult to obtain an accurate measurement for the grating resolution, and will limit any measurement to a lower-bound limit. In theory, the resolving power of a grating, $\lambda/\Delta\lambda$, should be equal to the number of grating lines illuminated by the source.[34,52]

The effects on the system resolution of the finite source size and finite source collimation can be easily computed. For the case of a collimated, narrow bandwidth source with a finite source size incident upon a grating, Figure III-2, the source size is projected onto the diffraction pattern, and this source size, Δh, becomes the minimum resolvable feature. For small diffraction angles, such that $\sin \theta_d \approx \tan \theta_d \approx \theta$, the minimum system resolution then becomes:

$$\Delta\lambda_{min} \approx \frac{p\Delta h}{L} \qquad (3\text{-}1)$$

where L is the distance from the grating to the recording plane.

To calculate the effects of finite source collimation upon system resolution, consider a source with some collimation angle, θ_c, incident upon a grating, Figure III-3. The angle of the first order diffracted beam would normally be:

$$\theta_d = \mathrm{Sin}^{-1} (\lambda/p) \approx \lambda/p \qquad (3\text{-}2)$$

With a finite collimation angle, the first order beam diverges to diffract in a wedge defined by the angles: $(\theta_d - 1/2\ \theta_c) \leq \theta \leq (\theta_d + 1/2\ \theta_c)$.

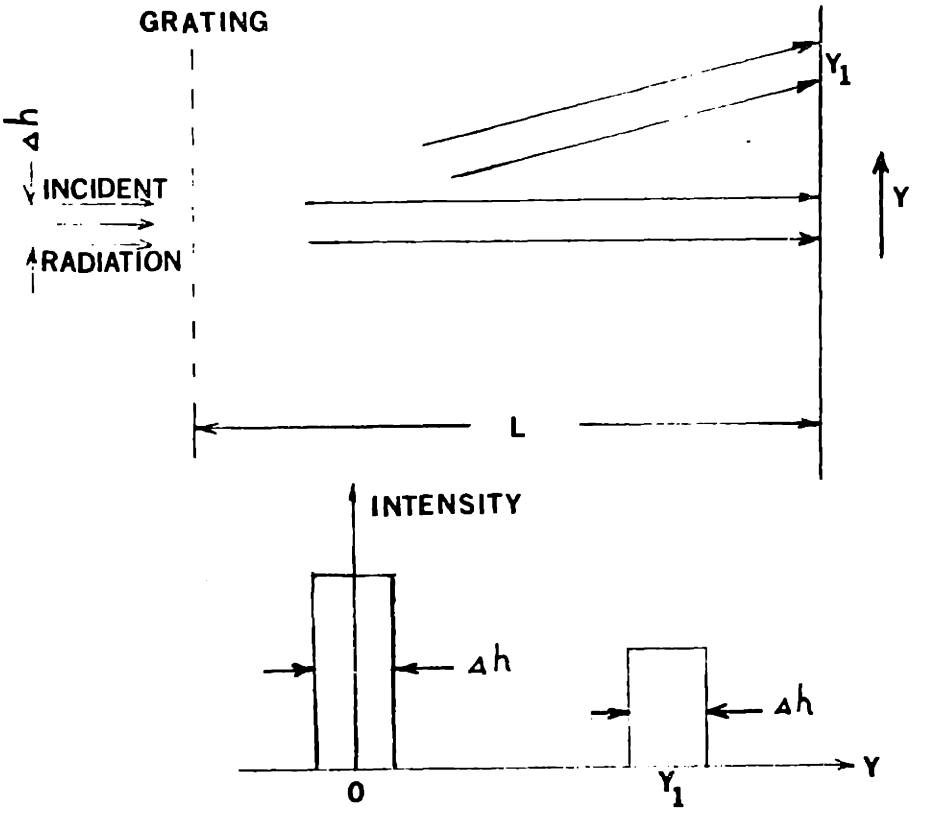

Figure III-2 An illustration of the effects of finite source size on the far field diffraction pattern. Incident monochromatic radiation with source size, Δh, is incident upon the grating. The size of the source is seen in the diffraction pattern, and has a width, Δh.

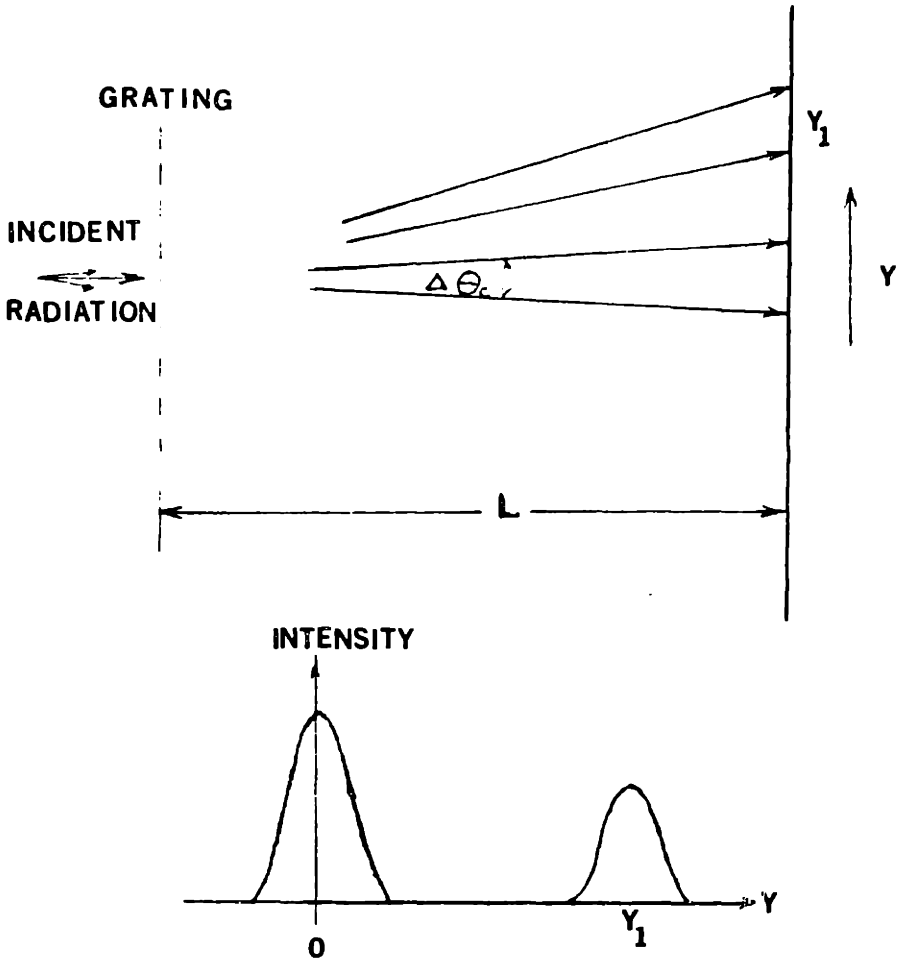

Figure III-3 An illustration of the effects of finite source collimation on the far field diffraction pattern. An infinitesimally narrow (in spatial extent) monochromatic source with finite collimation is incident upon the grating. The broadening in the far field diffraction pattern due to the finite source collimation is illustrated.

Again, for small angles such that Sin $\theta \backsim$ Tan $\theta \backsim \theta$, the spread, Δy, for a single narrow bandwidth source is:

$$\Delta y = L\ \theta_c \tag{3-3}$$

and the resolution, $\Delta\lambda_{min}$, is limited to be:

$$\Delta\lambda_{min} \backsim p\ \theta_c \tag{3-4}$$

As an example, to obtain a minimum resolution, $\Delta\lambda$, of 0.01 nm with a 300 nm period grating used in first order, and with a grating to film plane distance of 10 meters, both a source size of less than 300 μm and a source collimation of $< 3\times10^{-5}$ radians are required.

III-C EXPERIMENT FOR GRATING CHARACTERIZATION

In collaboration with N.M. Ceglio and R.H. Price of the Lawrence Livermore National Laboratory, the gratings were coupled to a 22x Wolter type[58] grazing incidence microscope with approximately 1 μm resolution,[53] to produce a high resolution imaging spectrometer, Figure III-4. To obtain discrete, narrow band x-ray lines, a Henke-type x-ray tube[54] with a tungsten anode, was used at 10 kV. The anode emitted the characteristic tungsten M_α, M_β, and M_γ lines (λ = 0.698, 0.676 and 0.609 nm, respectively), superimposed the broad-band continuum. One of several 4 μm thick gold masks with an array of apertures ranging in size from 2x2 μm to 20x50 μm was placed at the object plane of the microscope. The x-rays passing through the mask were then collected by the first surface of the microscope, the hyperboloid, and were reflected by total external reflection (angle of incidence $\lesssim$ 1°). The x-rays were then directed towards the second surface, the ellipsoid, in such a way that they appeared to originate from one focal point of the ellipsoid. The x-rays were redirected by

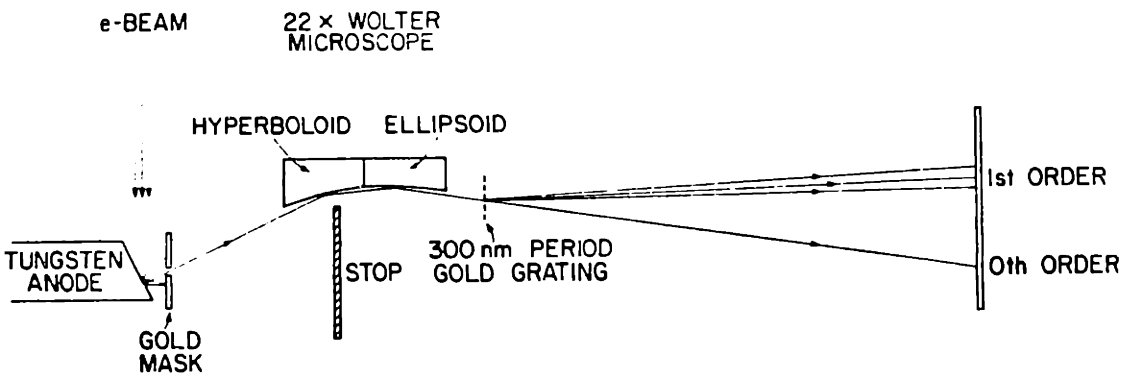

Figure III-4 High resolution imaging spectrometer. The x-rays from the tungsten anode pass through aperatures in the gold mask, and are redirected by the surfaces of the Wolter microscope. The x-rays are then incident upon a grating and are diffracted. The far field diffraction pattern is recorded on film.

the ellipsoid surface by total external reflection, and focused toward the second focus of the ellipsoid, which is the image plane of the microscope. An exit aperture, placed between the ellipsoid and the image plane, was used to block most of the x-rays. The x-ray beam exiting the aperture was approximately 300 μm x 7 mm in size, and was incident upon a thick gold transmission grating, Figure III-4.

III-D EXPERIMENTAL RESULTS OF GRATING CHARACTERIZATION

The Wolter 22x grazing incidence microscope used in this work has a demonstrated spatial resolution of approximately 1 μm when the full annular aperture of the microscope is utilized. In the imaging spectrometer work, the gratings subtended only ∿ 2.5% of the annular aperture (diameter of grating ∿ 7 mm) and the remainder of the aperture was obstructed. The gratings used in this work had a spatial period of 300 nm, gold thickness of 0.6 μm, and were supported on a 0.5 μm thick polyimide membrane, which is transparent to the tungsten M lines (approximately 0.15 dB attenuation). The 0.6 μm thick gold lines exhibited approximately 8 dB attenuation to the tungsten M lines.[55]

For the highest resolution experiments, a test pattern mask, consisting of an array of apertures ranging in size from 6x9 μm to about 2x2 μm in a 4 μm thick gold foil served as the object in the imaging spectrometer. The spectrally dispersed images of the test pattern mask, in addition to the zeroth order image, were recorded on a variety of x-ray films (Kodak type M, AA, KK, No Screen). Shown in Figure III-5 is a typical result obtained from this experiment, where the tungsten M lines are clearly resolved in the first order diffraction pattern. The dispersion, $dy/d\lambda$, at

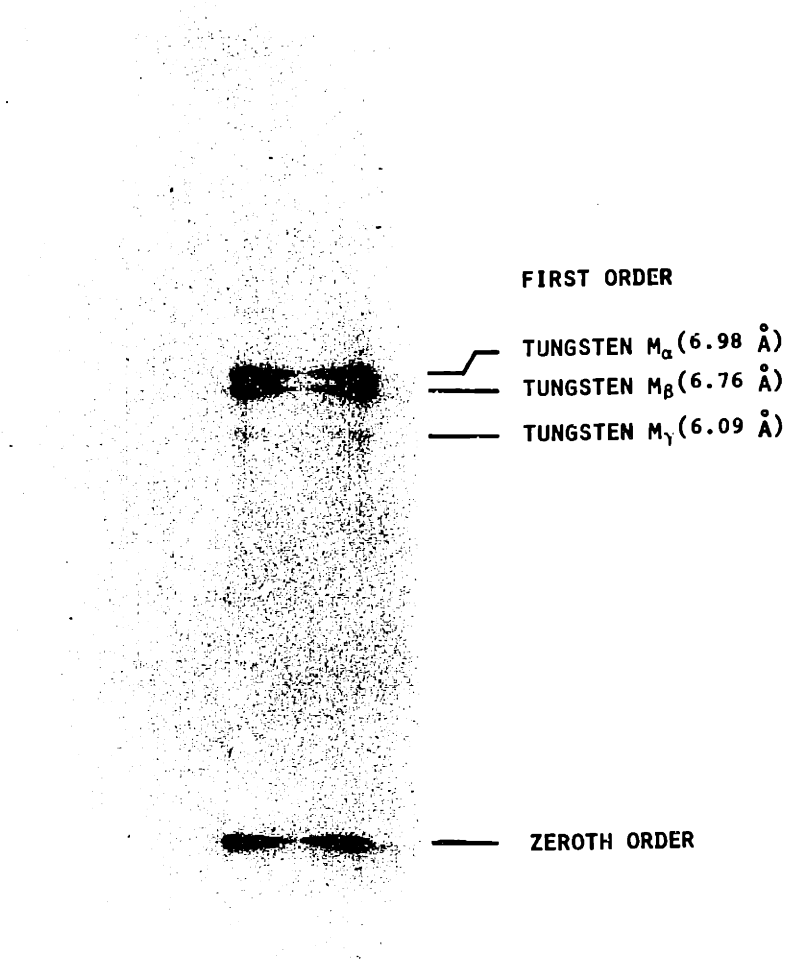

Figure III-5 Spectrogram obtained with the high resolution imaging spectrometer of Figure III-4. The tungsten M_α, M_β and M_γ lines are clearly resolved.

the film plane, measured between the M_α and M_β lines, is 19.6 mm/nm. The calculated dispersion, obtained from diffraction theory is:

$$\frac{dy}{d\lambda} \backsim \frac{L}{p} \tag{3-5}$$

where L is the distance from the grating to the film plane. For this experiment, L was 5.92 meters, and the calculated dispersion agrees with the measured dispersion to within 1/2%.

The minimum feature size in the image plane (image of the smallest aperture, nominally 2x2 μm) had a full width at half maximum of 66 μm in the zeroth and M_α first orders as determined by densitometry traces. The spectral resolution, $\Delta\lambda$, of the imaging spectrometer, is therefore:

$$\Delta\lambda \leq (66\ \mu m) \cdot (dy/d\lambda)^{-1} = 3.4 \times 10^{-3}\ nm \tag{3-6}$$

For $\Delta\lambda = 3.4 \times 10^{-3}$ nm, the resolving power, $\lambda/\Delta\lambda$, of the grating at λ = 0.698 is 205. A somewhat lower value (192) was obtained for the M_β line. It is important to note that these measured numbers for the resolution and resolving power are worst case estimates for the gratings. The resolution measured in this experiment is source size limited, and not limited by the distortions in the grating. The distortions in the grating are estimated to be $< 10^{-4}$ over the area illuminated by the x-rays (7 x 0.3 mm, parallel and perpendicular to the grating lines, respectively), taking into account membrane distortion ($< 10^{-4}$) and a worst-case estimate of the distortion produced by the use of spherical wavefronts in the holographic lithography ($< 10^{-4}$ at the corners of the grating area), as discussed in Appendix E (actual distortion may be much smaller than 10^{-4}). Since $\backsim 10^3$ grating lines were illuminated by the x-ray source, a grating resolving power of

10^3 can be expected and the lower value of 200 for the imaging spectrometers' resolving power is probably due to the finite source size.

The diffraction efficiency of the transmission diffraction grating is another important measurement in the characterization of the grating. For a fully opaque grating with lines and spaces of equal widths, 25% of the radiation incident upon the grating will appear in the zeroth diffracted order, I_0, and 10% will appear in each of the first two diffracted orders, I_1[34,52]. It is then possible to define the transmission diffraction efficiency (Footnote 1) as the ratio of the intensity in one of the first orders versus the intensity in the zeroth order:[59]

$$\eta = I_1/I_0 \qquad (3\text{-}7)$$

For such a fully opaque grating, the diffraction efficiency would be 40%. For a grating with partially transmitting lines, this ratio can be either higher or lower, depending upon the phase differences between the x-rays emerging from the partially opaque lines relative to the transmissive spaces of the grating. If the partially transmitted radiation experiences an appropriate phase shift relative to the unattenuated radiation, the diffraction efficiency will be increased. The diffraction efficiency can also be affected by the line-to-period ratio of the diffraction grating. The spectrogram of Figure III-5 was measured by a microdensitometer to determine the relative intensities of the first and zeroth order diffracted beams. The diffraction efficiency, defined as the sum of the intensities of the three tungsten M lines in one first order diffracted beam, relative

---

Footnote 1: A more traditional definition[34,52] for the efficiency of a transmission diffraction grating is the ratio of the energy in one first order diffracted beam to the incident energy. For the grating discussed above, this is 10%. However, to accurately determine this value requires the measurement of the energy incident upon the grating, which is often impractical. Therefore, the transmission diffraction efficiency as discussed above, is often used.

to the total intensity of the zeroth order beam, was measured to be 100% ±10%. This high efficiency can be accounted for by the partial transmission and subsequent phase shift through the grating lines, and the unequal widths of the lines relative to the spaces. The gold attenuated only approximately 8 dB (transmitted 16%) of the incident radiation, with a phase shift, and the gold line-to-space ratio of the 300 nm period grating used, was approximately 1.6:1. Recent calculations by M. Shattenburg[60] confirm the high diffraction efficiency observed in this experiment. Transmission diffraction efficiencies of 16% were recently reported for a 420 nm period transmission grating.[59]

III-E APPLICATIONS OF THICK GOLD TRANSMISSION DIFFRACTION GRATINGS TO SOFT X-RAY DIAGNOSTICS

Once the characteristics of the thick gold transmission diffraction gratings are measured, it is possible to use the gratings as spectroscopic diagnostic tools. The versatility and ease of implementation of the transmission gratings allow the gratings to be coupled to a variety of existing diagnostic instruments to broaden their capabilities. For example, the coupling of a grating to a Wolter type microscope, as already mentioned, obtained both spatial and spectral information simultaneously. The same can be done to an x-ray telescope to obtain spectral and spatial information of stellar objects. Gratings fabricated in this thesis research have also been coupled to an x-ray streak camera with temporal resolution of $\sim$ 20 psec, to obtain both temporal and spectral information of a laser produced plasma,[61,62] Figure III-6. In this experiment, the two arms of the Argus Laser System at the Lawrence Livermore National Laboratory heated a

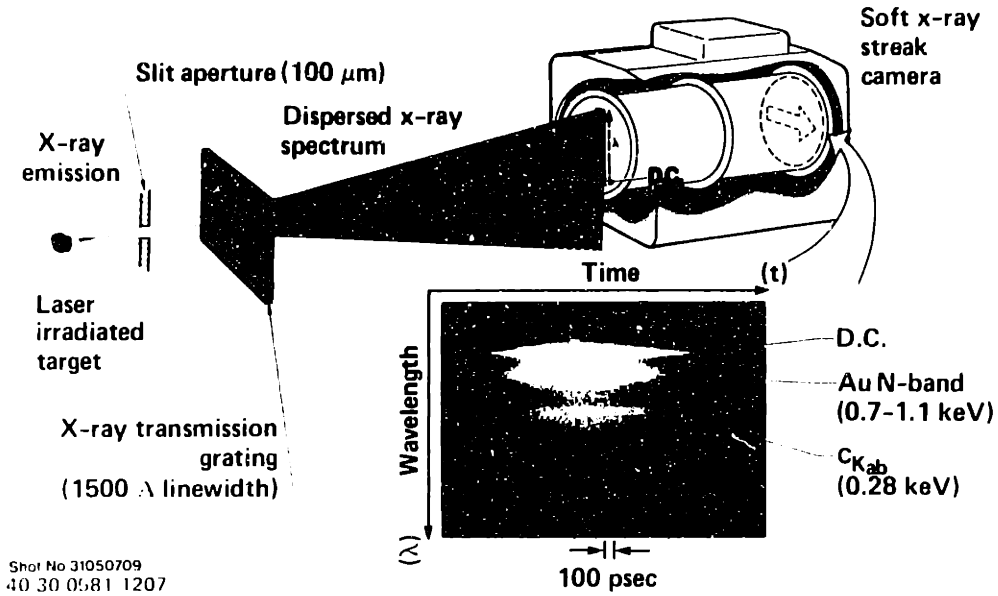

Figure III-6 By coupling a grating to a streak camera, both x-ray spectral and temporal information can be obtained, as illustrated above for the x-rays produced by a laser irradiated gold target. A free standing x-ray transmission grating is coupled to a soft x-ray streak camera to provide time resolved ($\sim$ 20 psec) continuous x-ray spectra over a broad spectral range (0.1 to 1.5 keV).

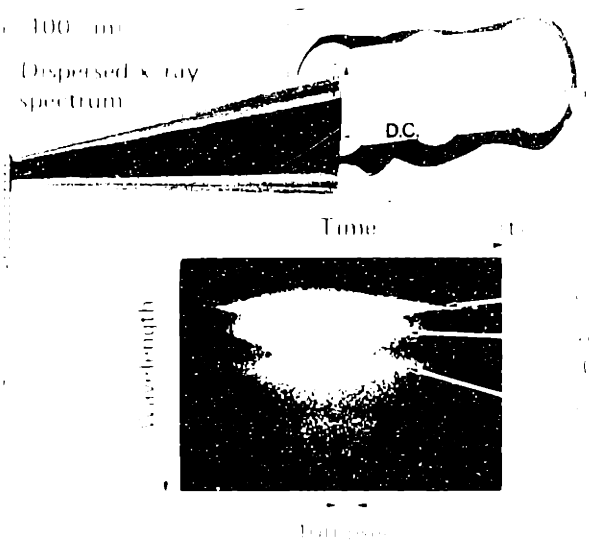
Dispersed x-ray
spectrum
D.C.
Time

gold disc which then emitted soft x-rays. The x-rays were then temporally and spectrally dispersed by the streak camera, equipped with a transmission diffraction grating.

The gratings have also been used in a strictly spectroscopic sense, to simply diffract soft x-rays, without any other instrumentation.[61,62] The gratings diffracted the x-rays from both gold and titanium disks that were again heated by the Lawrence Livermore National Laboratory's Argus Laser System. To limit the source size and source collimation, a slit was placed in front of the grating, and the soft x-ray spectra of both the gold and titanium disks were recorded on x-ray sensitive film, Figure III-7.

Plans are currently underway to couple a transmission diffraction grating with a Zone Plate Coded Imaging (ZPCI) aperture, to get both spectral and spatial resolution of soft x-ray radiation.[35] ZPCI is the spatial reconstruction of a source by optically decoding the shadow cast by the source through a zone plate onto a recording medium,[35,63] Figure III-8, where the source distribution is represented by three distinct emission points. Each source casts a shadow of the zone plate (coded image) onto the recording medium, and each zone plate shadow is uniquely characterized by the size and position of its source. The coded image is then decoded by illuminating it with an optical laser. Each recorded zone plate focuses the incident laser light to a diffraction limited spot, and the image of the original source is point by point reconstructed. By placing a thick gold transmission grating with appropriate periodicity between the original zone plate coded aperture and the recording medium, it should be possible to obtain both spectral and spatial information simultaneously, Figure III-9.

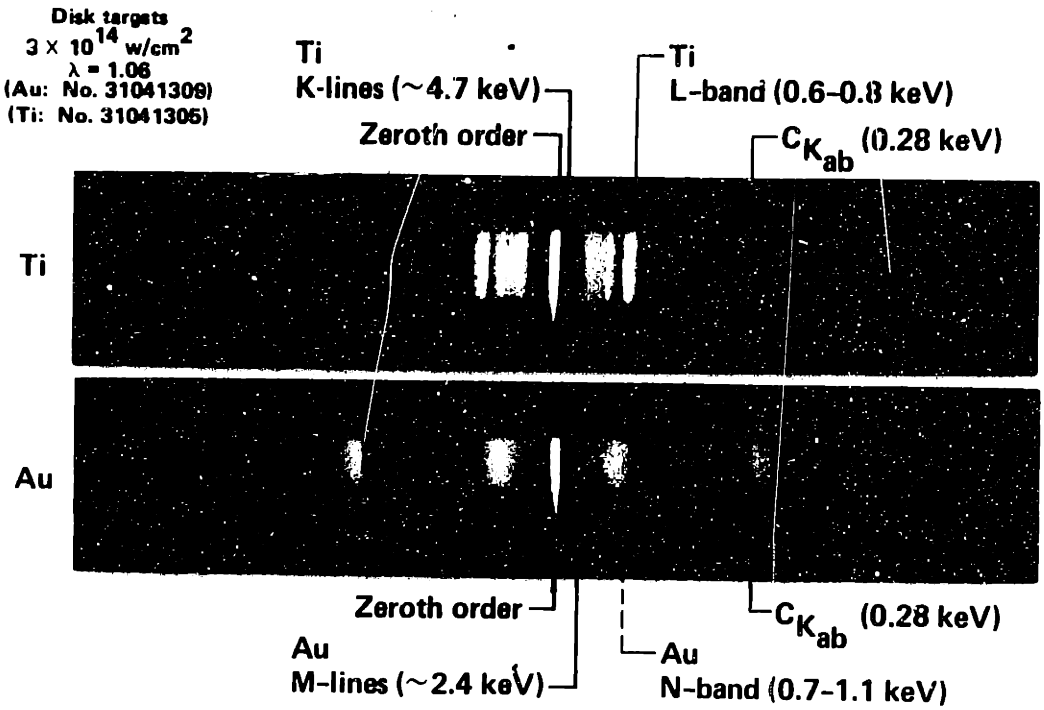

Figure III-7 Spectrogram of the x-ray emission from gold and titanium pellets under laser irradiation.

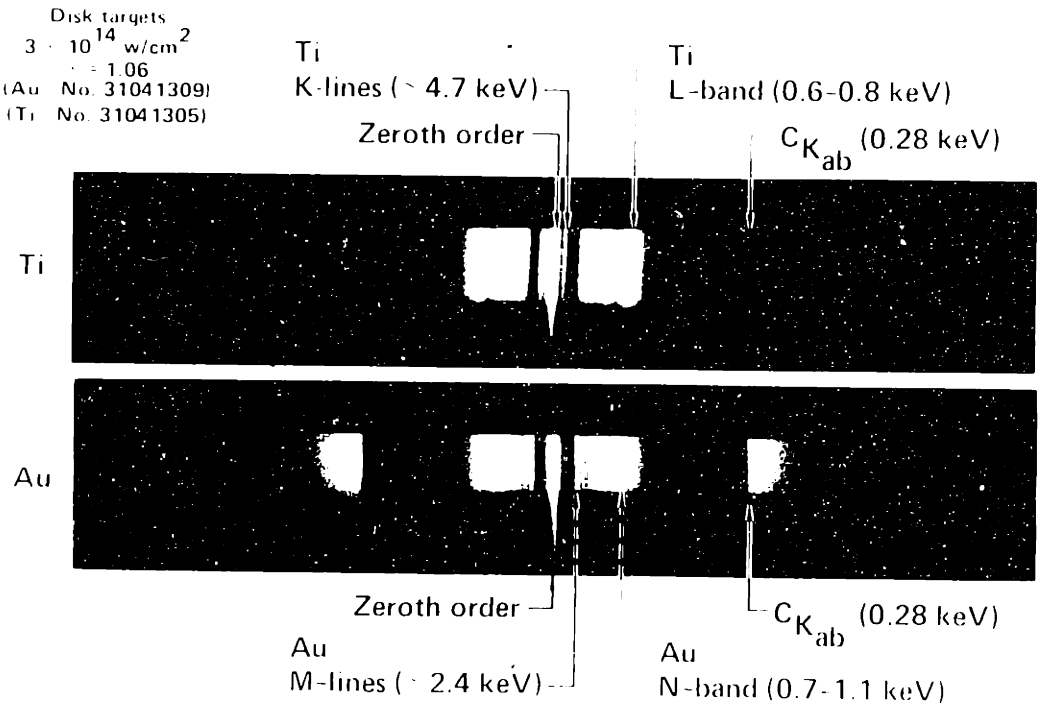

Figure III-[illegible] Spectrograms of the x-ray emission from gold and titanium pellets under laser irradiation.

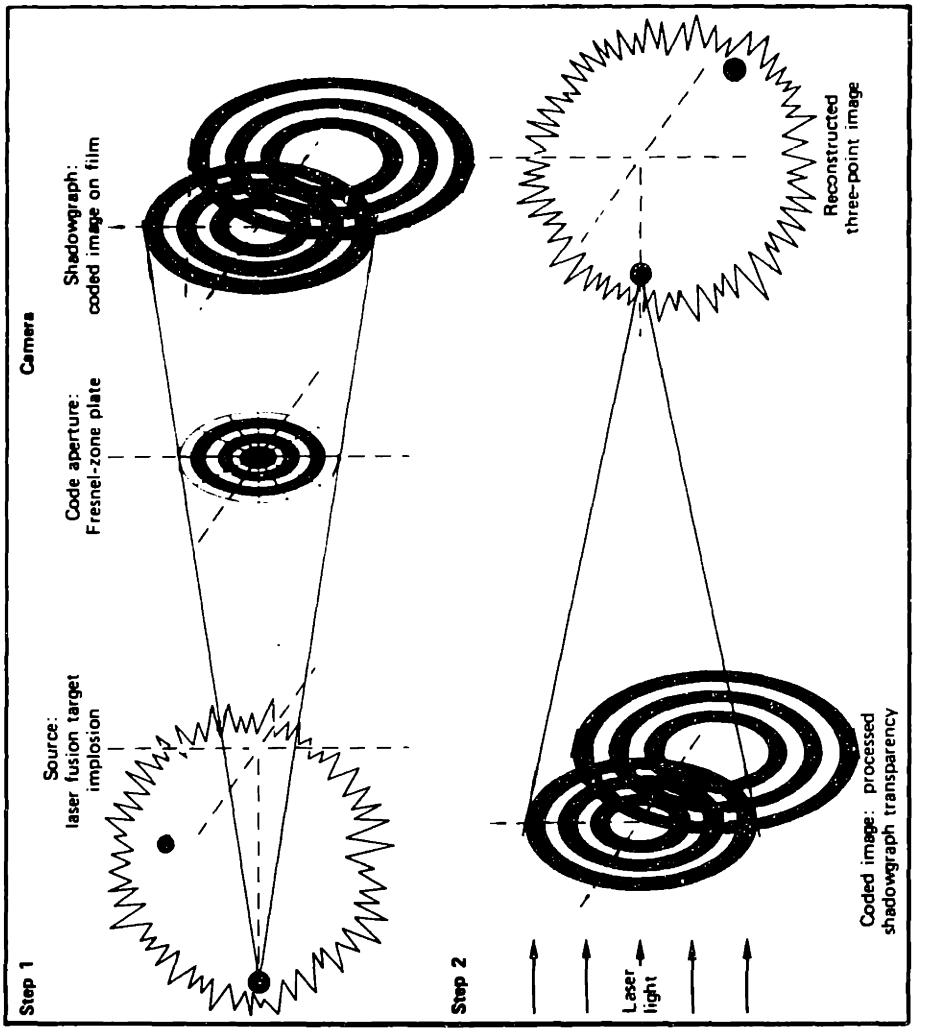

Figure III-8 Illustration of Zone Plate Coded Imaging (ZPCI). Step 1: A zone plate aperature views the radiation source, and casts a shadow onto a recording film. Step 2: The processed shadowgraph transparency is "playedback" with a visible laser light.

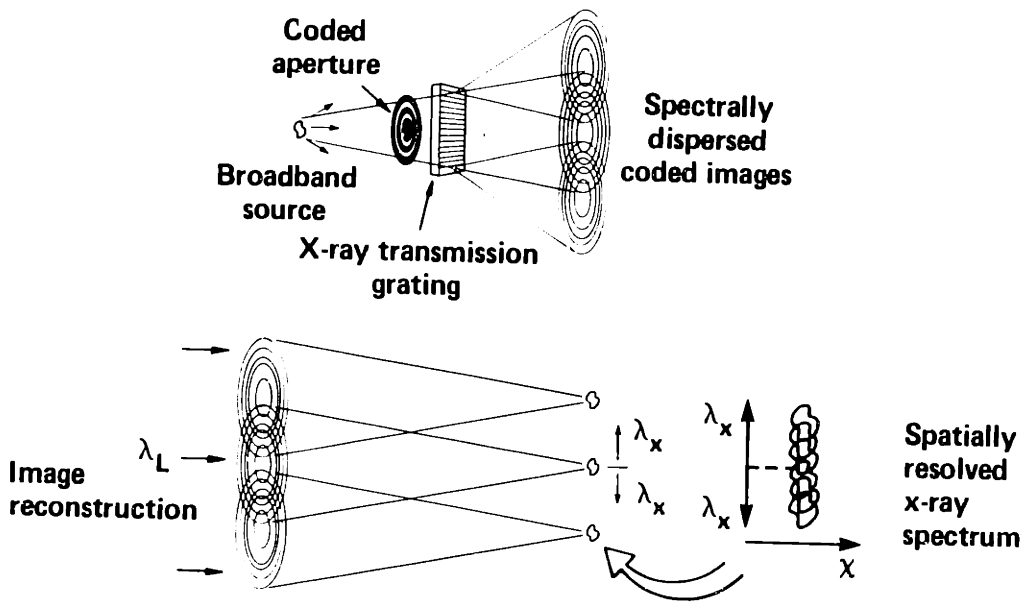

Figure III-9 By coupling a zone plate coded image aperture to a grating, both spatial and spectral resolution can be obtained simultaneously. A coded aperture (zone plate) serves as the entrance slit of a transmission grating spectrometer. The spectrally dispersed coded images can be reconstructed into a spatially resolved x-ray spectrum.

CHAPTER IV

THEORY OF SPATIAL PERIOD DIVISION

IV-A INTRODUCTION

The minimum spatial period that can be exposed with conventional holographic lithography is limited to one-half of the wavelength of the laser. By applying holographic lithography in a high index medium, gratings with spatial periods as fine as 110 nm have been produced,[37] but this technique cannot be extended to much finer grating periods. By upconverting a Nd:YAG laser, Bjorklund[64] produced radiation with wavelengths as short as 118.2 nm, and produced a grating with a spatial period of 83.5 nm in a holographic lithography arrangement. Clearly, an alternate procedure for producing sub-100 nm period gratings is desirable.

The technique of spatial period division allows one to produce, from a grating with period p, a new grating with period p/m, where "m" is an integer. This technique utilizes the near field diffraction pattern of an existing grating. By appropriate choice of a master ("parent") grating and an illumination source, it may be possible to produce gratings with spatial periods limited by the resolution of lithography. The phenomenon of spatial period division has been observed by other researchers in the past.[28,29,65-68] What is new in this dissertation is the use of this technique, coupled with x-ray lithography, to produce sub-100 nm period gratings, and to theoretically analyze the near field diffraction pattern of a parent grating in order to predict the occurrence and optimization of the spatial period division image.

IV-B ANALYSIS OF THE NEAR FIELD DIFFRACTION PATTERN

The near field diffraction pattern of a grating will be analyzed by the method known as the "angular spectrum of plane waves".[69] Goodman[69] has described this simple, intuitively appealing method of calculating the diffraction pattern of objects within the framework of scalar diffraction theory. The method is especially suitable for the description of diffraction from gratings. It involves writing the complex electric field (in scalar theory, polarization is ignored) across the plane of an aperture or a grating (the plane $z = 0$) as a Fourier integral (or a Fourier series for the case of a grating), with the various spatial Fourier components being identified as plane waves traveling in appropriate directions. The field amplitude at any point "downstream" of the grating ($z > 0$) is calculated by adding the contributions of these plane waves, taking into account the phase changes that they undergo during propagation. I will use this approach to analyze the near field diffraction pattern of a grating. It is well known that scalar diffraction theory (and hence, the angular spectrum of plane waves analysis, which assumes scalar diffraction theory) is valid in the domain where the diffracting apertures are large compared with the wavelength and at sufficient distances from the aperture so that evanescent fields are negligible. In practice, the agreement between scalar theory and rigorous diffraction theory is surprisingly good. With one exception (section IV-E) the patterns that will be analyzed in this dissertation fall within the domain of validity of scalar diffraction theory. The boundary conditions assumed are that the electric field across the surface of the grating can be discontinuous, and is a square-wave like function. The local electric field at a grating "space" is the same as what the electric

field would be in the absence of the grating, and the electric field at a grating line is simply attenuated and phase shifted by the grating line.

In the following analysis, I will consider a grating of period p, consisting of "lines" (regions of attenuation and phase shift) and "spaces" (no attenuation or phase shift). The width of the spaces is equal to $2p/\beta$, and the electric field at the grating lines has amplitude b and phase shift φ relative to the spaces, Figure IV-1. Goodman has given an integral expression for the complex electric field, E(x,y,z) at a distance z from the plane (x,y,0), which is the location of the aperture, or as in our case, the grating. If we establish a coordinate system so that the x axis is perpendicular to the grating lines, the z axis is perpendicular to the plane of the grating, and the radiation propagates in the z direction, as in Figure IV-1, the integral expression for a component of electric field in front of a grating of infinite length in the y and x directions is:

$$E(x,z) = \int_{-\infty}^{\infty} A_o(k_x) \exp\{jk\sqrt{1-\left(\frac{k_x}{k}\right)^2}\cdot z\}\cdot\exp\{j(k_x x)\}\,dk_x \qquad (4\text{-}1)$$

where: $$A_o(k_x) = \int_{-\infty}^{\infty} E(x,o)\exp\{-j(k_x x)\}dx \qquad (4\text{-}2)$$

and:

$|\bar{k}| = k = 2\pi/\lambda$

$k_x = \bar{k}\cdot\hat{x}$

$k_z = \bar{k}\cdot\hat{z}$

$K = 2\pi/p$

$\hat{z}$ = a unit vector normal to the plane of the grating

$\hat{x}$ = a unit vector normal to the grating lines and in the plane of the grating

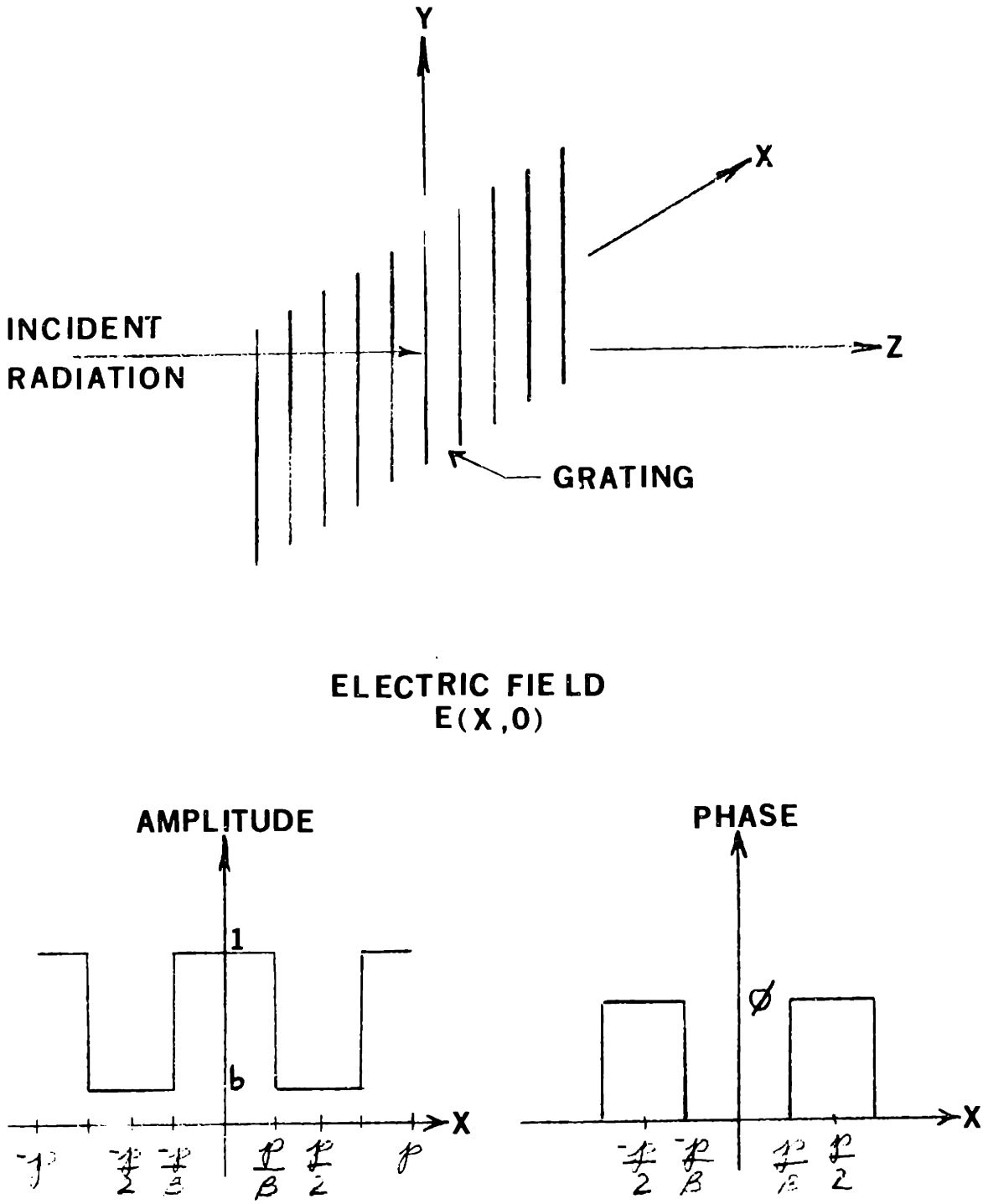

Figure IV-1 Radiation incident upon a grating of infinite extent. The radiation propagates along the Z axis (perpendicular to the plane of the grating). The electric field, E(X,0), at the plane of the grating, Z = 0, is represented by the amplitude and phase diagrams.

For the case of a grating, it is more convenient to write E(x,z) as the Fourier series:

$$E(x,z) = \sum_{n=-\infty}^{\infty} B_n \exp(j\, k_x\, x)\, \exp(j\, k_z\, z) \tag{4-3}$$

where k_x can take on only discrete values:

$$k_x = k_x(n) = n \cdot 2\pi/p = n \cdot K$$

Since $k^2 = k_x^2 + k_z^2$, k_z also takes on only discrete values:

$$k_z = k_z(n) = k\sqrt{1-(k_x/k)^2} = k\sqrt{1-(\frac{n\lambda}{p})^2}$$

If k_z is real we have, from equation (4-3), a propagating wave. Thus we impose the condition :

$$(n\lambda/p)^2 < 1 \tag{4-4}$$

$$\text{or} \quad p/\lambda > |n| \tag{4-5}$$

As a result, the index "n" can take on only a finite range of values, from $-n_o$ to $+n_o$, where n_o is the largest integer $\leq p/\lambda$.

When the grating is illuminated by a plane wave the complex electric field in the plane (x,y,0) is given by E(x,0), as defined in Figure IV-1. The values for B_n in equation 4-3 are:

$$B_n = \frac{1}{p}\int_{-p/2}^{p/2} E(x,0)\, \exp\{-jnKx\}\, dx \tag{4-6}$$

which yields:

$$B_o = \frac{1}{p}\left[\frac{2p}{\beta} + be^{j\phi}(p - 2p/\beta)\right] \tag{4-7}$$

$$B_n = \frac{\mathrm{Sin}(2n\pi/\beta)}{n\pi}\,[1 - be^{j\phi}] \tag{4-8}$$

With these values for B_n, the complex electric field, $E(x,z)$ can be calculated by using equation (4-3).

Because $E(x,0)$ is an even function, the expression to calculate $E(x,z)$ can be simplified to:

$$E(x,z) = B_o \exp\{jkz\} + 2 \sum_{n=1}^{n_o} B_n \mathrm{Cos}(nKx) \exp\{jk_z(n)\cdot z\} \tag{4-9}$$

and the resulting intensity pattern is:

$$I(x,z) = |B_o|^2 + 4 \sum_{n=1}^{n_o} B_o B_n \mathrm{Cos}(nK\,x) \mathrm{Cos}((k-k_z(n))z) + \tag{4-10}$$

$$4 \sum_{n=1}^{n_o} \sum_{q=1}^{n_o} B_n B_q \mathrm{Cos}(nK\,x) \mathrm{Cos}(qK\,x) \mathrm{Cos}((k_z(n)-k_z(q))z)$$

It is clear that, in the series, sinusoidal intensity patterns with spatial frequencies higher than the fundamental (original) grating exist. For example, the first summation in equation 4-10 can be expanded as:

$$\sum_{n=1}^{n_o} B_o B_n \mathrm{Cos}(nKx) \mathrm{Cos}((k-k_z(n))z) = \tag{4-11}$$

$$B_o B_1 \mathrm{Cos}(Kx) \mathrm{Cos}((k-k_z(1))z) +$$

$$B_o B_2 \mathrm{Cos}(2Kx) \mathrm{Cos}((k-k_z(2)z) + \ldots$$

where the first term on the right hand side is sinusoidal in the fundamental grating period, p, the second term is sinusoidal with spatial period equal to one half the original grating period, etc. Since each term in the series has a factor of $\mathrm{Cos}((k-k_z(n))z)$, it is clear that each term will pass through maxima and minima as z is increased. Spatial period division (i.e., a pattern of period p/m) occurs when the term corresponding to an

intensity pattern with spatial period p/m (and others that add constructively) is a maximum, while the terms that add destructively, are minimum. This occurs at the proper location, z, and at the proper line-to-period ratio of the original grating (i.e., appropriate value for β). In this chapter, I will analyze the conditions under which spatial period division occurs. First, I will present a simplified discussion of the optimum conditions for "doubling" (m = 2) with a highly opaque grating. I will then consider "doubling" with a phase grating and "doubling" with a grating such that only the zeroth and first order diffracted beams are present (i.e., $p > \lambda > p/2$). Then I will analyze the near field diffraction pattern of a grating to derive a general understanding of the conditions necessary for spatial period division at any value of "m". The effects of phase shift and attenuation through the grating lines on the quality of the spatial period division will be considered in addition to a displacement from the optimum distance, z, for spatial period division.

IV-C "DOUBLING" WITH A HIGHLY OPAQUE PARENT GRATING

If the opaque regions (the "lines") of the grating are highly opaque (zero transmission), then the electric field at the plane of the grating, z = 0, can be graphically represented as in Figure IV-2, where the transmissive regions (the spaces) of the grating have a width equal to $2p/\beta$. Under these conditions, from equations 4-7 and 4-8, the Fourier series coefficients are:

$$B_0 = 2/\beta$$

$$B_n = \frac{1}{n\pi} \operatorname{Sin} \left(\frac{2n\pi}{\beta}\right) \qquad (4\text{-}12)$$

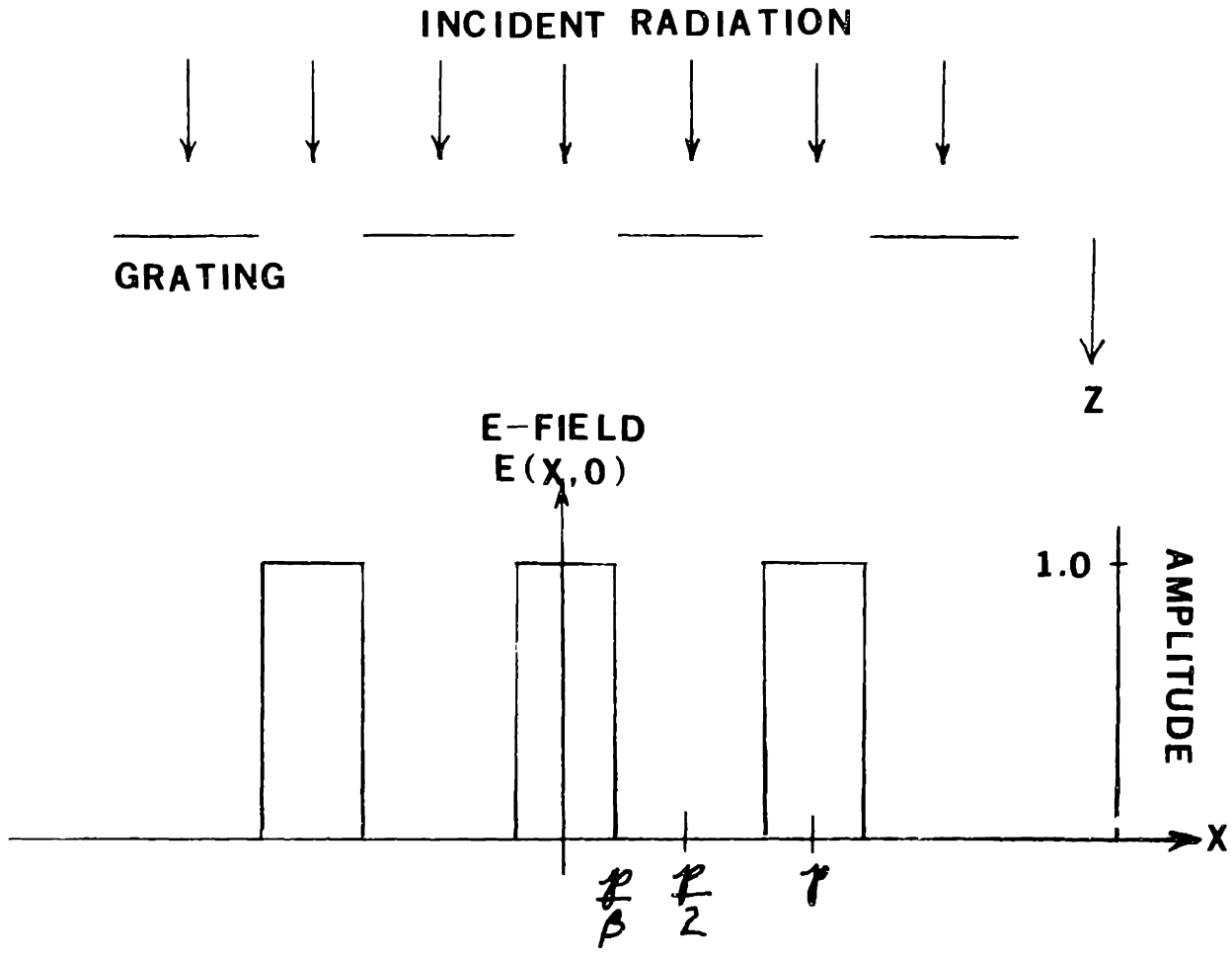

Figure IV-2 The electric field at the plane of the grating, Z = 0, for a highly opaque grating (b = 0).

Recall that the intensity pattern is given by:

$$I(x,z) = |B_o|^2 + 4 \sum_{n=1}^{n_o} B_o B_n \cos(nKx) \cos((k-k_z(n))z) + \quad (4\text{-}10)$$

$$4 \sum_{n=1}^{n_o} \sum_{q=1}^{n_o} B_n B_q \cos(nKx) \cos(qKx) \cos((k_z(n)-k_z(q))z)$$

For $\lambda << p$ and for n small, $(k-k_z(n))$ can be simplified to:

$$(k-k_z(n)) \approx [k - \frac{2\pi}{\lambda} (1 - \frac{n^2\lambda^2}{2p^2})] = \frac{\pi n^2 \lambda}{p^2} \quad (4\text{-}13)$$

This approximation is increasingly less valid for large n, but since the Fourier series coefficients, B_n, become increasingly smaller for large n, the error produced in calculating the intensity pattern with this approximation is small. Similarly, $(k_z(n) - k_z(q))$ can be simplified to:

$$(k_z(n)-k_z(q)) \approx \frac{\pi\lambda}{p^2} (q^2-n^2) \quad (4\text{-}14)$$

The intensity pattern can be re-written as:

$$I(x,z) \approx |B_o|^2 + 4 \sum_{n=1}^{n_o} B_o B_n \cos(nKx) \cos(\frac{\pi n^2 \lambda}{p^2} z) + \quad (4\text{-}15)$$

$$4 \sum_{n=1}^{n_o} \sum_{q=1}^{n_o} B_n B_q \cos(nKx) \cos(qKx) \cos(\frac{\pi\lambda}{p^2} (q^2-n^2)z)$$

Since this approximation is valid only for small values of n and q (i.e. $(\frac{n\lambda}{p})^2 < 0.1$), only those terms of equation (4-15) will be analyzed. This approximation is used to give insight to the problem of spatial period division. Later, a computer is used to calculate the near field diffraction pattern without this approximation, using equation (4-10).

Returning to equation 4-15, "doubling" occurs when the n=1 term in the first summation in equation (4-15) is at a minimum, and the n=2 term is at a maximum. The n=1 term is minimum when:

$$\text{Cos}\left(\frac{\pi\lambda}{p^2}\, z\right) = 0$$

or

$$z = \frac{t_1}{2}\,\frac{p^2}{\lambda} \tag{4-16}$$

where t_1 is any odd integer. The n=2 term is maximum when:

$$\text{Cos}\left(\frac{4\pi\lambda z}{p^2}\right) = 1$$

or

$$z = \frac{t_2}{2}\,\frac{p^2}{\lambda} \tag{4-17}$$

where t_2 is any integer. Therefore, "doubling" occurs when these two conditions are satisfied:

$$z = \frac{p^2}{2\lambda} \cdot t_1 \tag{4-18}$$

The location corresponding to $t_1 = 1$ is now analyzed in detail. At this location, all terms with odd indices in the first summation of equation (4-15) are zero, and only even indexed terms are non-zero. A maximum intensity in the n=2 term results when the value of B_2 is a maximum. This happens with linewidth-to-period ratio in the parent grating equal to 3:4, which corresponds to a value for $\beta = 8$ (see equation (4-12)). Under these conditions, the Fourier series coefficients with indices which are multiples of four are zero, i.e. $B_4 = B_8 = B_{12} = \ldots = 0$. The only non-zero terms in the entire first summation of equation (4-15) at $z = p^2/2\lambda$ and for $\beta = 8$ are the terms with n = 2, 6, 10 ...

At this point, it is more instructive to return to the expression for the electric field at the "doubling" location. Equation (4-9) can be written as:

$$E(x,z) = \exp\{jkz\}\left[B_o + 2\sum_{n=1}^{n_o} B_n \,\text{Cos}(nKx)\, \exp\{j(k_z(n)-k)z\}\right]$$

disregarding the phase factor exp(jkz), and using equation 4-13, the electric field becomes:

$$E(x,z) = B_o + 2 \sum_{n=1}^{n_o} B_n \cos(nKx) \exp(j\pi n^2 \lambda z/p^2)$$

Note that for n even and $z = p^2/2\lambda$, the phase factor, $\exp(j\pi n^2 \lambda z/p^2) = 1$. For the same z and n odd, the phase factor equals j. Therefore the electric field can be re-written as the sum of two terms:

$$E(x, \frac{p^2}{2\lambda}) = E_1(x) + jE_2(x)$$

where

$$E_1(x) = B_o + 2 \sum_{n=1}^{n_o/2} B_{(2n)} \cos(2nKx) \qquad (4\text{-}19)$$

and

$$E_2(x) = 2 \sum_{n=1}^{n_o/2} B_{(2n-1)} \cos((2n-1)Kx) \qquad (4\text{-}20)$$

Note that the intensity $I(x, p^2/2\lambda)$ is simply:

$$I(x, p^2/2\lambda) = (E_1(x) + jE_2(x)) \cdot (E_1(x) - jE_2(x))$$
$$= (E_1(x))^2 + (E_2(x))^2 \qquad (4\text{-}21)$$

$E_1(x)$ and $E_2(x)$ are partial sums, up to $n_o/2$ of the functions $\varepsilon_1(x)$ and $\varepsilon_2(x)$ where:

$$\varepsilon_1(x) = B_o + 2 \sum_{n=1}^{\infty} B_{(2n)} \cos(2nKx)$$

and

$$\varepsilon_2(x) = 2 \sum_{n=1}^{\infty} B_{(2n-1)} \cos((2n-1)Kx)$$

The functions $E_1(x)$ and $E_2(x)$ approach $\varepsilon_1(x)$ and $\varepsilon_2(x)$ as $n_o \to \infty$. The functions $\varepsilon_1(x)$ and $\varepsilon_2(x)$ are plotted in Figure IV-3. Note that $\varepsilon_1(x)$ is a square wave function of period p/2, whereas $\varepsilon_2(x)$ is a square wave function of period p. However, $|\varepsilon_2(x)|^2$ has a period p/2. Thus, the intensity pattern obtained from the summation $|\varepsilon_1(x)|^2 + |\varepsilon_2(x)|^2$ has a period equal to p/2. Therefore, as $n_o \to \infty$, the near field diffraction intensity pattern, $I(x, p^2/2\lambda)$, has a period of p/2.

The summations in equation 4-10 were performed on a computer for the following parameters: p = 200 nm, $z = p^2/2\lambda$ = 4 μm, β = 8 and λ = 5 nm. These parameters were chosen to closely simulate the experiment described in Chapter 5. Figure IV-4 illustrates the image produced at the "doubling" distance, 4 μm, and has an intensity pattern with a spatial periodicity of 100 nm. The intensity pattern is adequate for resist exposure.

The analysis can be expanded (as is done in section IV-F) to yield a general relation for the location, z, of the m^{th} spatial period division, and its corresponding optimum value of β.

IV-D "DOUBLING" WITH A PHASE GRATING

Figure IV-5 illustrates a phase grating: transmission of an incident plane wave through the grating yields a field pattern at the grating (E(x,0)) with unity magnitude, but, at the lines of the grating, the phase is shifted by π radians relative to the phase at the spaces of the grating. The Fourier series coefficients for such a grating are:

$$B_o = 0 \tag{4-22}$$

$$B_n = \frac{2}{n\pi} \operatorname{Sin}\left(\frac{n\pi}{2}\right) \tag{4-23}$$

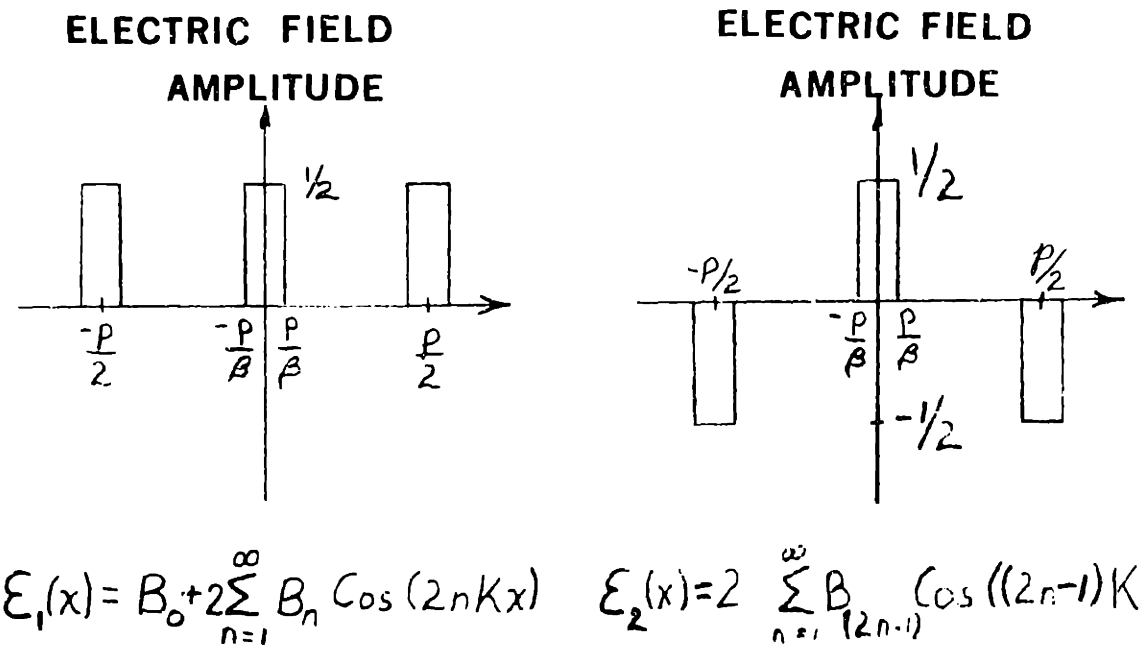

$$\mathcal{E}_1(x) = B_0 + 2\sum_{n=1}^{\infty} B_n \cos(2nKx) \qquad \mathcal{E}_2(x) = 2\sum_{n=1}^{\infty} B_{(2n-1)} \cos((2n-1)Kx)$$

SUPERPOSITION:

$$|\mathcal{E}_1(x)|^2 + |\mathcal{E}_2(x)|^2$$

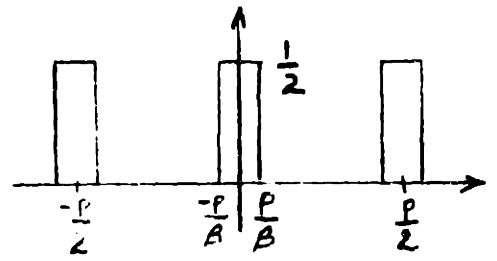

Figure IV-3 The near field diffraction pattern of a highly opaque grating at the "doubling" distance ($Z = p^2/2\lambda$) is the superposition of two electric fields, $(E_1(x) + iE_2(x))$ which, when squared, produces an intensity pattern of period p/2.

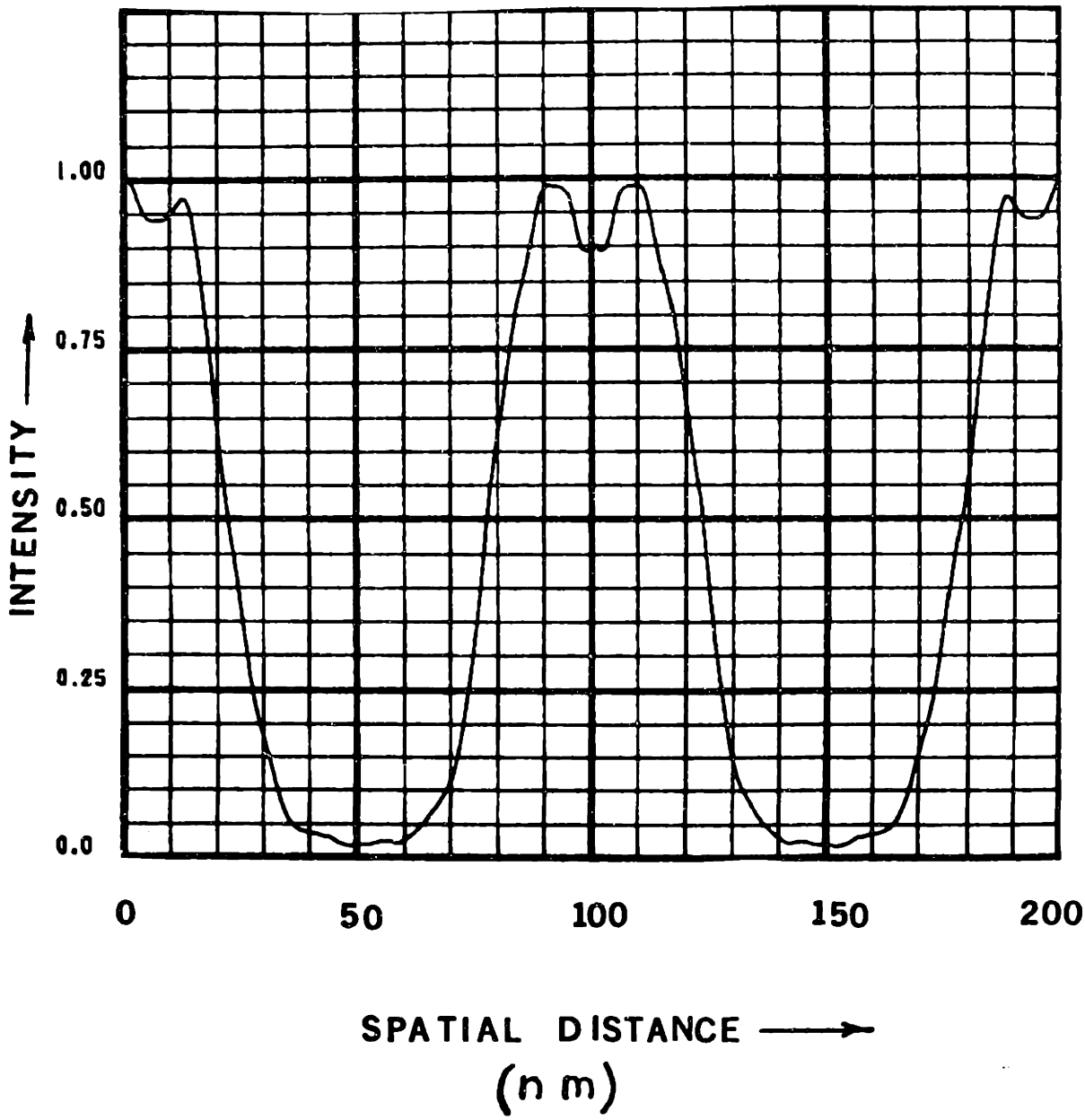

Figure IV-4 Computer calculation of the near field diffraction pattern of a highly opaque grating (b = 0) for $\beta = 8$, $Z = p^2/2\lambda$, $p = 200$ nm and $\lambda = 5$ nm.

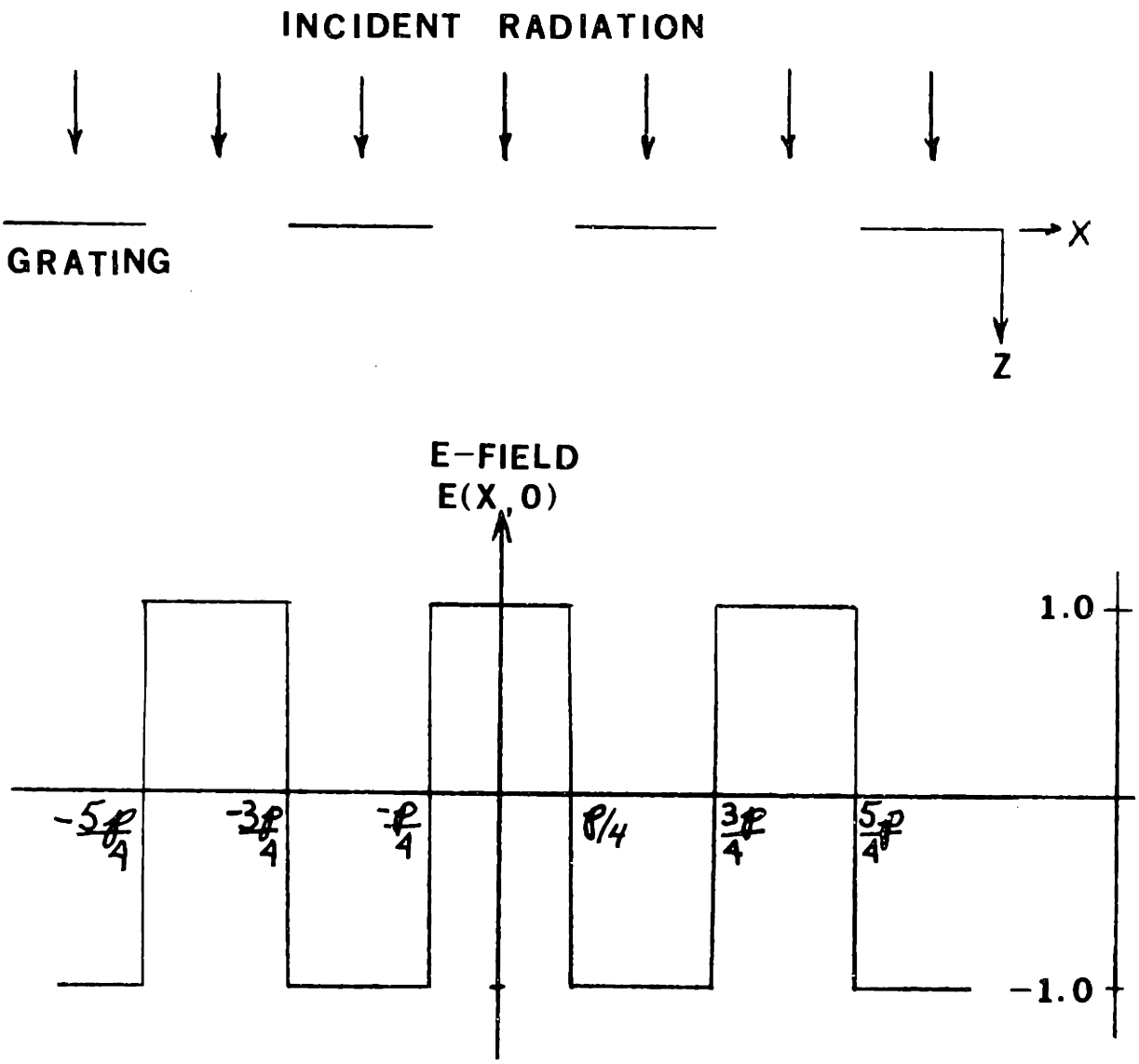

Figure IV-5 The transmitted electric field at the plane of the grating (E(X,0)) for a phase grating.

Notice that the even order indices are identically zero. The electric field pattern for a phase grating is (from equation 4-9):

$$E(x,z) = 2 \sum_{n=1}^{n_o} B_n \, \mathrm{Cos}(nKx) \, \exp(jk_z(n)z)$$

but since, for n even, $B_n = 0$, the equation can be written as:

$$E(x,z) = 2 \sum_{n=1}^{n_o/2} B_{(2n-1)} \, \mathrm{Cos}((2n-1)Kx) \, \exp(jk_z(2n-1)z) \qquad (4\text{-}24)$$

A factor of exp(jkz) can be factored out of the summation, and, using equation 4-13, the electric field is:

$$E(x,z) = 2 \exp(jkz) \exp\left(\frac{-jz\pi\lambda}{p^2}\right) \cdot$$

$$\sum_{n=1}^{n_o/2} B_{(2n-1)} \, \mathrm{Cos}((2n-1)Kx) \, \exp\left(\frac{-jz\pi\lambda}{p^2} (4n^2 - 4n)\right) \qquad (4\text{-}25)$$

Analyzing the electric field pattern in Figure IV-6, (a "trial" function) we find that its Fourier series is:

$$\mathcal{E}_3(x) = 2\sum_{n=1}^{\infty} C_{(2n-1)} \, \mathrm{Cos}((2n-1)Kx) \qquad (4\text{-}26)$$

where

$$C_n = \frac{2}{n\pi} \left(\mathrm{Sin}\left(\frac{n\pi}{4}\right) + \mathrm{Sin}\left(\frac{3n\pi}{4}\right)\right) \qquad (4\text{-}27)$$

For $n_o \to \infty$, the intensity patterns obtained from the electric fields expressed in equations 4-25 and 4-26 are equivalent when:

$$B_{(2n-1)} \exp\left\{\frac{-jz\pi\lambda}{p^2} (4n^2-4n)\right\} = C_{(2n-1)} \qquad (4\text{-}28)$$

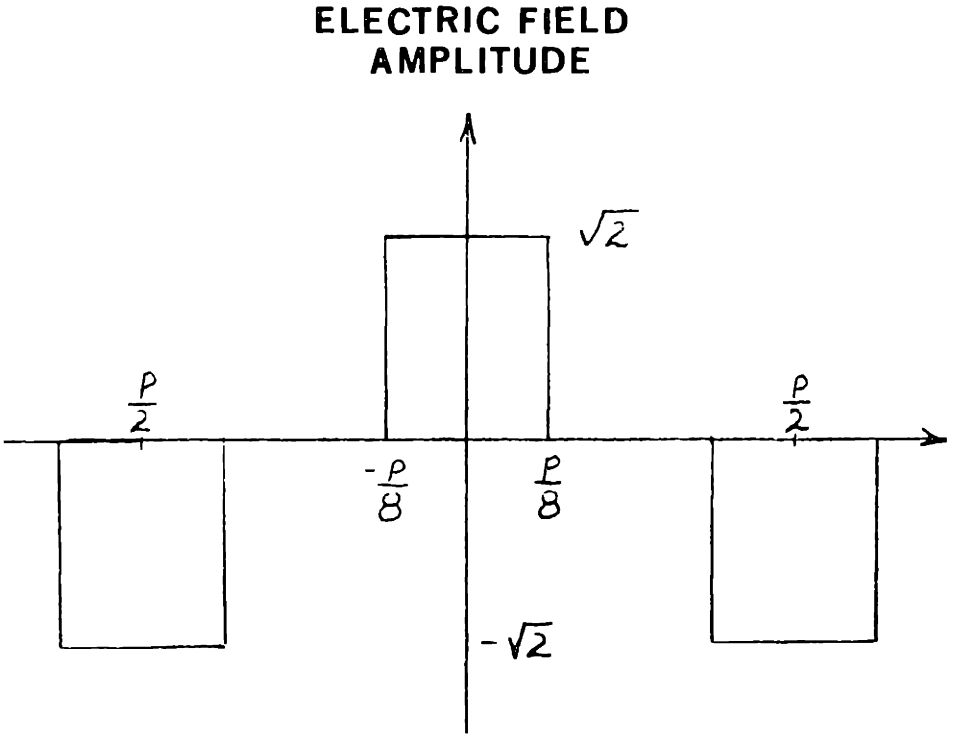

$$\mathcal{E}_3(x) = 2\sum_{n=1}^{\infty} C_{(2n-1)} \cos((2n-1)Kx)$$

Figure IV-6 The near field diffraction pattern of a phase grating is compared to the electric field pattern illustrated above. The former approaches the later at $Z = t_1 p^2/8\lambda$, as $n_0 \to \infty$.

which is satisfied when:

$$z = t_1 \cdot (p^2/8\lambda) \tag{4-29}$$

where t_1 is any odd integer. Therefore, the intensity pattern observed at any of the doubling distances defined by equation 4-29, will approach (as $n_0 \to \infty$) a square wave pattern with period (p/2). As an illustration of this, the intensity pattern of a phase grating was calculated by a computer by using equation 4-10. The calculation assumed a 200 nm "parent" phase grating, such as that illustrated in Figure IV-5, and which was illuminated by a plane wave with a wavelength of 5 nm. At a distance of 1 μm, corresponding to $z = p^2/8\lambda$, the desired "doubled" image is observed, Figure IV-7.

IV-E "DOUBLING" WITH $p > \lambda > p/2$

When a grating of period p is illuminated by a plane wave of wavelength λ, where $p > \lambda > p/2$, only the zeroth and first order diffracted beams are present. To analyze the near-field diffraction pattern of such a structure at distances from the grating comparable to the wavelength is difficult,[39,52,70,71] and in fact, cannot be done exactly. However, the case of $p > \lambda > p/2$ is of special interest. The above expressions (equations 4-1 and 4-2) for the field in front of a grating are not valid, as discussed earlier, for the case $\lambda \sim p$, and the method used thus far cannot correctly calculate the magnitudes and relative phases of the diffracted beams. Nevertheless, away from evanescent fields, the near field diffraction pattern can still be thought to be a superposition of the zeroth and first orders, which yields:

$$E(x,z) = B_0 \exp(jkz) + 2 B_1 \text{Cos}(Kx) \exp(jk_z z) \tag{4-30}$$

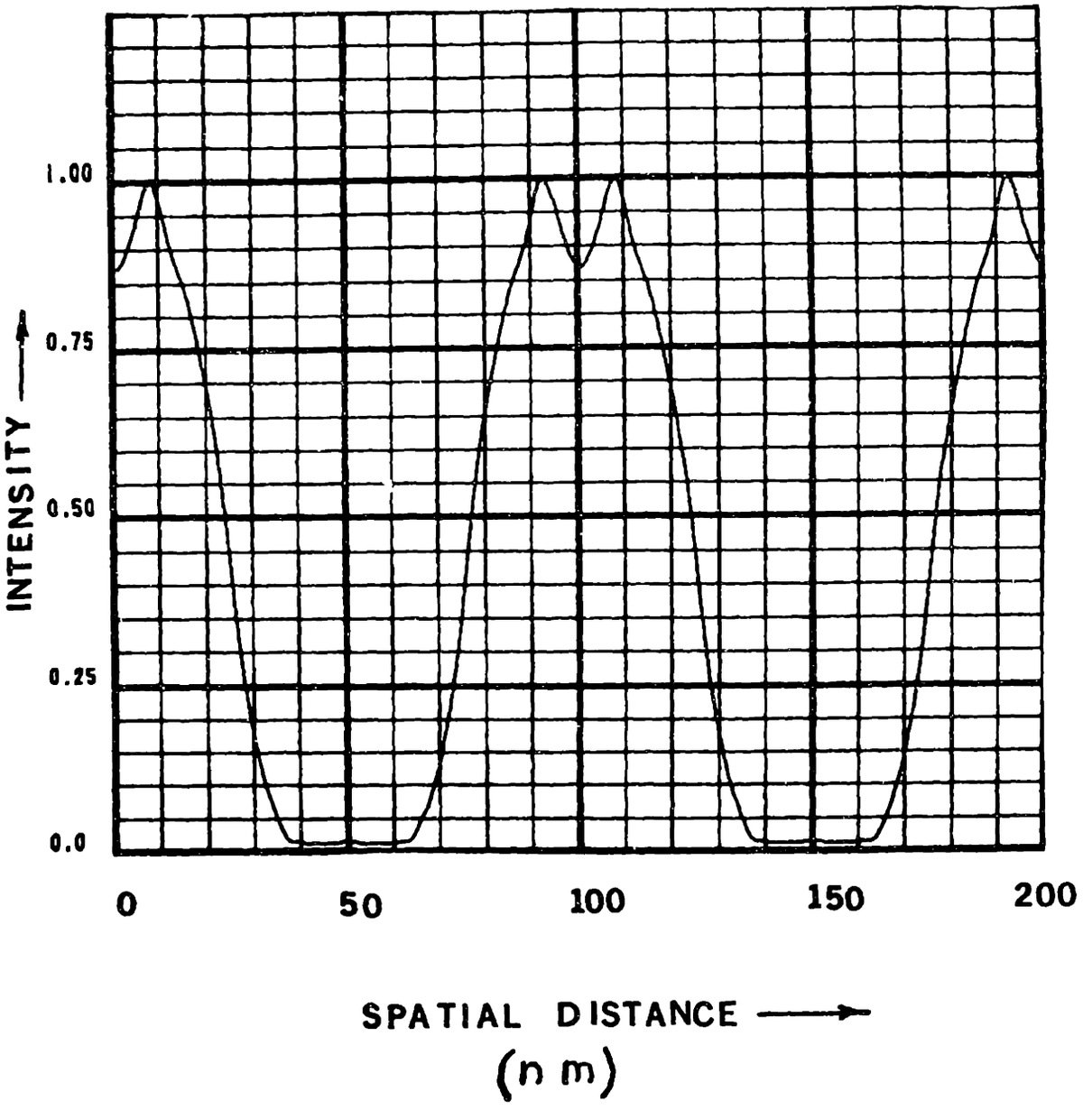

Figure IV-7 Computer calculation of the near-field diffraction pattern of π phase grating for p = 200 nm, λ = 5 nm and $Z = p^2/8\lambda$.

and

$$I(x,z) = |B_0|^2 + 4\, B_0\, B_1\, \mathrm{Cos}(Kx)\, \mathrm{Cos}((k-k_z)z) + 4|B_1|^2\, \mathrm{Cos}^2(Kx) \qquad (4\text{-}31)$$

At the planes where $\mathrm{Cos}((k-k_z)z) = 0$, the intensity pattern is simply a sinusoidal pattern with half the period of the original grating, superimposed onto a uniform background. This is true for a grating with any arbitrary transmission and phase shift through the grating lines, and any line-to-period ratio. In order to optimize the "doubled" intensity pattern, the values of B_0 and B_1 need to be at a minimum and maximum, respectively. A special situation arises for a pure phase grating of π phase shift, such that there exists no zeroth order diffracted beam, and only the first order diffracted beams exist. In this case, doubling will occur at all distances in the near field.[9,28] Note that, from equation (4-31), an oscillatory behavior can be expected. This has been verified experimentally in section V-D.

IV-F GENERAL SPATIAL PERIOD DIVISION ANALYSIS

The technique of spatial period division should have its greatest impact on the fabrication of sub-100 nm periodic structures. Holographic lithography is a simple and useful technique which can be used to produce gratings with periods from approximately 0.2 μm to several microns. However, it is in the fabrication of the finer grating periods which are inaccessible by holographic lithography, that spatial period division will likely make its largest contribution. To produce the desired finer gratings with a square wave-like intensity pattern, it is necessary to illuminate the grating with radiation of wavelength much less than the spatial

period to be produced, so that the necessary diffracted orders exist ("doubling" with $p > \lambda > p/2$ is a special case exception to this general rule and yields a sinusoidal, rather than a square-wave like intensity pattern). It is therefore clear that the radiation source for most applications should have $\lambda \lesssim 10$ nm, and it is the techniques of x-ray lithography which will play the role of recording the finer grating periods. Aside from the UV synchrotron, reliable sources below 100 nm exist only in the soft x-ray regime, below 10 nm. The x-ray sensitive resist with the highest known resolution[56] is PMMA, and it is also well known that PMMA is a very high contrast resist. Specifically, the dissolution rate of exposed PMMA[24] is proportional to the absorbed energy raised to the 3.4 power (rate $\sim$ (energy)$^{3.4}$). This indicates that a factor of two increase in exposure will increase the dissolution rate of PMMA by a factor of 10 in the appropriate developer. Therefore, an intensity contrast (ratio of the intensity maximum to intensity minimum) of two is generally sufficient to record a useful grating pattern in PMMA.

In the soft x-ray regime, it is difficult to obtain either complete opacity (complete attenuation) or π phase shift through grating lines. To achieve either requires thick layers of dense materials, and the two effects cannot be separated. It is therefore necessary to calculate the diffraction pattern for x-ray spatial period division as a function of both the phase shift and transmission through the grating lines. For the general transmission function of a grating, Figure II-1, the complex Fourier series coefficients are:

$$B_o = \frac{1}{p}\left[\frac{2p}{\beta} + be^{j\phi}\left(p - \frac{2p}{\beta}\right)\right] \qquad (4\text{-}7)$$

$$B_n = \frac{\mathrm{Sin}(\frac{2n\pi}{\beta})}{n\pi}\,[1-be^{j\phi}] \tag{4-8}$$

and the observed intensity pattern is:

$$I(x,z) = |B_o|^2 + 4\sum_{n=1}^{n_o} B_o\,B_n\,\mathrm{Cos}(nKx)\,\mathrm{Cos}((k-k_z(n))z) + \tag{4-10}$$

$$4\sum_{n=1}^{n_o}\sum_{n=1}^{n_o} B_n\,B_q\,\mathrm{Cos}(nKx)\,\mathrm{Cos}(qKx)\,\mathrm{Cos}((k_z(n)-k_z(q))z)$$

The m^{th} spatial period division (an intensity pattern with period p/m) occurs when the n=m coefficient of the single summation term is a maximum. This implies that B_m must be a maximum, and $\mathrm{Cos}((k-k_z(m))z)$ equals one. In addition, the contribution from those double summation terms which add construcively to the desired spatial period division pattern are also a maximum. The most important is the n = q = m/2 term for "m" even, and the q = (m+1)/2 and n = (m-1)/2 terms for "m" odd. Obviously, n and q are interchangeable. For "m" even, there is no z dependence for the n = q term, and this term is a maximum for all z. For "m" odd, the requirement is satisfied at the proper location of z, where the product of the (m+1)/2 and the (m-1)/2 terms are a maximum. Finally, the contribution from the n = m/2 adds destructively to the desired pattern, and this term is a minimum when $\mathrm{Cos}((k-k_z(m/2))z)$ is minimum. Taken collectively, optimum spatial period division occurs when:

$$\beta = 4m \tag{4-32}$$

and

$$z_m = p^2/m\lambda \tag{4-33}$$

It is clear that only a few of the terms of the single and double summation series have been considered. At this point it is more instructive to analyze the electric field pattern at the proper location, z, for an m^{th}-order spatial period division. For $\lambda << p$, Equation 4-9 becomes (factoring out a phase factor of exp(jkz)):

$$E(x,z) = B_0 + 2 \sum_{n=1}^{n_o} B_n \cos(nKx) \exp\{j\pi n^2/m\} \qquad (4\text{-}34)$$

As in the case of "doubling", the summation can be written as a sum of terms, each of which corresponds to an E-field pattern that approaches a square-wave form as $n_o \to \infty$. Any individual electric field pattern may have a period, p, but taken collectively, the resulting intensity pattern has period (p/m). For example, for m=4, the summation in equation 4-34 can be written as sums over the odd and even indices. For $n_o \to \infty$, the summation over the even indices gives the square wave pattern in Figure IV-8b, and the summation over the odd indices gives the square wave pattern in Figure IV-8a. Superimposing the two electric field patterns, and squaring the sum, yields an intensity pattern of period p/4. This process can be repeated for all values of m, and, as an illustration of this, the spatial period division of a highly opaque grating (b = 0) with period p, is shown in Figure IV-9 under optimum conditions (i.e. $\beta = 4m$ and $z = p^2/m\lambda$) and for divisions of m = 2 through 10, calculated by using equation 4-10. For these computer calculations, a grating period of 200 nm, and a monochromatic plane wave source with a wavelength of 1 nm was assumed.

Since most materials exhibit both finite attenuation and phase shifts for incident soft x-ray radiation, it must be assumed that in any real

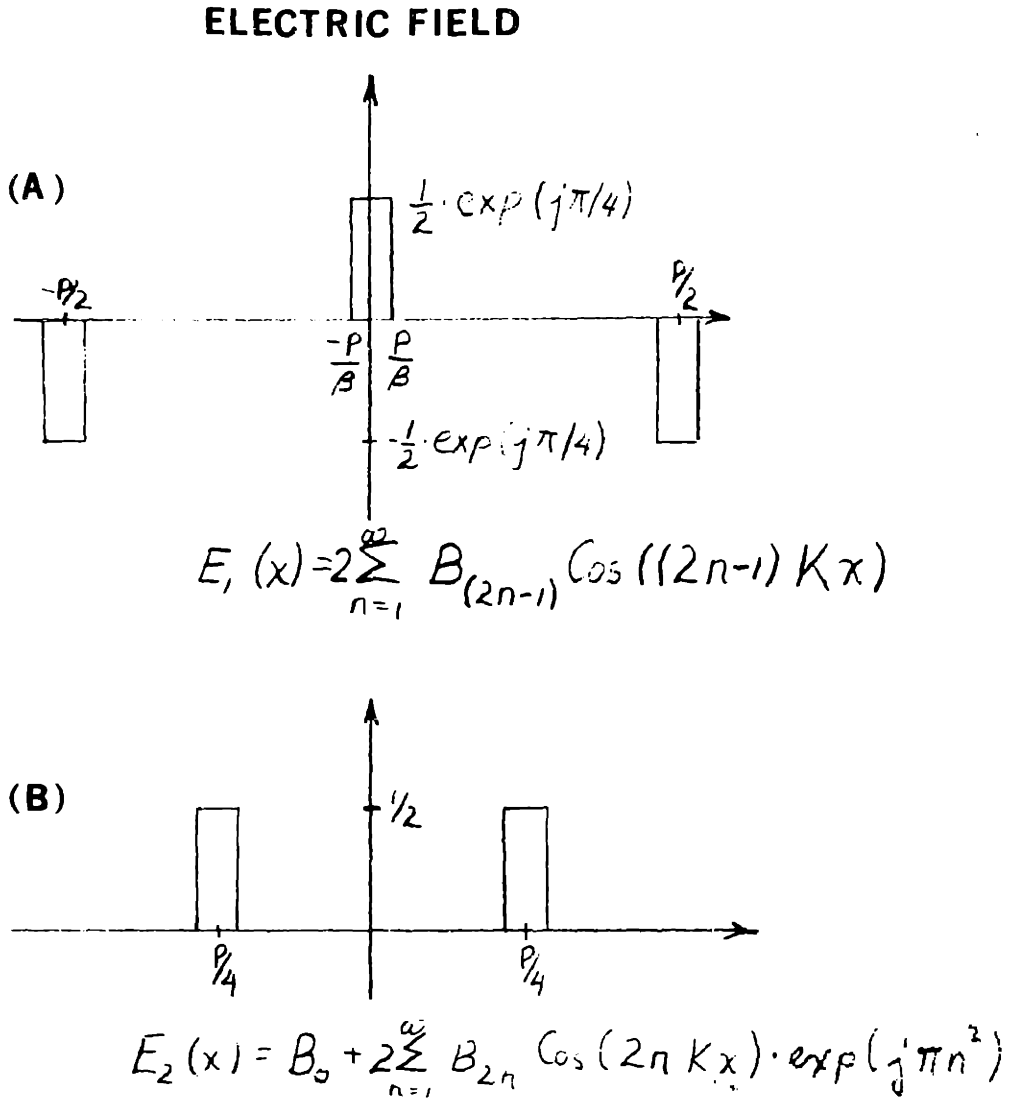

Figure IV-8 The near field diffraction pattern of an "m^{th}" spatial period division, for m = 4, is the superposition of two periodic electric fields, which, when superimposed, produces an intensity pattern of period p/4. (A) is the summation over the odd indices in equation (4-29), and (B) is the summation over even indices.

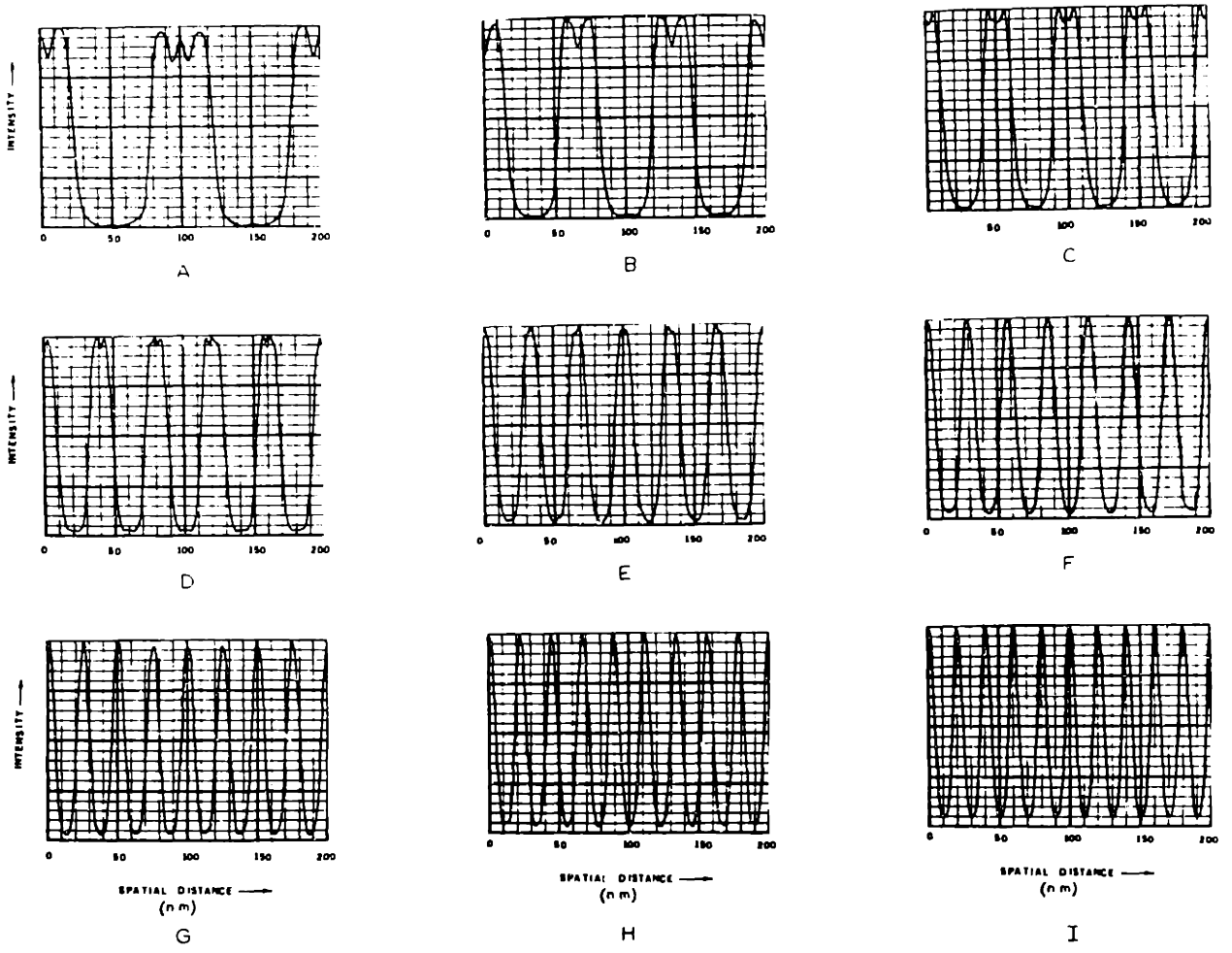

Figure IV-9 The near field diffraction pattern of a highly opaque grating, as discussed in the text, illustrating spatial period division under optimum conditions ($\beta = 4$ m and $z = \rho^2/m\lambda$).

A) m = 2	B) m = 3	C) m = 4
D) m = 5	E) m = 6	F) m = 7
G) m = 8	H) m = 9	I) m = 10

experiment, the grating lines will not be fully opaque, and that some phase shift through the grating lines occurs. To analyze the quality of the spatial period division pattern under conditions of partial transmission, the intensity pattern at $z = p^2/m\lambda$ as a function of phase shift and transmission through the grating lines was computed. To analyze the depth of field of the spatial period division pattern, the intensity pattern in the vicinity of the proper location, z, for the m^{th} spatial period division was computed.

The partial transmission and phase shifts through the grating lines will affect the Fourier series coefficients, B_n (see equations 4-7 and 4-8). As the thickness of the grating lines increase, the absorption and phase shifts in the grating lines increase. For a gold grating, the measured absorption[17] and phase shifts[17] at the carbon-K x-ray are 128 dB/μm and 1°/mm, respectively. As the grating line thickness increases, it is clear from (4-7) and (4-8) that the value of B_0 decreases and the values for B_n increase. This continues until a $\phi = \pi$ phase shift is reached, after which the values of B_0 and B_n increase and decrease, respectively. This oscillatory behavior in the values of B_0 and B_n continues until the attenuation is very large ($b \backsim 0$). For general m^{th} order spatial period division, the best results are obtained from the diffraction pattern of a highly opaque grating. In practice, it is difficult to obtain full opacity. For example, a gold thickness of 180 nm corresponds to an attenuation of 23 dB ($b^2 = 5 \times 10^{-3}$) and a $\phi = \pi$ phase shift for the carbon-K x-ray. Whereas this may seem to be sufficient attenuation, examination of the near field diffraction pattern of an m^{th} spatial period division will reveal that the widths of the lines are not all the same for a given inten-

sity level. Spatial period division is very sensitive to the gold thickness, even for gold thicknesses in excess of 180 nm. This is explained by the fact that the diffraction pattern is a coherent effect, and is sensitive to the phase of any transmitted wave. For $b^2 = 5 \times 10^{-3}$, the relative electric field strength of the radiation transmitted through the lines is 0.07, and this produces a background. The m^{th} order division is composed of square wave electric field "pulses", which may have components that are either positive or negative relative to this background. The background will add to the square wave pulses so that the positive pulses will have higher peak electric fields, while the negative pulses will be diminished. As an example, for m = 4, if an individual electric field pulse were -0.5 relative units and another were +0.5 relative units, then the transmitted radiation would change the electric field strengths to -0.43 and + 0.57, respectively. The difference in the resulting peak intensities would be a factor of 1.75, which is unacceptable for replication purposes.

In the following calculations, the characteristics of a carbon-K x-ray source is assumed (λ = 4.48 nm, 2% bandwidth) and the measured attenuation and phase shift through gold is used. The near field diffraction pattern a 0.2 μm period grating is calculated. The incident x-ray beam is assumed to be collimated and at normal incidence to the grating. A 20 nm resolution in the recording medium is also assumed. This effect can be simulated by convolving the near field diffraction pattern with a 20 nm wide rectangular pulse. The "doubling" of a 200 nm period grating would require a grating with $\lesssim$ 50 nm spaces ($\beta \geq 8$). Figure IV-10 is a plot of the near field diffraction pattern at $z = p^2/2\lambda$ as a function of gold thickess, from 120 nm to 400 nm. Although the maximum thickness obtained

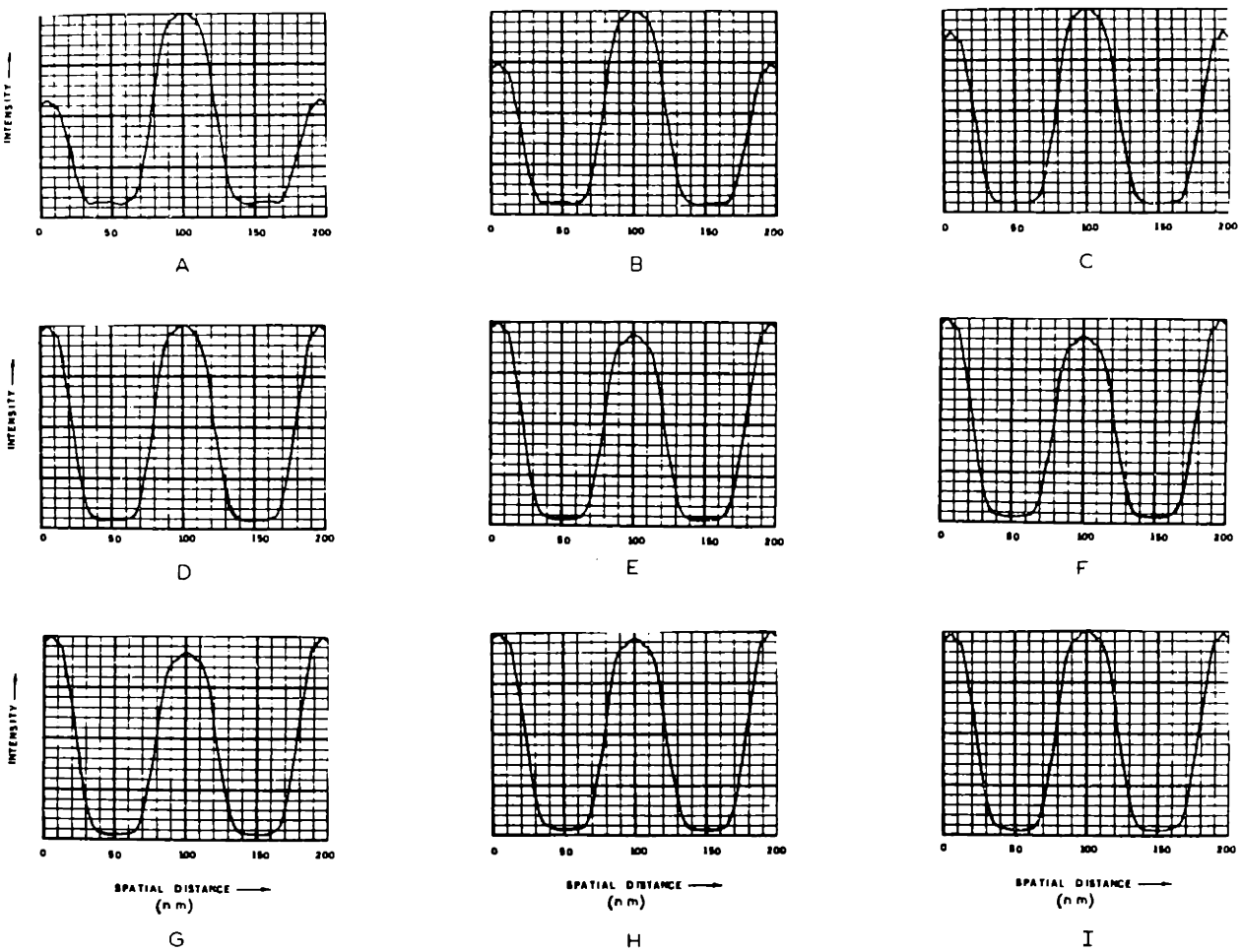

Figure IV-10 The near field diffraction pattern of a grating as a function of increasing attenuation and phase shift (increasing gold thickness), for $\beta = 8$ and $z = p^2/2\lambda$ ($m = 2$).

A) gold thickness = 120 nm
B) 140 nm
C) 160 nm
D) 180 nm
E) 200 nm
F) 220 nm
G) 250 nm
H) 300 nm
I) 400 nm

so far for this experiment was 250 nm, a thickness of ∿ 400 nm should be feasible. As is evident, the pattern changes quite dramatically for gold thicknesses up to approximately 180 nm, but does not change appreciably for thicknesses beyond 220 nm. For a high contrast recording medium, such as PMMA, gold thicknesses in excess of approximately 180 nm should be suitable for "doubling", but thinner layers would be unsuitable. For gold thicknesses less than 180 nm, adjacent intensity peaks differ by more than 20%. This will result in a factor of two, or more, difference in the development rate between the two peaks, and the fundamental grating period would be evident as linewidth variations in the developed pattern.

The same calculations have been made for m = 3 and m = 4, and are shown in Figures IV-11 and IV-12. It is evident from these plots that the higher spatial period divisions are more sensitive to any partial transmission by the gold, and for adequate spatial period division, a gold thickness in excess of ∿ 250 nm is required.

The effects of changing the line-to-period ratio of the parent grating (varying β) is simply to change the peak widths in the near field diffraction pattern. These peak widths are approximately equal to the transparent region (spaces) of the parent mask. For example, a parent grating with spaces equal to $2p/\beta$ will have a diffraction pattern with intensity peak widths (FWHM) equal to approximately $2p/\beta$. Obviously, the value of $2p/\beta$ must be less than the period of the desired near field intensity pattern. As an illustration, Figure IV-13 shows the "doubling" of a 0.2 μm period grating with various values of β. A fully opaque grating (b = 0) is assumed, and plane waves with the characteristics of the C_K x-ray are incident upon the grating.

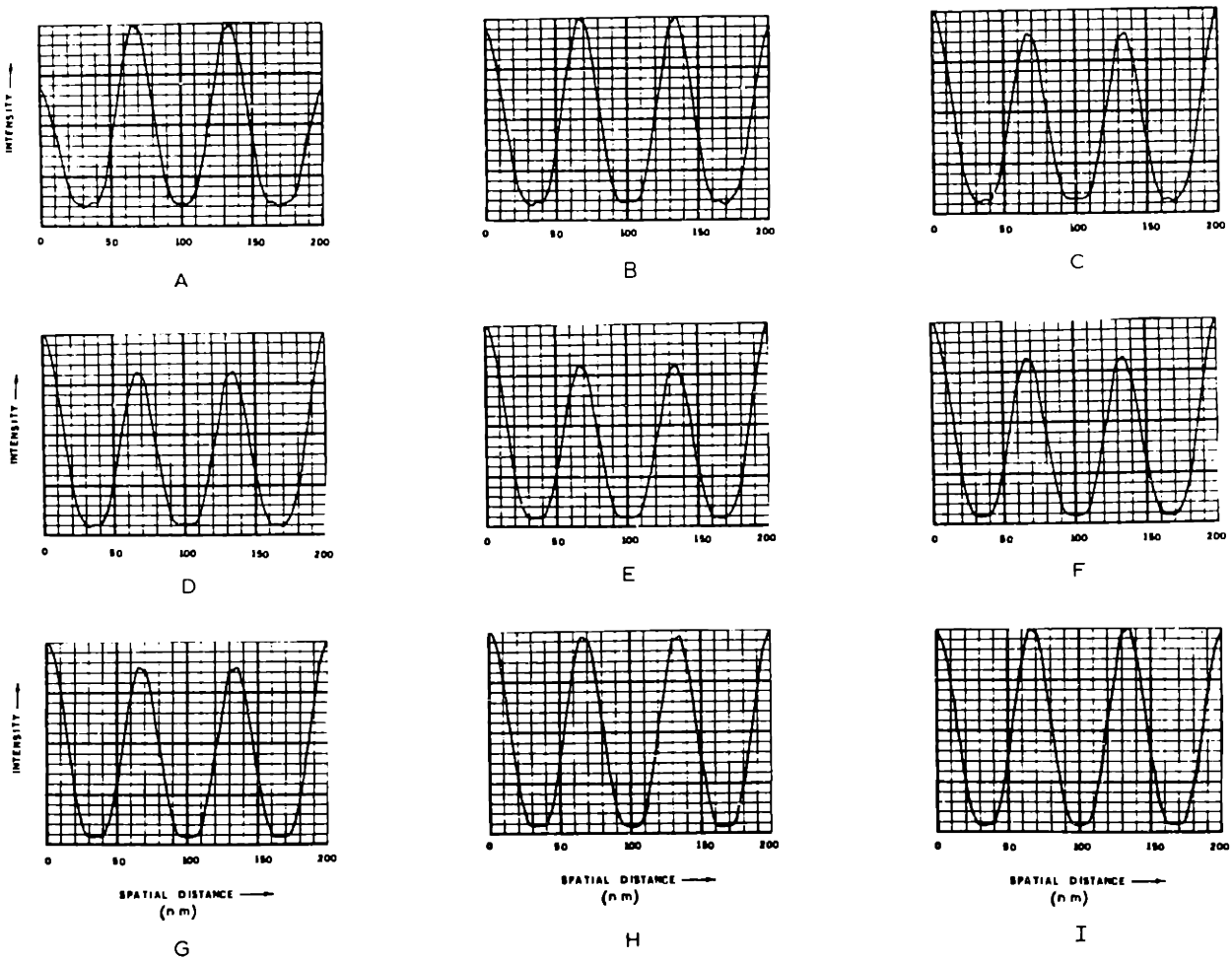

Figure IV-11 The near field diffraction pattern of a grating as a function of increasing attenuation and phase shift (increasing gold thickness), for $\beta = 12$ and $z = p^2/3\lambda$ ($m = 3$).

A) gold thickness = 120 nm
B) 140 nm
C) 160 nm
D) 180 nm
E) 200 nm
F) 220 nm
G) 250 nm
H) 300 nm
I) 400 nm

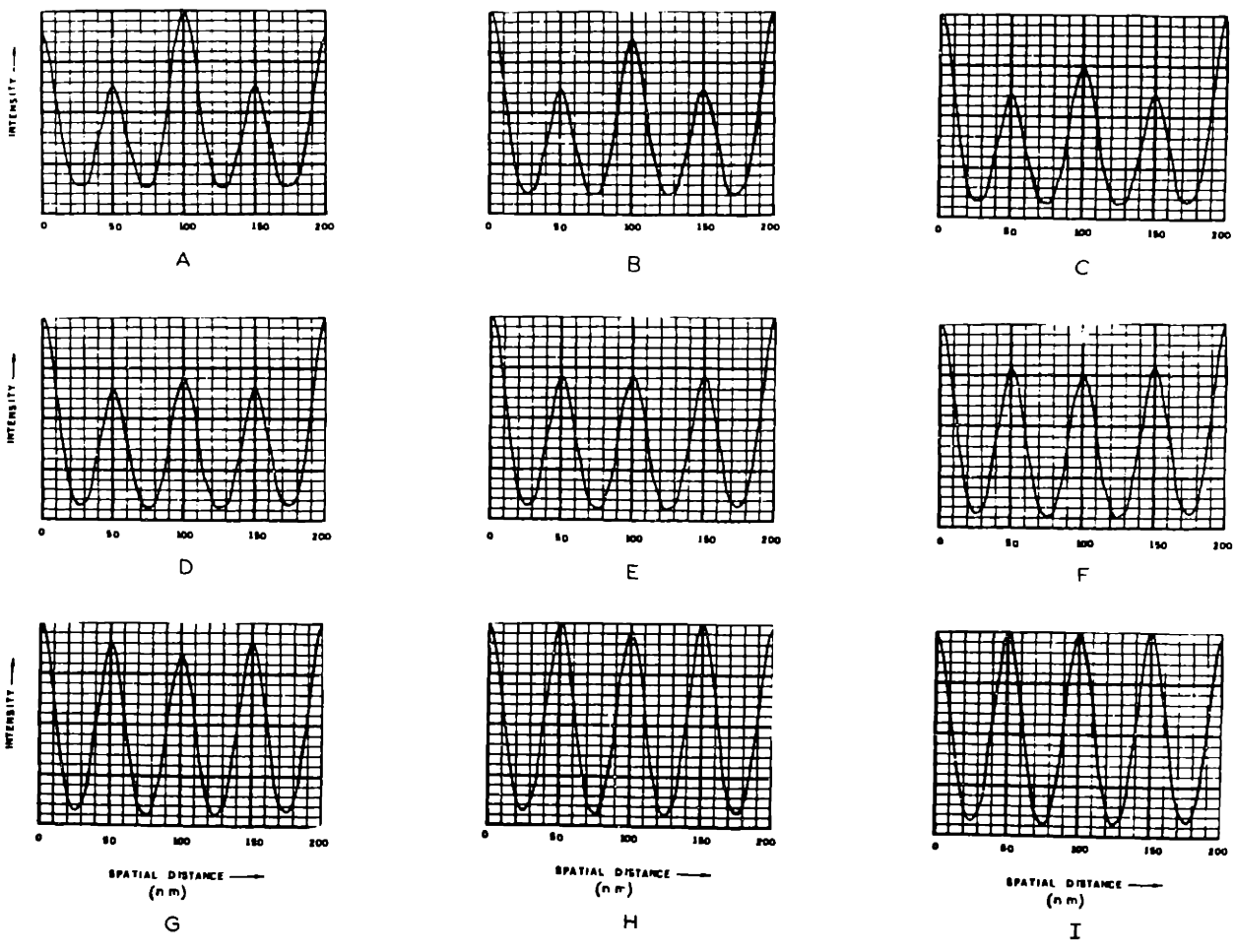

Figure IV-12 The near field diffraction pattern of a grating as a function of increasing attenuation and phase shift (increasing gold thickness), for $\beta = 16$ and $z = p^2/4\lambda$ ($m = 4$).

A) gold thickness = 120 nm B) 140 nm
C) 160 nm D) 180 nm E) 200 nm
F) 220 nm G) 250 nm H) 300 nm
I) 400 nm

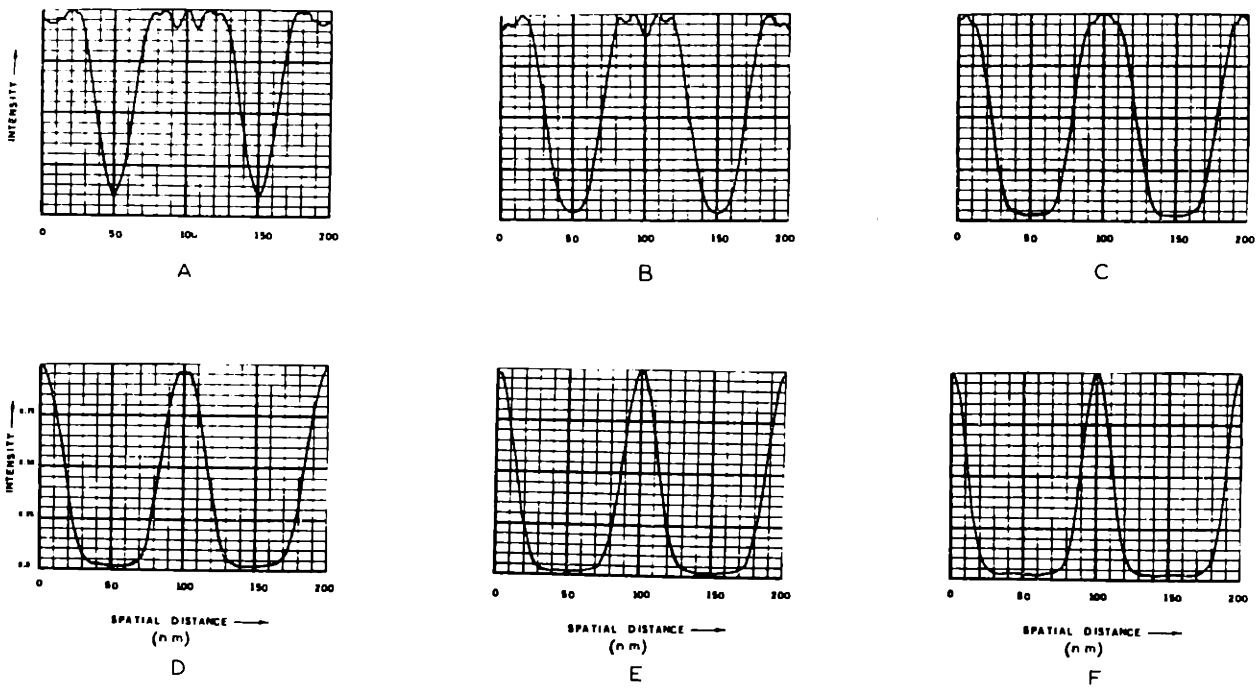

Figure IV-13 The near field diffraction pattern of a grating as a function of varying line-to-period ratio (varying β) for $b = 0$, $z = p^2/2\lambda$ and $m = 2$.

A) $\beta = 5$ B) $\beta = 6$

C) $\beta = 8$ D) $\beta = 10$

E) $\beta = 12$ F) $\beta = 16$

Lastly, it is important to analyze the near-field diffraction pattern in the vicinity of the plane, $z = p^2/m\lambda$. The terms that are z dependent in the near field pattern are dependent through a $\cos((k-k_z(n))z)$ factor. For $\lambda << p$, this is a slowly oscillatory function, and it is expected that the depth of field can be large compared to a wavelength. Figures IV-14, IV-15 and IV-16 illustrate this point by plotting the near field diffraction pattern of a 200 nm period grating, in the vicinity of the m^{th} spatial period division image, for m = 2, 3 and 4. For these calculations, b = 0 and $\beta = 4m$, and the characteristics of the C_K x-ray are again assumed. From these calculations, the quality of the m^{th} spatial period division image as a function of distance from the grating is illustrated.

From a simple calculation, the distance in the near field diffraction pattern between two successive divisions is:

$$\Delta z = \frac{p^2}{(m^2+m)\lambda} \tag{4-35}$$

A rough estimate of the depth of field can be made by dividing this region into three sub-regions, the first having a diffraction of period p/m, the second is a transition region, and the third region has a diffraction pattern of period p/(m+1). The approximate depth of field (d.o.f.) of the m^{th} order division is then:

$$\text{d.o.f.} = \frac{1}{3}\frac{p^2}{(m^2+m)\lambda} \tag{4-36}$$

As another illustration of the m^{th} spatial period division image as a function of distance from the grating, and with the desire to produce sub-

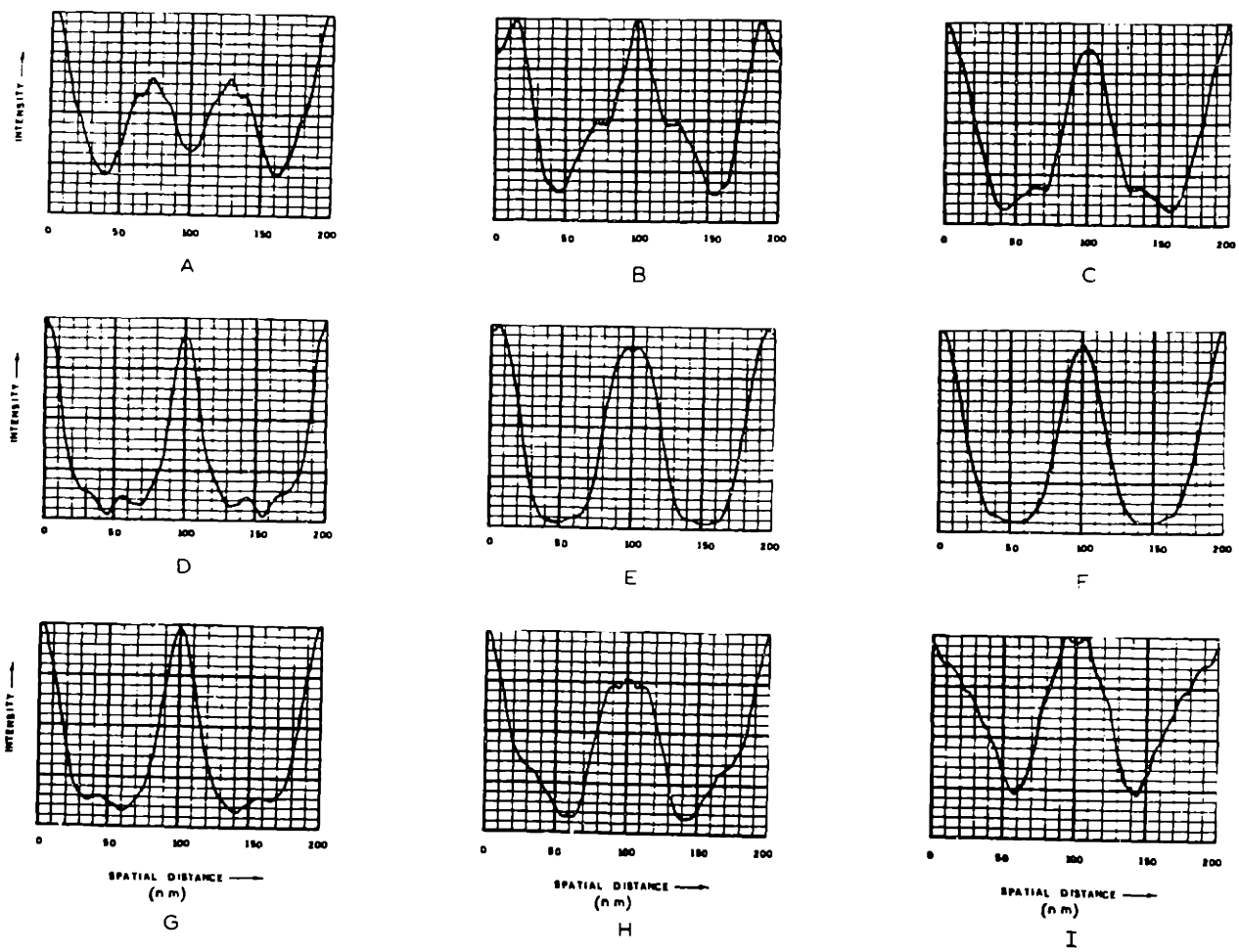

Figure IV-14 The near field diffraction pattern of a grating as a function of distance, z, for $\beta = 8$, $b = 0$ and $m = 2$. Optimum "doubling" would occur at $z = p^2/2\lambda = 4.46$ μm.

A) z = 3.5 μm
B) 3.75 μm
C) 4.0 μm
D) 4.2 μm
E) 4.4 μm
F) 4.6 μm
G) 4.8 μm
H) 5.0 μm
I) 5.25 μm

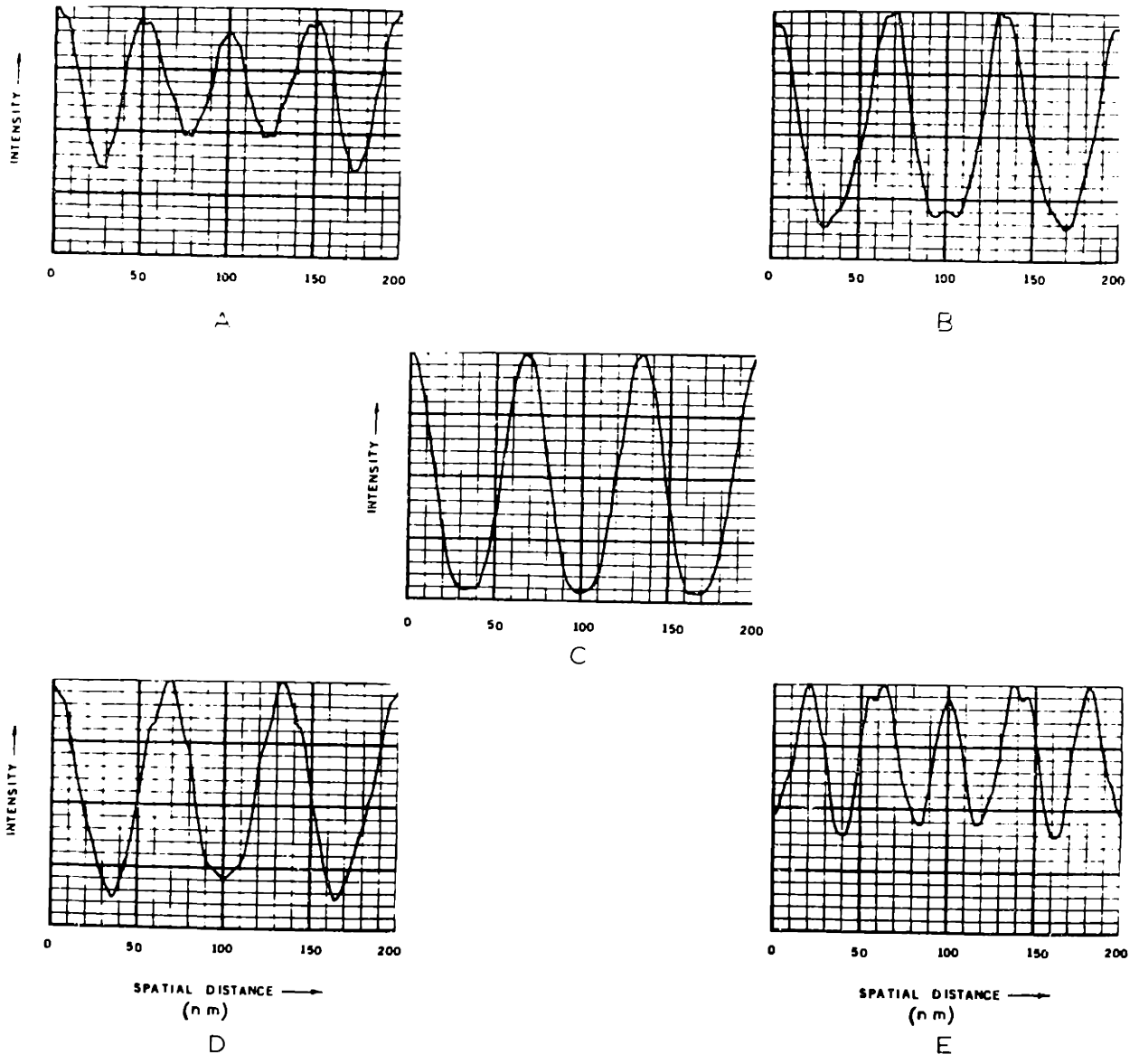

Figure IV-15 The near field diffraction pattern of a grating as a function of distance z, for $\beta = 12$, $b = 0$ and $m = 3$. Optimum spatial period division would occur at $z = p^2/3\lambda = 2.98$ μm.

A) z = 2.5 μm
B) 2.75 μm
C) 3.0 μm
D) 3.25 μm
E) 3.5 μm

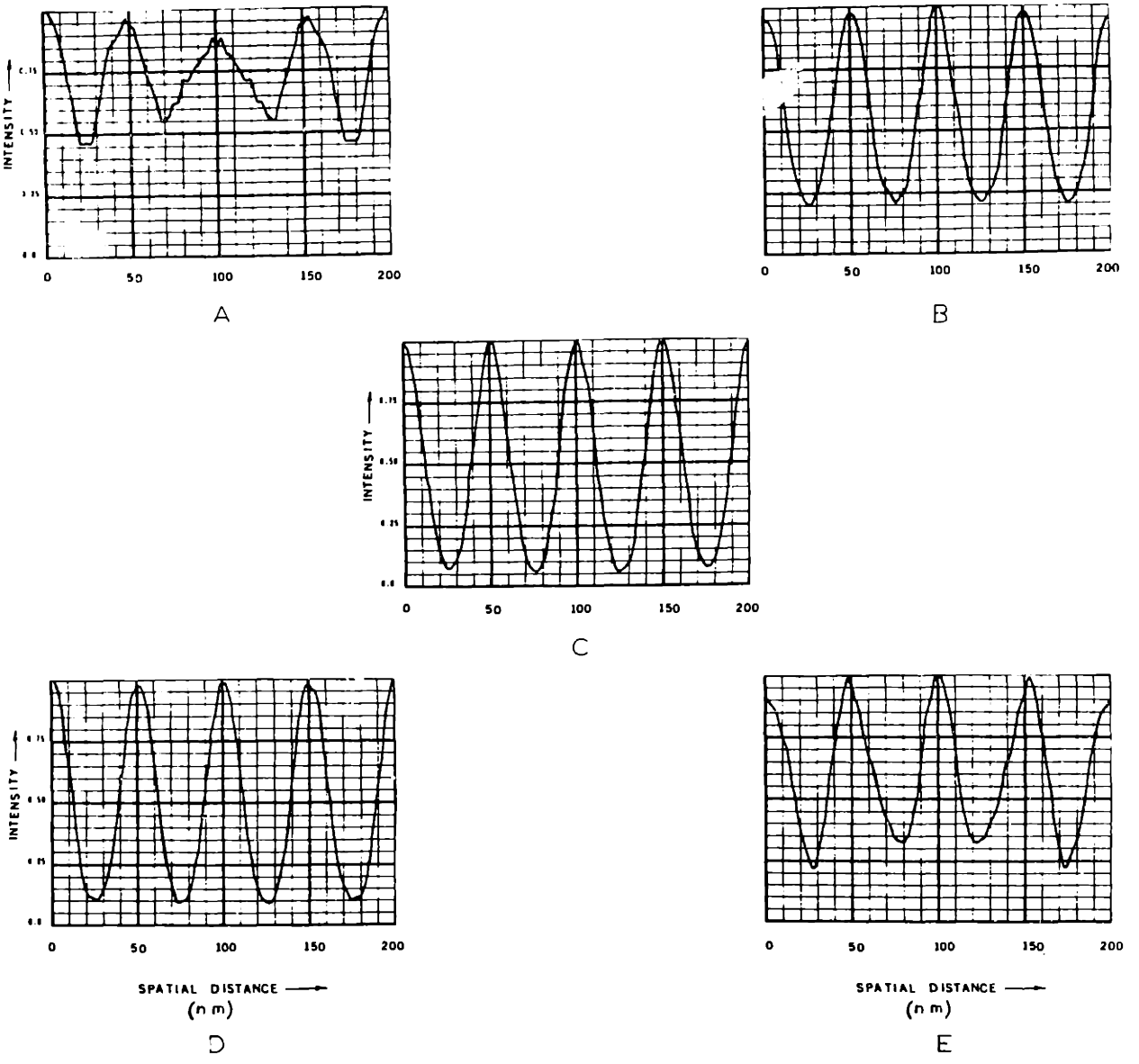

Figure IV-16 The near field diffraction pattern of a grating as a function of distance, z, for $\beta = 16$, $b = 0$ and $m = 4$. Optimum spatial period division would occur at $z = p^2/4\lambda = 2.23$ μm.

A) z = 2.0 μm

B) 2.1 μm

C) 2.2 μm

D) 2.3 μm

E) 2.4 μm

100 nm period grating, the near field pattern of a 200 nm period grating was plotted by a computer. Earlier in this thesis work, it was thought that a grating with spaces $\sim$ 20 nm wide and gold thickness $\sim$ 250 nm could be fabricated, and this grating would be illuminated with a broadband, synchrotron souce (10% bandwidth), centered at λ = 4.7 nm. This ultimately proved to be unfeasible, due to synchrotron availability. The penumbra associated with this source was determined by the source collimation $\sim$ 1 milliradian. Under these conditions, the near field diffraction pattern, as a function of distance from the grating, is illustrated in Figure IV-17, where the vertical axis represents the intensity. At distances from the grating corresponding to divisions of m = 2, 3, 4 and 5 ($z = p^2/m\lambda$), a cut-away view is exposed to reveal the intensity pattern at that plane.

It would be highly desirable to calculate the resist profile obtained by spatial period division by coupling the intensity pattern to a model for the resist development. Unfortunately, most development models do not take into account the finite resolution of the recording medium. Since sub-100 nm period gratings have features which are approaching the molecular size of the recording medium, one is hesitant to use large quantities of computer time on programs which may be suspect. New development models need to be formulated for the situation where the feature sizes to be recorded are near the effective resolution limits of PMMA ($\sim$ 20 nm).[56]

Since PMMA has a very high contrast (a 20% difference in exposure will result in a factor of two difference in development rate), there are several requirements on the intensity pattern for it to be useful for spatial period division. The recorded pattern should be free of any fundamental component, and this requirement implies:

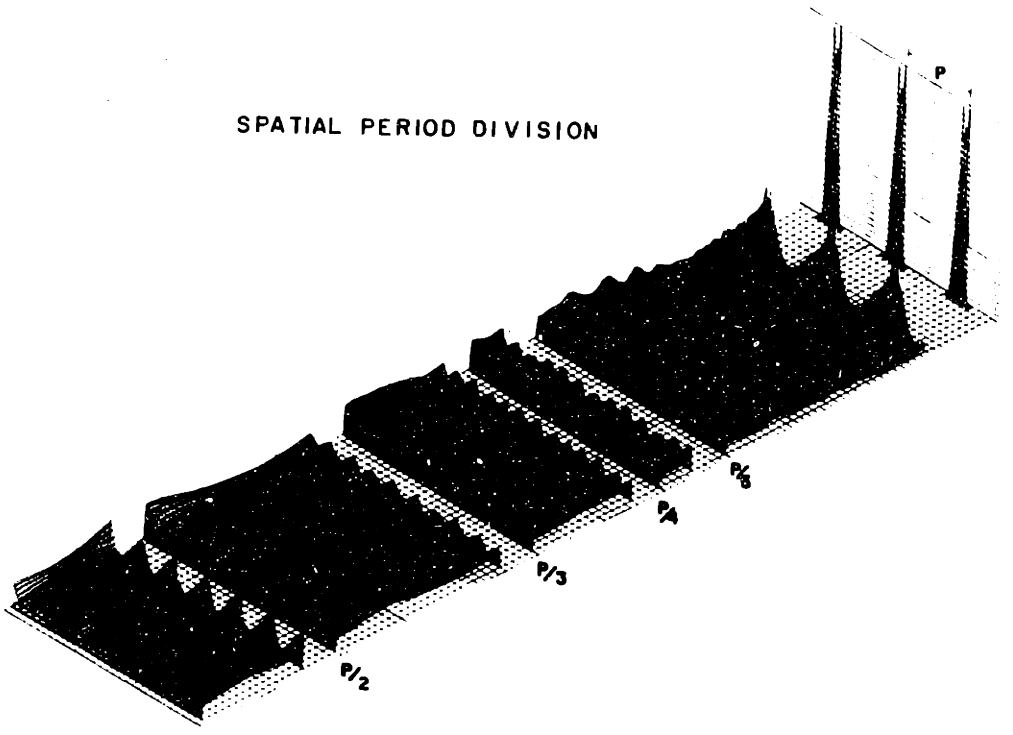

Figure IV-17 The near field diffraction pattern of a grating with $\beta = 20$ and a gold thickness = 250 nm, illustrating the planes of m^{th} spatial period division for m = 2, 3, 4, and 5. The characteristics of the sychrotron source mentioned in the text is assumed. Intensity is plotted on the verticle axis.

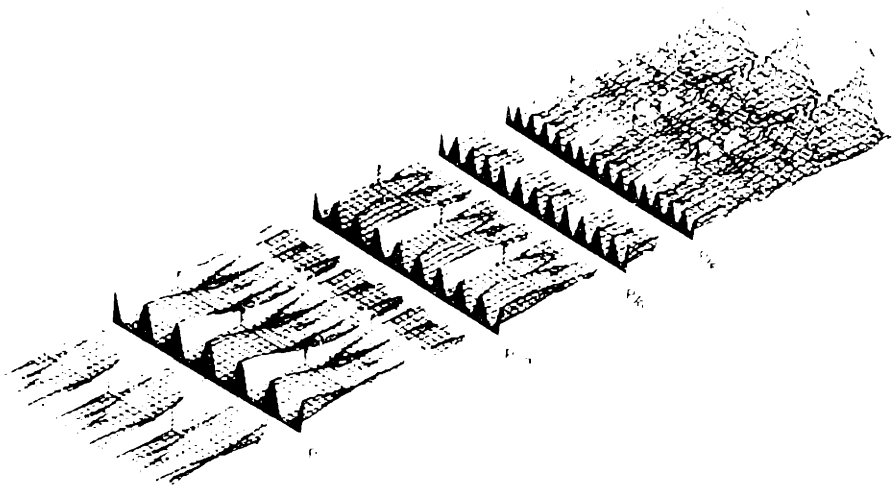

(1) The intensity maxima must be greater than three times the of intensity minima;

(2) Any individual intensity maximum cannot deviate by more than 20% from any other intensity maximum; otherwise, it will develop more rapidly than the other, leading to line widening through lateral development;

(3) The linewidths of the intensity maxima cannot vary by more than 20%.

Note that the value 20% is somewhat arbitrary, but serves as a good "rule-of-thumb". Taken together, these requirements impose strict limitations on the mask and the depth of field. It is, therefore, very important to carefully analyze the diffraction pattern as a function of all variables, z, b, ϕ, β and source characteristics. As a result, the "doubling" of a 0.2 μm period grating with C_K x-ray source is not a trivial task. From the computer calculations, it is clear that a thick gold grating ($\gtrsim$ 200 nm), with spaces < 50 nm, must be fabricated, and exact control of the gap is essential, z = 4.5 μm ± 0.3 μm. These are very severe restrictions. Furthermore, the spatial period division image must be analyzed for deviations from ideal conditions. As an example, a division of m = 3 is possible for a mask gold thickness of 140 nm (Figure IV-11b), but careful evaluation reveals that a change in the gold thickness by only 20 nm will destroy the image (the intensity peaks do not meet condition 2 above). It is very difficult to maintain a constant plated gold thickness over a square centimeter to ± 15 nm tolerances, and so, a better strategy for m = 3 might be to choose a "fully" opaque mask with gold thickness $\gtrsim$ 250 nm.

CHAPTER V

EXPERIMENTAL VERIFICATION OF SPATIAL PERIOD DIVISION

V-A INTRODUCTION

It was desired to test the applicability of spatial period division to the fabrication of sub-100 nm period gratings. Towards this end, three experiments were performed. The first experiment involved the spatial period division of a coarse period (> 10 μm) grating, illuminated by optical radiation. The second experiment involved the spatial period division (with m = 2) of a 199 nm period gold grating, illuminated by the carbon-K x-ray, to produce a 99.5 nm period grating in PMMA. The third experiment verified the spatial period division of a 199 nm period grating with a deep U.V. radiation source such that $p > \lambda > p/2$, as discussed in Section IV-E.

V-B OPTICAL TEST OF SPATIAL PERIOD DIVISION

To verify the theoretical predictions of chapter IV, a test at optical frequencies was performed[28], together with D.C. Flanders. Others[65-68] had observed this effect under similar experimental conditions, but none had done a detailed study to characterize the optimum conditions for spatial period division. The optical test that was performed used an orange filter ($\lambda \sim 600$ nm), with an incandescent source. The parent mask was a 16.9 μm period grating, etched into chromium. The grating pattern was originally exposed by electron beam lithography, by D.C. Shaver, and consisted of several grating areas, each with a different line-to-period ratio (different β's for different areas). The chromium grating was placed in an optical microscope, with the orange light incident on the grating from behind.

The microscope was then focused onto a plane in the near field diffraction pattern of the grating. In this manner, a magnified image of the near field diffraction pattern was obtained. Figure V-1 shows the results of this optical testing, as recorded in photographic film. The patterns were recorded at the plane corresponding to divisions by factors of 2, 3 and 4. This clearly demonstrated the technique of spatial period division. It also demonstrated an important feature, consistent with the theory presented in Chapter IV (although this was not fully understood at the time). Under the conditions of a slightly transparent parent mask, the patterns for m = 3 and m = 4 have some intensity peaks brighter than others; some fundamental component is evident. The attenuation in the parent mask was approximately 15 dB. From the computer calculations shown in Chapter IV for m = 3 and m = 4, it is necessary to have greater than approximately 30 dB attenuation to avoid the "fundamental" component.

V-C X-RAY SPATIAL PERIOD DIVISION

V-C-1 Introduction

The most difficult challenge of this thesis was to experimentally demonstrate spatial period division with soft x-rays. A 199 nm period grating, illuminated with the carbon-K x-ray (λ = 4.48 nm) was "doubled" to produce an intensity pattern with period 99.5 nm, which was recorded in a 150 nm thick layer of PMMA. The requirements on the "parent" grating, as discussed in Chapter IV, were that:

(1) the grating have narrow lines ($\beta \leq 8$);

(2) the gold lines have a thickness in excess of $\sim$ 180 nm.

The techniques of producing thick gold gratings, as discussed in Chapter

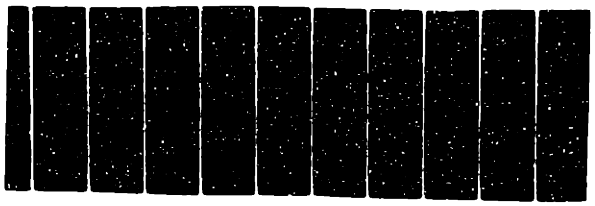

FUNDAMENTAL

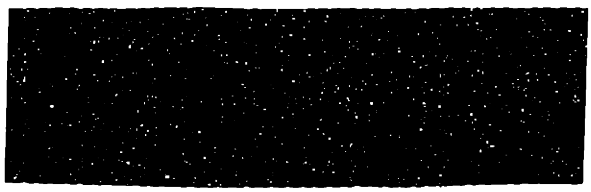

4X

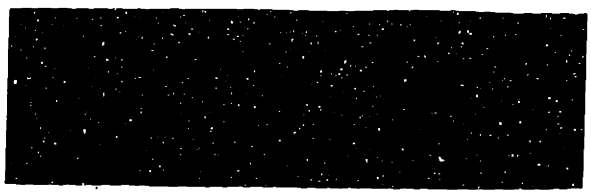

3X

2X

Figure V-1 Results of a spatial period division experiment at optical wavelengths. A 16.9 μm period grating was illuminated by a ∿ 600 nm source. At the appropriate locations, an m^{th} spatial period division (m = 2, 3 and 4) was observed. Notice that for m = 3 and 4, a fundamental intensity pattern is also evident, indicating partial transmission through the opaque grating lines.

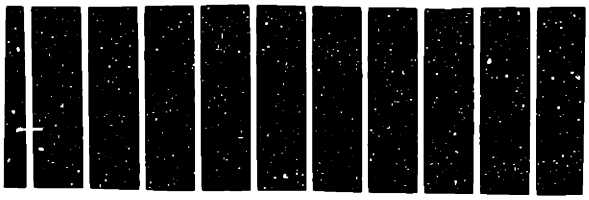

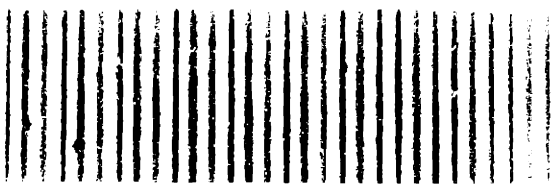

II, were directly applicable, along with a technique of accurately controlling the line-to-period ratio of the grating, discussed below. In addition, the gap between the "parent" grating and the recording film had to be accurately determined and maintained.

V-C-2 Fabrication Procedure to Produce the Parent Mask

The fabrication procedure to produce the gratings required for x-ray spatial period division was very similar to that already discussed in Chapter II. In that chapter, a procedure for making thick gold transmission diffraction gratings was presented. For the carbon-K x-ray, the gold thickness required is $\gtrsim$ 180 nm, and the transmissive region of the 199 nm period grating must be $\lesssim$ 50 nm wide. To meet the added requirement of narrow (50 nm) spaces, the original x-ray lithography mask was made with the required line-to-period ratio through a "shadowing" process developed by D.C. Flanders.[22] The detailed fabrication steps are given in Appendix F. This "shadowing" procedure began with holographic lithography exposures of 199 nm period grating patterns on (100) silicon wafers coated with 20 nm of Si_3N_4, 10 nm of Cr and 60 nm of photoresist. The holographic exposures were performed so that the grating lines were oriented parallel to the <110> direction. After resist exposures and development, the 10 nm layer of chromium was chemically etched in a solution of 164 grams of ceric ammonium nitrate, 43 ml of perchloric acid and sufficient water to produce a one liter volume of etchent.[72] The chromium was then used as a mask to etch the Si_3N_4 in a CHF_3 plasma in the reactive ion etcher.[21] The etch was stopped when the silicon was exposed in unmasked, monitor areas. Next, the samples were placed in a 30% solution of potassium hydroxide (KOH), satura-

ted with isopropyl alcohol. The KOH solution at 80°C is known to etch into the <111> crystallographic direction approximately 20 times slower than into either the <100> or the <110> direction.[73] This results in a crystallographically smooth "sawtooth" structure in the silicon surface, Figure V-2.[22] After the KOH etch, the Si_3N_4 was removed by a one-minute soak in buffered HF, and an approximately 2 μm thick layer of polyimide was spun onto the silicon "sawtooth" surface. After polyimide curing, the polyimide was bonded to a polyvinylchloride tube, and the silicon wafer was etched away. The polyimide was then bonded to an aluminum ring. Next, tungsten was obliquely evaporated onto this polyimide mold, Figure V-3. The angle at which the tungsten was evaporated determined the linewidth of the opaque regions of this membrane. Control over the grating period through holographic lithography to ±0.5 nm tolerances is relatively easy. Control over the line-to-period ratio of the grating through "shadowing" to ±5 nm has been demonstrated by D.C. Flanders.[22]

The x-ray lithography masks produced in this fashion have a low contrast, ∿ 3 dB. This is due to the angle of the polyimide sawtooth structure, which determines the maximum thickness of the absorber pattern, and hence, the maximum contrast. It was found that the replication of a 40 to 50 nm wide line with only 3 db contrast in the x-ray mask, could only be accomplished when the PMMA thickness was less than ∿ 150 nm. Since gold thicknesses in excess of 180 nm were desired, this mask was unsuitable. Through two successive x-ray exposures and lift-off processes, a mask with the correct polarity and sufficient contrast (∿ 8 dB) was fabricated. This new mask was used to expose the desired grating structure with ∿ 40 nm wide lines in 250 nm thick PMMA on a gold plating base. At this point, the gold

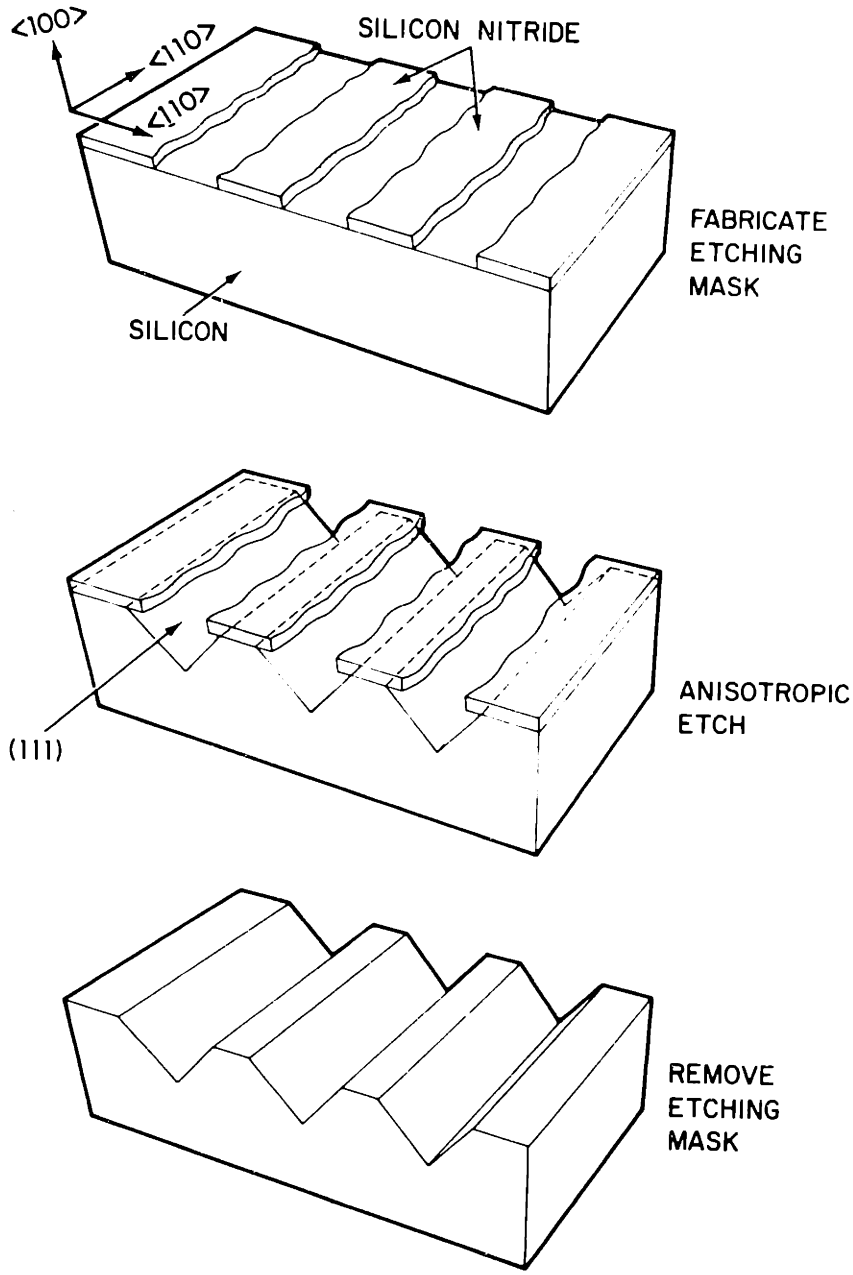

Figure V-2 Procedure to fabricate a sawtooth structure in silicon. A silicon nitride grating is defined with its grating lines parallel to the <110> direction in the silicon wafer. Potassium hydroxide is used to anisotropically etch the exposed silicon. Finally, the silicon nitride mask is removed in buffered hydrofluoric acid, and the silicon sawtooth structure is left (Reference 22).

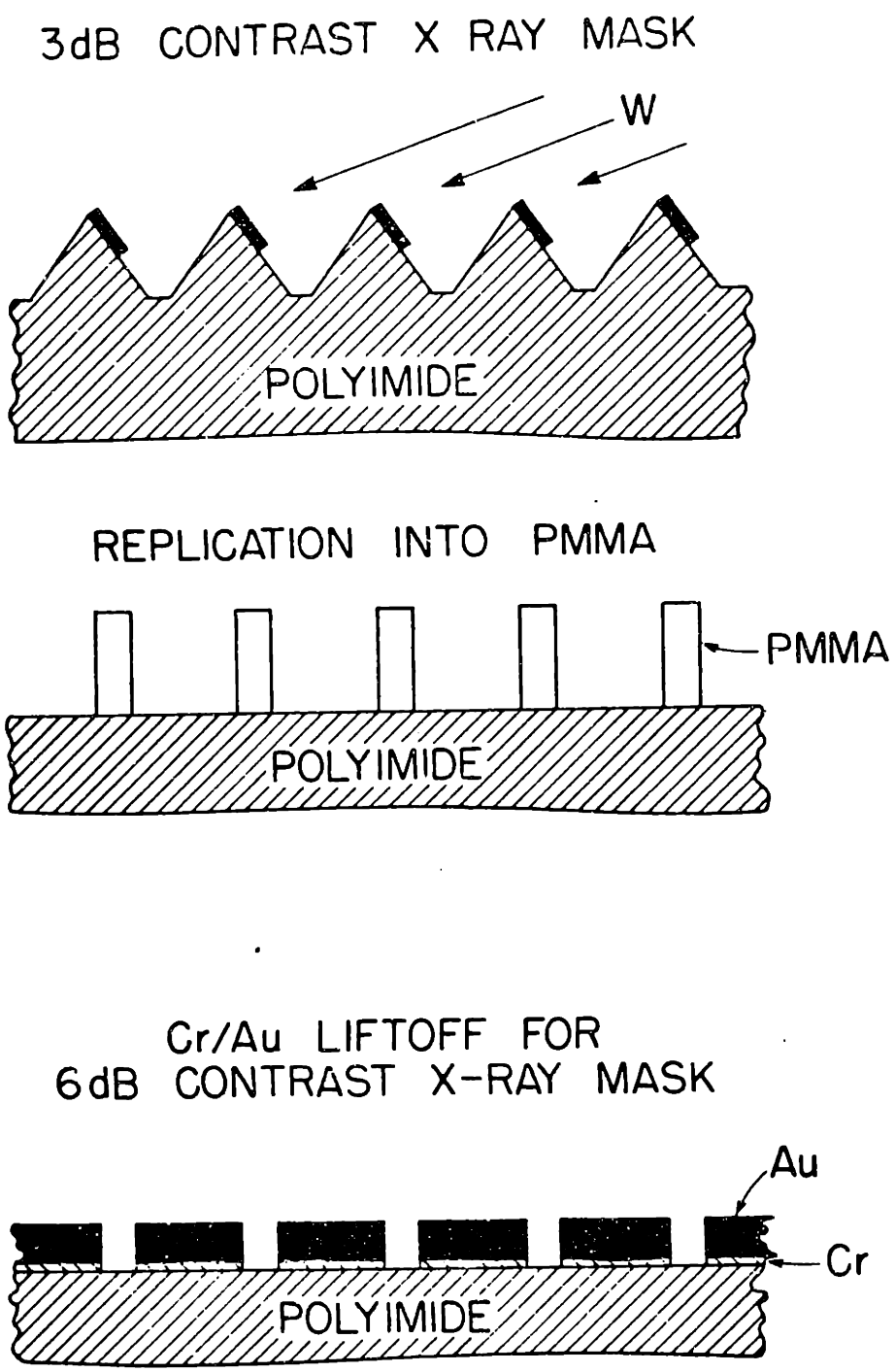

Figure V-3 A polyimide mold of the silicon sawtooth structure in Figure V-2 was "shadowed" at an oblique angle with tungsten to produce an x-ray lithography mask with a controlled line-to-period-ratio. Replication into PMMA is accomplished, and further processing can be done (such as a Cr/Au liftoff to produce a higher contrast x-ray lithography mask).

microplating, outlined in Chapter II, was performed to produce the desired structure. Figure V-4 is an SEM micrograph of a 199 nm spatial period gold grating with ∿ 40 nm wide spaces. This sample was plated to only 180 nm, and was therefore sacrificed for microscopy. The actual "doubling" experiments were performed with a mask plated to a thickness of approximately 250 nm.

V-C-3 Gap Control

To record the spatial period division image, the "parent" mask must be kept at the appropriate distance from the recording film. To "double" a 199 nm period grating with the C_K x-ray, a 4.4 ± ∿ 0.3 μm gap was required, according to section IV-F. One method of gap control would be to use a thin film membrane. A 4.4 μm thick polyimide membrane, with one of the lowest known attenuations at the C_K x-ray, would absorb ∿ 9 dB of the incident x-rays (Figure II-2), and would increase the exposure times by a factor of 8, which was unsatisfactory. Another method of gap control was required. The approach used was to spin a 4.4 μm layer of polyimide onto a silicon wafer, and then to etch 25 x 25 μm square holes, spaced 50 μm apart, into the film by RIE in O_2. After the 25 μm square grid pattern was produced, the polyimide film was mounted onto a ring and the silicon wafer was etched away, Figure V-5. The advantage of this method was to be able to maintain the proper gap with the polyimide membrane spacer, and to record the spatial period division image in the regions of no attenuation.

In addition to the fixed gap polyimide spacer, a variable (tapered) spacer was also fabricated. This was achieved by first fabricating a 4.8 μm thick polyimide film onto a silicon wafer, with the 25 x 25 μm grid pat-

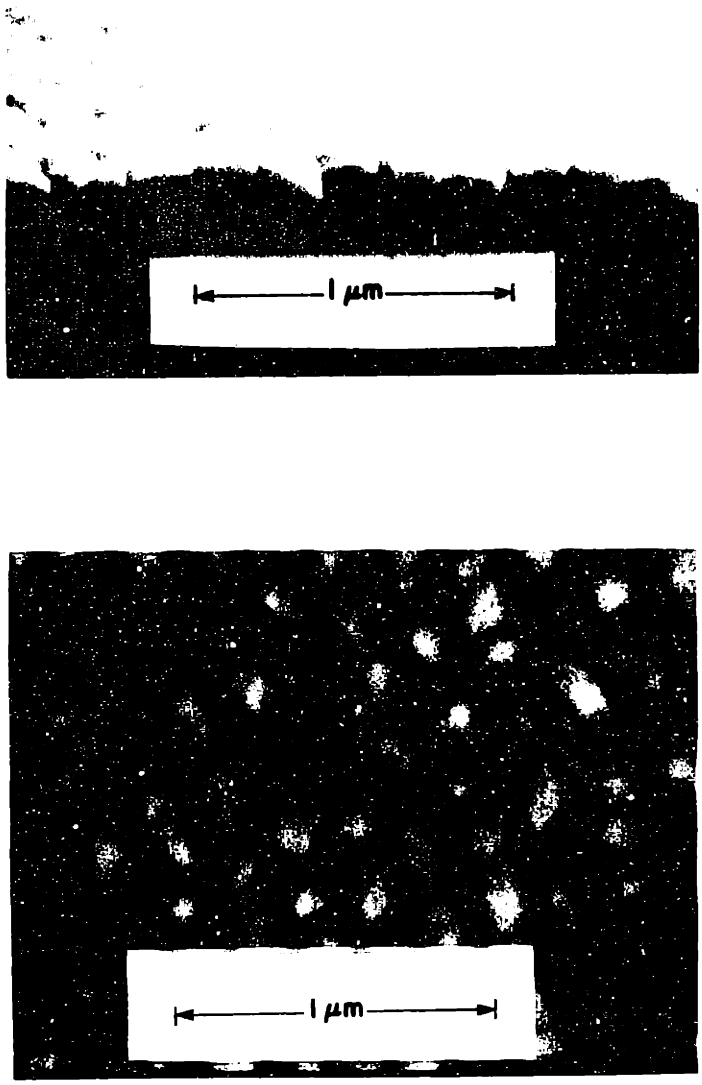

Figure V-4 SEM micrograph of a 199 nm period grating with 40 nm wide "slits" in 180 nm thick gold: top: cleaved edge view, bottom: top view.

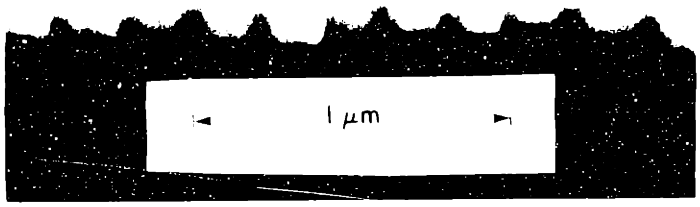
1 μm

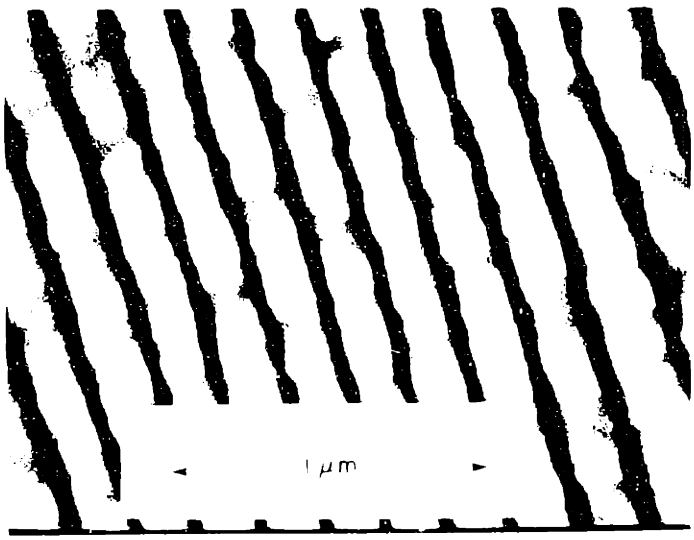
1 μm

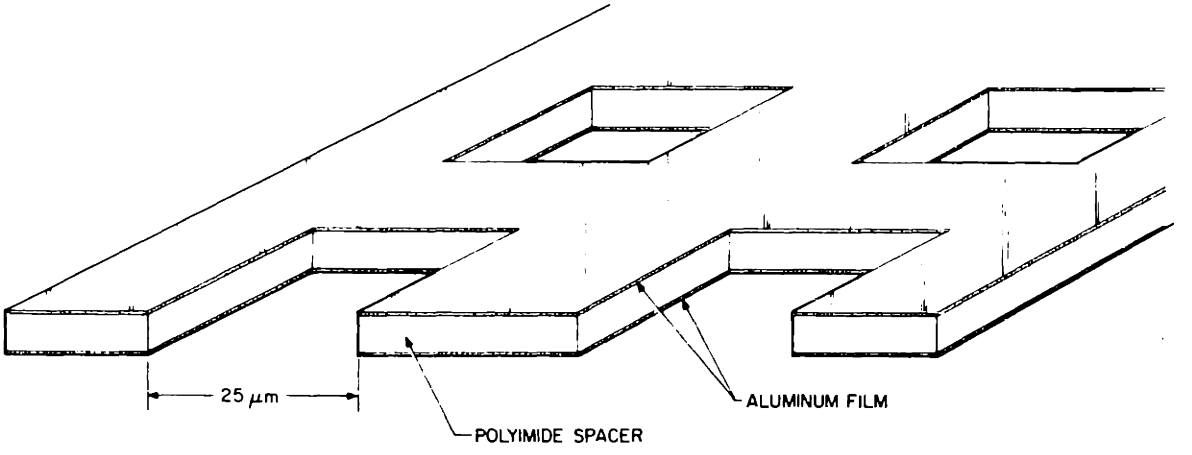

Figure V-5 Cross-sectional view of the polyimide spacer used for gap control.[28] A 25 x 25 μm hole pattern was etched into the ∿ 4 μm thick polyimide film. The aluminum film, shown above, was originally part of the electrostatic hold-down for mask-wafer contact. More recent experiments used a different arrangement which did not require the aluminum film.

tern of holes etched into the polyimide. The film was then stripped of all masking materials, and placed under a stationary aluminum block in an oxygen ion beam (500 eV, $\sim$ 0.5 mA/cm^2). The sample was removed from underneath the aluminum block at a rate of approximately 1 mm per minute. The final product was a polyimide film with a thickness monotonically increasing from 3.5 to 4.8 μm. The polyimide was then bonded to a ring, and the silicon etched away.

To maintain the proper mask-to-wafer gap, the polyimide spacer mentioned above was placed onto a PMMA coated silicon wafer. The spatial period division mask was then placed on top of the polyimide spacer, and the entire "sandwich" was clamped together electrostatically (see section II-D-3-d).

V-C-4 X-Ray Spatial Period Division Exposure and Results

For a spatial period division, it is necessary to have a source of radiation with sufficient collimation so that the penumbra will not degrade the image. The penumbra, δ, is defined as:

$$\delta = Sd/D$$

where S is the mask to wafer gap, d is the source diameter and D is the source-to-mask distance. To "double" a 200 nm period grating, it is necessary that the penumbra be less than a linewidth (δ < 50 nm). For S = 4.4 μm, it was required that d/D < 10^{-3} radians.

To maintain a d/D $\leq$ 10^{-3} radians, a 0.8 x 4 mm aperture was placed 6 mm above the x-ray source. This insured that an x-ray "line" source would result, which would limit the penumbra in one dimension (perpendicular to the grating lines), and any effects of electron-beam walking or spreading

on the anode would not increase the effective source size. Unfortunately, the aperture increased x-ray replication exposure times to ∿ 50 hours (normal replication exposures of 15-18 hours were required without the aperture), and x-ray "doubling" exposure times to ∿ 190 hours, indicating that the source is larger than 1 mm in diameter. The nominal doubling exposure should be twice the nominal replication exposure time. The additional increase in exposure time was due to additional absorption of the x-rays in the gold plating base (∿ 1.5 dB) and the additional absorption in a thicker polyimide membrane (∿ 2 μm) supporting the "parent" mask (additional ∿ 2 dB attenuation).

The "parent" mask was separated from the recording film of 150 nm thick PMMA by the polyimide spacer described in the last section. The "parent" mask was oriented so that the grating lines were parallel to the longer aperture dimension. The mask-spacer-sample sandwich was then clamped together electrostatically, Figure V-6. After a 190 hour exposure, the sample was developed for 5 minutes in 40% MIBK, and 60% isopropyl alcohol. The sample was cleaved, gold coated and observed in the SEM. A 99.5 nm period grating in 150 nm thick PMMA was then observed, Figure V-7, which clearly demonstrated the technique of x-ray spatial period division, and its ability to produce sub-100 nm period gratings. The dip, which extends about 20 nm deep into the top of each PMMA line, is a higher spatial frequency component. Under appropriate conditions, this dip is predicted from the near field diffraction pattern.

V-D DEEP U.V. SPATIAL PERIOD DIVISION

As a final example of the theory presented in Chapter IV, an experi-

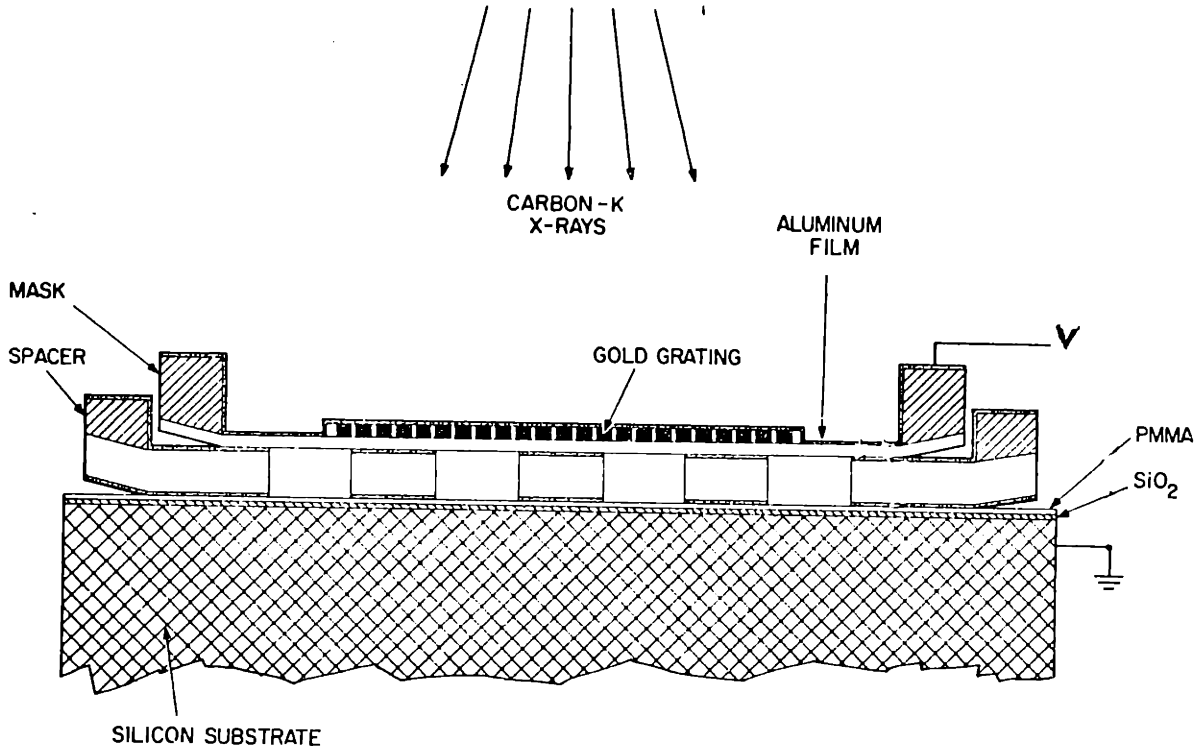

Figure V-6 Cross-sectional view of the spatial period division exposure. A thick gold grating was exposed to carbon-K x-rays. The grating to wafer gap was maintained by the polyimide spacer (Figure V-5), and the mask-spacer-wafer assembly was held together electrostatically.

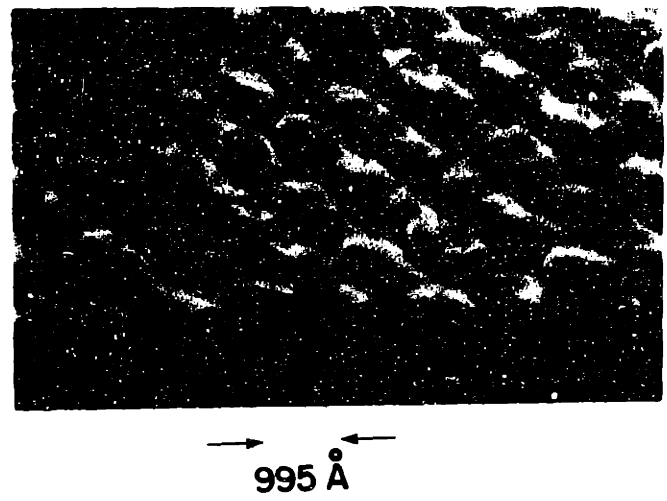

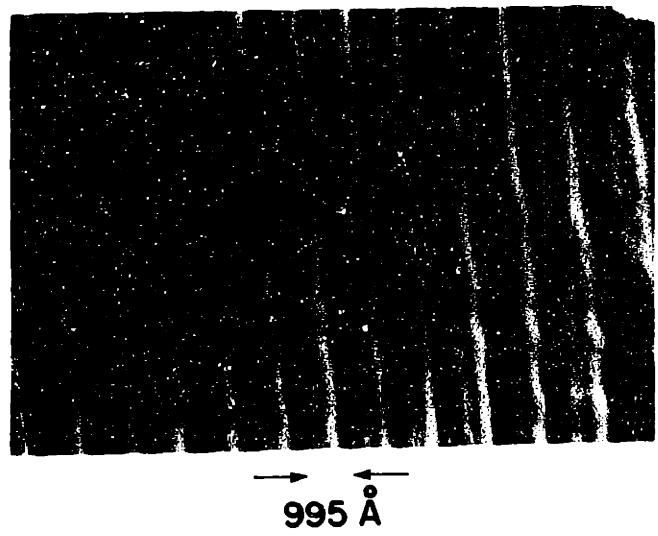

Figure V-7 SEM micrograph of the cleaved edge view and the top view of a 99.5 nm period grating exposed in 150 nm thick PMMA by x-ray spatial period division. The dip in each PMMA line, which extends about 20 nm, is a higher spatial frequency interference effect.

995 Å

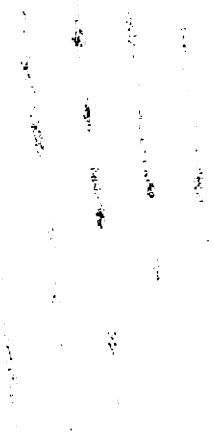

995 Å

ment was performed to "double" a 199 nm period grating with a deep U.V. source, such that only the zeroth and first order diffracted beams were present ($p > \lambda > p/2$). The theoretical analysis in section IV-E indicated that the near field diffraction pattern should have planes where the magnitude of the term corresponding to the fundamental grating period is either maximized or minimized. It was desired to record this oscillatory behavior, and to also observe the "doubled" image where the magnitude of the fundamental term is minimum.

The parent mask for this experiment was a 199 nm period grating, in 55 nm thick aluminum. This pattern was produced by a liftoff process with an x-ray lithographically exposed, 250 nm thick PMMA grating on a 1/16" thick, 1-1/2" diameter quartz disk. The measured attenuation in a 55 nm thick layer of aluminum at λ = 193 nm was $\gtrsim$ 20 dB, which corresponds to an "opaque" grating.

Thin (1-1/2 x 1-1/2 x 0.009") glass samples (Corning 0211 glass)[74] were coated with a 40 to 50 nm thick layer of PMMA. The sample was then clamped to the aluminum grating on the quartz disk, and pressed into contact at one location with a probe. The separation between the mask and wafer increased as a function of distance from the probe location. A measurement of this separation was made by recording the location of the interference fringes produced by visible light as a function of the gap between the two surfaces in near contact, Figure V-8. Each fringe corresponds to an increase in gap of approximately 300 nm (one-half a visible light wavelength).

To expose the "doubled" image of the grating, a pulsed ArF laser (λ = 193 nm) was used. The beam of the ArF laser was expanded so that a nearly

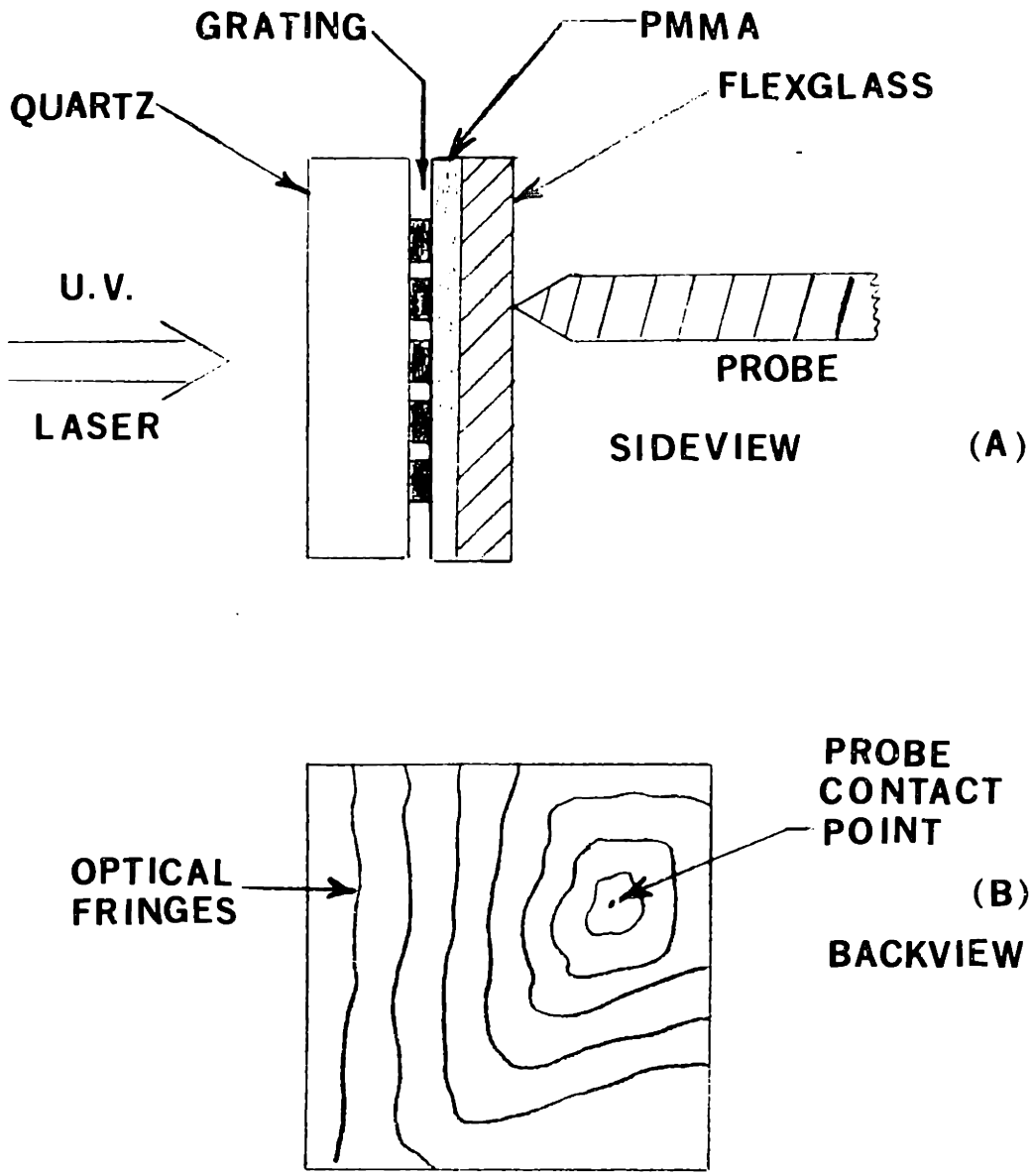

Figure V-8 U.V. spatial period division experiment. (A) Sideview: a 199 nm aluminum grating (on a quartz disk) was illuminated by a U.V. laser. A probe held the grating in intimate contact with 50 nm thick PMMA, spun onto Corning 0211 glass ("Flexglass"). (B) Backview: optical fringes, which were easily seen, indicated the variation in gap as a function of distance.

uniform beam illuminated the one centimeter square area of the grating, through the quartz disk. The total output energy of the laser was approximately 3 mj/pulse, and approximately 15,000 pulses (at a repetition rate of 10 pulses per second). The power density after expansion was not measured, but from data on x-ray exposure,[24] about 1000 J/cm^3 should be required to fully expose PMMA. After a 2 minute development in 40% MIBK, and 60% isopropyl alcohol, the presence of a grating was detected by looking for diffraction effects. By placing the sample in a beaker of water, and illuminating it with a white light source, bands of diffraction corresponding to a grating with period of 199 nm (the "fundamental") were observed. Next, the sample was illuminated by the ArF laser at near grazing incidence, and again, bands of diffraction corresponding to a grating of peroid 99.5 nm were observed on a fluorescent card. The sample was then cleaved, gold coated and observed in the SEM. The micrographs shown in Figure V-9 clearly illustrate that the pattern recorded in the PMMA varied as the gap between mask and substrate changed, and also reveal that, at the correct gap, the pattern recorded has a spatial period of 99.5 nm. The spatial period of the recorded pattern changed from fundamental grating period (199 nm) to half the fundamental grating period (99.5 nm) and back again with approximately 2.5 ±0.5 full cycles of oscillation with a change in gap corresponding to one optical fringe (a gap variation of $\sim$ 300 nm).

From equation 4-31 it was expected that one full cycle of oscillation would occur when the distance, Λ, varied by:

$$\Lambda = \pi/(k-k_z)$$

where $k = 2\pi/\lambda$ and $k_z = ((k^2 - 2\pi/p)^2)^{1/2}$.

For the conditions of this experiment, Λ would be $\sim$ 130 nm, which agrees reasonably well with the experimental observation of $\sim$ 120 ±20 nm.

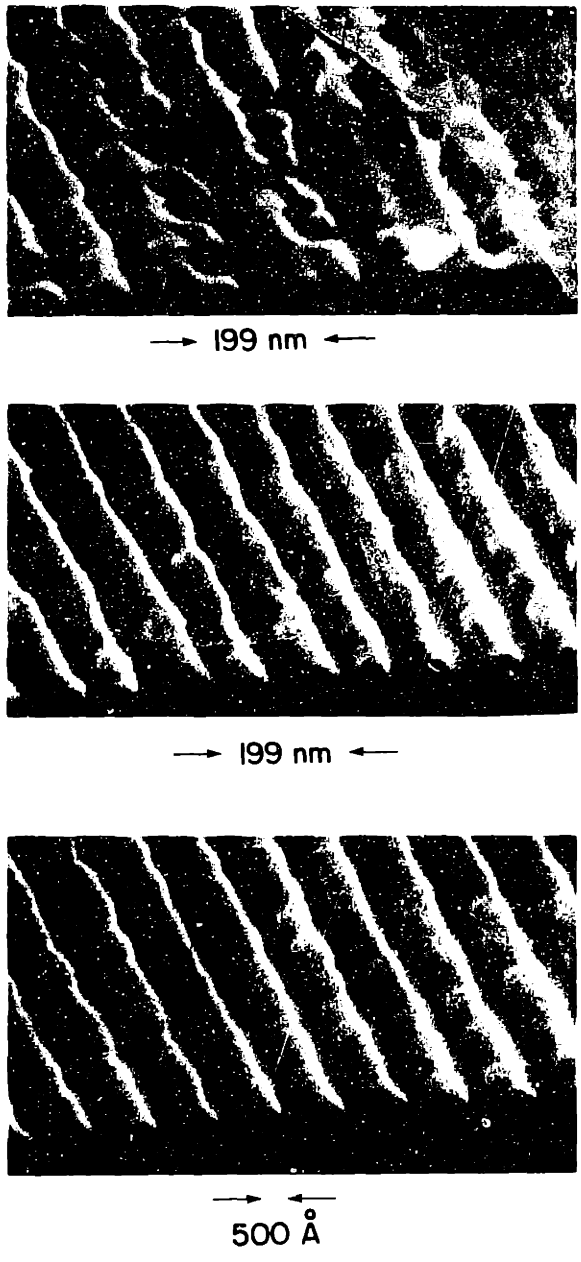

Figure V-9 SEM micrograph of the cleaved edge view as a function of distance, for a sample exposed in the U.V. spatial period division experiment. In the top micrograph, a 199 nm period modulation in 50 nm thick PMMA is seen. As the gap is changed, the PMMA lines begin to split (center micrograph), until a 99.5 nm period grating is observed (bottom micrograph).

199 nm

199 nm

500 Å

CHAPTER VI

SUMMARY AND FUTURE WORK

Thick gold, transmission diffraction gratings have been produced by a multistep process involving holographic lithography, ion etching, x-ray lithography and gold microplating. This process permitted the fabrication of thick gold gratings with submicron periodicities and high aspect ratios. The gratings were used as the diffractive element in a spectrometer, and were also coupled to an x-ray microscope and a streak camera to simultaneously produce spatial and spectral, and temporal and spectral information of x-ray sources. Measurements of the efficiency and resolving power of the gratings were also made.

The near field diffraction pattern of a transmission diffraction grating was calculated by using the angular spectrum of plane waves approximation. Numerical calculations of the intensity pattern as a function of transmission and phase shift through the grating lines, line-to-period ratio of the grating, and the distance from the grating were presented. The calculations were used to optimize the parameters necessary to record a spatial period division image. Spatial period division was demonstrated by the exposure of sub-100 nm period gratings using soft x-ray radiation, and deep U.V. radiation.

Further experimental work can have major impacts on several fronts. Thicker gold diffraction gratings with smaller periods than those reported here will enable the spectroscopic investigation of more energetic sources.[60] Thicker gold gratings may be fabricated by several techniques, including the one outlined in section II-G. The simplicity and versatility

of these gratings allow them to be coupled with a variety of x-ray diagnostic instruments, only a few of which have been mentioned in this dissertation. The techniques of producing very thick gold gratings can also be adopted to produce thick (> 1 μm) Fresnel zone plates[63,75] with minimum linewidths of the order 0.1 μm. Spatial period division can also be used to produce gold gratings with finer spatial periods, perhaps as small as 40 nm, and also to "double" a Fresnel zone plate.[9] Lastly, refinements in the technique of spatial period division may be possible which would release the requirement of thick gold for the grating lines.

More detailed calculations on the near field diffraction pattern of thick gold gratings need also be considered. Specifically, under the condition that:

$$\lambda \sim \frac{p^2}{2t_g}$$

where λ is the wavelength of the incident radiation, p is the grating period and t_g is the thickness of the gold grating lines, the simple calculations used here are no longer valid. It is possible that coupling between diffracted orders will occur which will severely alter the amplitude of the various orders.

Much work has been done in the past few years on the fabrication of x-ray optical components, and a grating is only one such component. Various groups are working on x-ray Fresnel zone plates,[76,77] and other groups are working on reflecting mirrors for soft x-rays.[78,79] Current fabrication technology is quickly approaching the regime where accurate control over distances comparable to a soft x-ray wavelength is feasible, and the capability of producing high quality diffractive optics with minimal dis-

tortions has now been achieved. With this capability, and with the techniques discussed in this dissertation, it is clear that the door to new frontiers has been opened. Using these optical components for spectroscopic information, as I have done, is just the first step to fully utilize these x-ray optical components. New x-ray diagnostic optical components, such as interferometers or other tools, can be contemplated with the advent of these submicron fabrication techniques.

APPENDIX A

PREPARATION AND SPINNING OF PMMA

The PMMA used in this work was obtained from the Esschem Corporation[60] and had an average molecular weight of ∿ 950,000. The procedure for the preparation and spinning of PMMA closely follows the procedure given in reference 30. First, 10 grams of PMMA were "leached" in a one-liter solution of develcper (60% isopropyl alcohol, 40% MIBK) and stirred for 16 hours to insure that the solid which remained had a minimum solubility in the developer. After stirring, the PMMA was separated from the developer by vacuum filtration through a fritted glass filter. Any remaining solvent was evaporated by placing the "leached" PMMA into an 80°C oven for 12 hours. The PMMA prepared in this manner can be stored indefinitely.

To coat samples, the PMMA was dissolved in an appropriate solvent, such as chlorobenzene. Solutions of 2, 4, 6, 8 and 10% PMMA by weight were prepared. For spin coating samples, the solution was passed through a sintered-silver[81] filter (0.2 μm filter size) to remove any suspended particles. Chlorobenzene is a toxic chemical, and a vented spinner must be used. In addition, a moderate air velocity normal to the spinning sample surface was necessary to prevent PMMA "cobwebs". A spin time of 60 seconds and a variety of spin seeds were used to achieve thicknesses ranging from a few tens of nanometers, to over one micron with the different percentage solutions, Figure A-1. After spinning, the PMMA film is baked at 180°C in flowing nitrogen for 30 minutes.

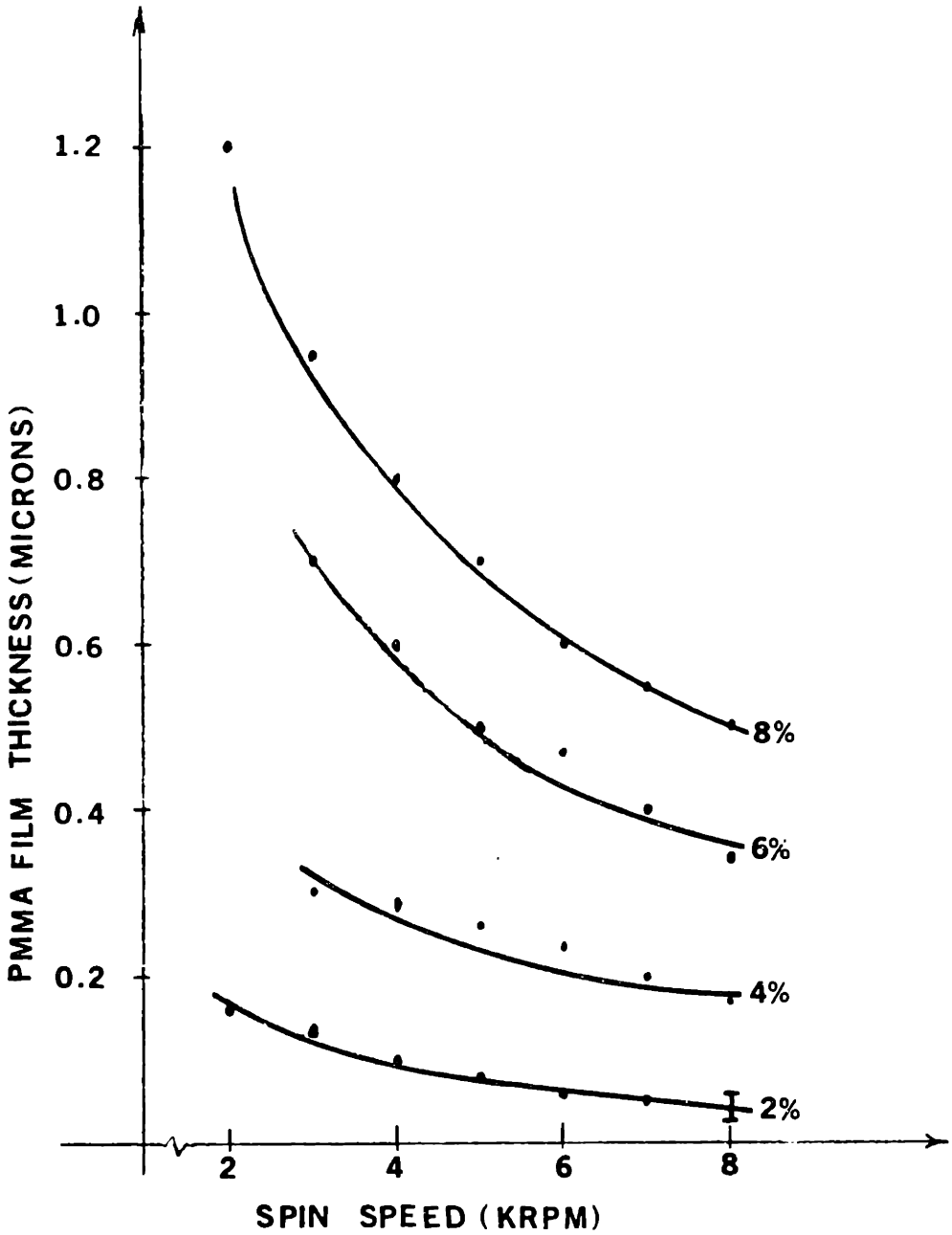

Figure A-1 PMMA thickness versus spin speed for various percentage solutions of PMMA in chlorobenzene.

APPENDIX B

PREPARATION AND SPINNING OF POLYIMIDE

The procedures described below closely follow those described by D.C. Flanders.[30] The polyimide used in this work was obtained from the duPont Company,[82] as PI-2530, and is a solution of polyamic acid in N-methyl-2-pyrollidone and cellusolve, which upon heating polymerizes into polyimide. Polyamic acid is very hydroscopic, and any water in the solution will degrade the resulting polyimide film. It is therefore very important to keep the PI-2530 away from water, in dry beakers, and not open to humid air. When preparing the solutions of PI-2530, it is often diluted with N-methyl-2-pyrollidone and acetone to obtain a thinner film of polyimide. Because acetone can absorb water when exposed to humid air, a fresh (unopened) bottle of acetone must be used. Lastly, PI-2530 has a limited shelf life at room temperature, and must be stored at temperatures below $\sim$ 5°C.

When spinning a polyimide film onto samples, it is necessary to thoroughly clean the samples first. The final step in a standard cleaning procedure is to immerse the samples into high purity ($\sim$ 18 Mohm-cm) water for 30 minutes. Prior to spinning, the samples must be thoroughly dried, and this can be done by blowing excess water off in a nitrogen jet, and then baking them in a clean, vented oven at approximately 120°C for 10 minutes.

The polyimide solution is pushed through a sintered-silver filter[81] (0.2 μm) at room temperature. Cold solutions of polyimide are very viscous, and are difficult to force through the filter. The PI-2530 solution has been diluted into a 4:1:1 mixture and a 4:3:3 mixture of PI-2530:N-

methyl-2-pyrollidone:Acetone. By varying the spin speed from 3-10 KRPM, film thickness of approximately 2.4 to 1.4 μm can be obtained from the 4:1:1 mixture (Figure B-1) and a thin, 0.5 μm film can be obtained with the 4:3:3 mixture at 10 KRPM. After spinning on a vented spinner, the film is cured in a three-temperature bake:

(a) 150°C for 30 minutes in flowing N_2;

(b) 250°C for 60 minutes in flowing N_2;

(c) 310°C for 2 hours in vacuum.

After curing, the samples can be stored indefinitely.

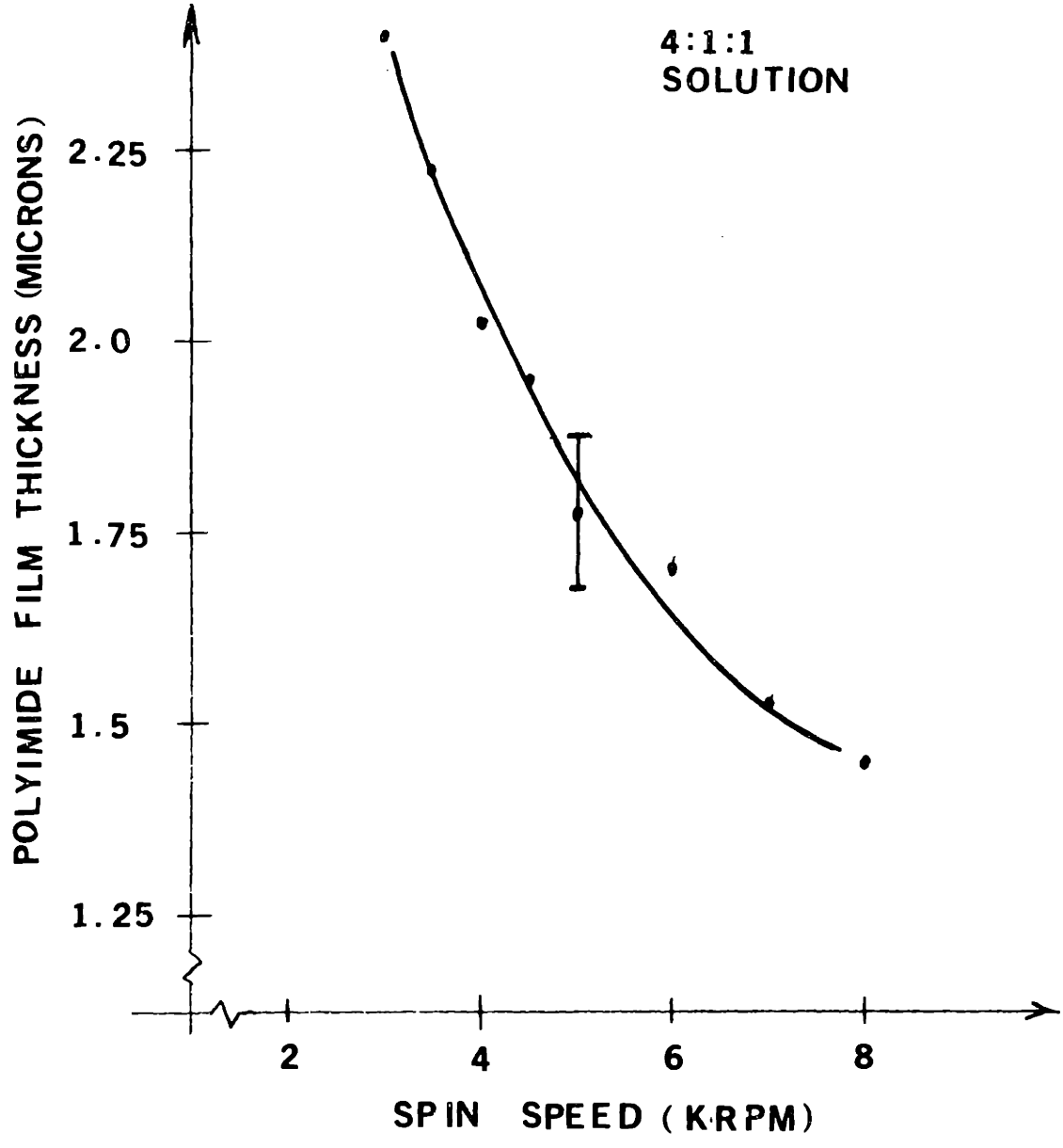

Figure B-1 Polyimide film thickness versus spin speed for a 4:1:1 solution of polyimide.

APPENDIX C

FABRICATION PROCEDURE TO PRODUCE X-RAY MASKS

The procedure for making x-ray lithography masks on a polyimide membrane closely follows that described by D.C. Flanders,[30] with some modification. To define a gold absorber pattern on a polyimide film suitable for an x-ray lithography mask, several patterning techniques are possible. The simplest process for making a grating mask included holographic lithography and ion etching. The sequence of fabrication steps was as follows:

(1) A 1.0 to 1.5 μm thick film of polyimide is spun onto a 2-inch diameter silicon wafer, using the procedure outlined in Appendix B.

(2) Approximately 10 nm of polyimide is etched in an oxygen plasma asher (∿ 30 sec at 250 W) to insure a clean surface for good adhesion between the polyimide and the chrome-gold layer, step (3).

(3) Immediately following the plasma ashing, 10 nm of chrome, followed by ∿ 70 nm of gold are electron-beam evaporated onto the polyimide in a high vacuum (∿ 2×10^{-7} torr) chamber.

(4) The sample is spin-coated with ∿ 60 nm thickness of AZ 1350 J resist, diluted with AZ thinner (2:7 ratio) and baked at 80°C for 20 minutes.

(5) The samples are holographically exposed and then developed in a solution of one part AZ developer and one part water for 15 seconds.

(6) A monitor area near the grating is formed by removing the unexposed resist with a cotton-tipped swab, soaked with acetone. Caution must be exercised at this point to prevent destruction of the exposed grating.

(7) The samples are ion-beamed etched in a neutralized 500 eV argon ion beam. Etching is terminated when all the gold in the monitor area is removed. Approximately one minute of etching time is required for a 0.5 mA/cm^2 current density. Etching was done in a 10-second etch, 30-second cool-down cycle to prevent overheating of the resist.

(8) The remaining resist is removed by spraying the sample with acetone. If this does not fully remove the resist, plasma ashing the sample for two minutes in an oxygen plasma (plasma asher) is used.

(9) The sample is bonded with five-minute epoxy to a polyvinylchloride tube 1-3/4" outside diameter, 1-1/2" inside diameter.

(10) All exposed epoxy and all silicon areas not to be etched are masked by a layer of black wax.

(11) The silicon is etched in a 97% HF, 3% HNO_3 solution at room temperature. A 10-mil thick silicon wafer etches completely in approximately 20 minutes.

(12) After silicon etching, the sample is rinsed in DI water, then in isopropyl alcohol. The polyimide is then dried by blowing it with a nitrogen jet.

(13) A 1" O.D., 3/4" I.D., 1/16" thick aluminum ring (with a 5° taper, see Figure II-16) is bonded to the polyimide membrane with a low viscosity, 24 hour curing epoxy (BI-PAX, Trabond, BA-2115).[83]

(14) The aluminum ring is removed from the excess membrane outside the ring by cutting through the membrane with a knife.

(15) For the electrical hold-down procedure, a 40 nm thick layer of aluminum is evaporated onto the membrane. Electrical continuity to the aluminum ring is accomplished by scratching through the polyimide

to the aluminum ring, allowing the evaporated aluminum to make contact to the ring. Several scratches are necessary to get reliable contact.

To produce an x-ray lithography mask through a liftoff process requires a slightly different procedure. A sample is prepared with a polyimide film as in steps (1) and (2) above. Then:

(3a) Spin 4% PMMA at 5 KRPM to obtain a $\sim$ 0.25 μm thick film.

(4a) Use x-ray lithography to expose a grating into the PMMA with an existing mask. Develop until the monitor area is fully developed.

(5a) Remove any organic contaminant by placing the sample in the plasma asher at 250 W for 5 seconds.

(6a) Evaporate 5 nm Cr, 60 nm Au for liftoff.

(7a) Soak sample in chlorobenzene with ultrasonic agitation.

Steps (9-15) are then followed as before. To expose PMMA on a conducting surface, such as a plating base, a Vespel, or some other insulating ring is used instead of an aluminum ring, and aluminum is evaporated onto the "back" surface of the membrane, instead of the "front" surface. To provide continuity between the aluminum film on the membrane and the aluminum on top of the insulating ring, the evaporation is done at roughly 45° relative to the vertical, and approximately 70 nm of aluminum is deposited.

APPENDIX D

FABRICATION PROCEDURE TO PRODUCE THICK GOLD GRATINGS

The thick gold grating fabrication procedure can be summarized as follows:

(1) Spin 0.5 μm of polyimide onto silicon wafers.

(2) Etch ∿ 10 nm of polyimide in an oxygen plasma asher (∿ 30 seconds at 250 W) to promote metal film adhesion.

(3) Immediately following the plasma ashing, 10 nm of Cr and 10-15 nm of Au are electron beam evaporated onto the polyimide coated samples in a high vacuum chamber (∿ 2×10^{-7} torr).

(4) The samples are spin-coated with ∿ 0.7 to 1.0 μm PMMA using a 6-8% PMMA solution, and baked at 180°C. (A 0.25 μm thick PMMA layer is used for the spatial period division work.)

(5) X-ray lithography is used to expose a grating pattern into the PMMA. The appropriate mask produced by liftoff must be used, as explained in section II-D-3-d. The samples are developed until the monitor areas are clear of all residual resist.

(6) The samples are then plasma-ashed in oxygen for 5 seconds (at 250 W) to remove any organic contamination.

(7) Sel-Rex[50] BDT-510 plating solution is used to microplate gold between resist lines. A bath temperature of 45°C (±3°C) and a pH of 8 (±0.5) is used. A driving voltage of 0.7 volts produces a plating rate of ∿ 10-15 nm/min, with an anode-to-cathode spacing of ∿ 2.5 cm.

(8) The PMMA is removed by soaking the sample in chlorobenzene for 10 minutes, and placing the sample into the plasma asher for 1 minute at 250 Watts.

(9) The plated wafer is bonded to a polyvinylchloride tube and black wax is used to mask all areas that are not to be etched. A circular pattern behind the grating area is etched in a solution of 97% HF, 3% HNO_3 acids, to obtain the gold transmission grating on a silicon support ring. In addition, an annular pattern ($\sim$ 2.5 cm inside diameter) is also etched, so that the silicon support ring can later be removed from the polyvinylchloride tube.

(10) After silicon etching (which takes approximately 20 minutes), the sample is rinsed in flowing DI water, followed by isopropyl alcohol, and subsequently dried in a nitrogen jet.

(11) The silicon ring with the grating pattern is removed from the tube by cutting through the polyimide in the annular pattern with a knife.

APPENDIX E

DISTORTIONS IN HOLOGRAPHICALLY PRODUCED GRATINGS

The issue of distortion in gratings exposed by holographic lithography has been discussed by Schmahl and Rudolf.[19,84] If two-plane waves interfere to expose a grating, a perfectly linearly grating, free of distortion, results. However, if the two interfering beams are spherical waves, the resulting grating is a family of hyperbolas.[84] Schmahl and Rudolph provided a complete description of the geometry of such a pattern, and from this, one can calculate the deviation from a linear grating. In this thesis, two spherical waves were interfered to produce the grating pattern (see Figure II-5), and there was concern about whether the resulting distortion would represent a problem when the gratings were used for x-ray spectroscopy. H.I. Smith provided the folowing simple calculation of the worst case distortion in gratings exposed by holographic lithography with spherical wavefronts.

Figure E-1 depicts a family of hyperbolas exposed through holographic lithography. The deviations from a linear grating are, of course, greatly exaggerated. Figure E-2 gives a top view of the holographic exposure system. We wish to calculate the distortion between points 1 and 2, where "distortion" is defined as the fractional change in recorded period, $\frac{p_2-p_1}{p_1} = \frac{\Delta p}{p}$, when source points F_1 and F_2 and points 1 and 2 are all in the same plane (plane of the holographic system).

To calculate the increase in grating period along the recording plane, the two point sources of wavelength λ are assumed to be separated by a distance 2W, and the recording plane is located a distance b from a line

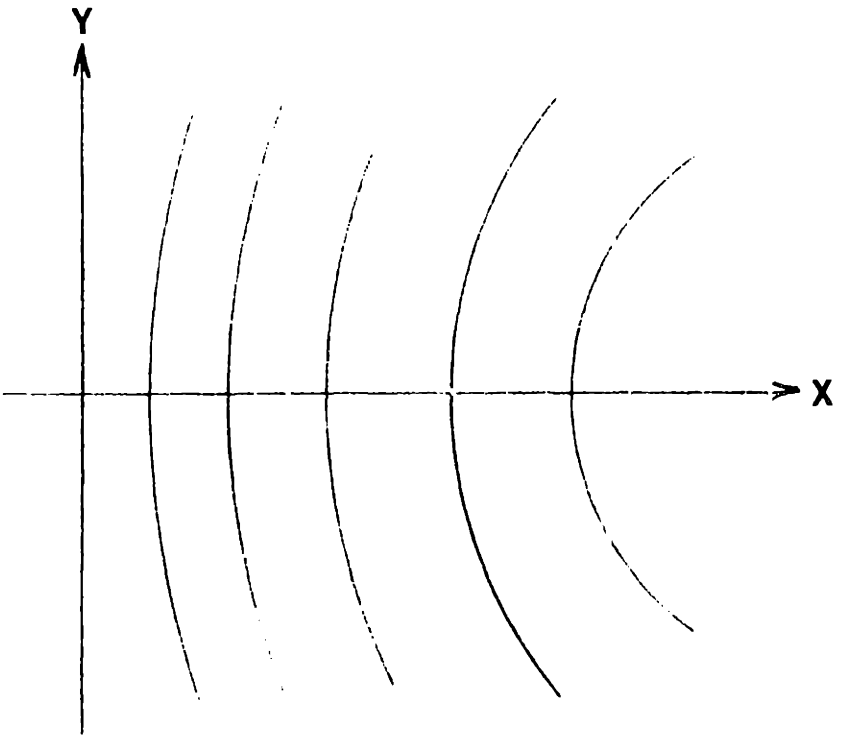

Figure E-1 Pattern of grating lines produced by interfacing two spherical beams is a family of hyperbolas. The period increases as a function of distance from the center of the pattern. The distortion as depicted above is greatly exaggerated.

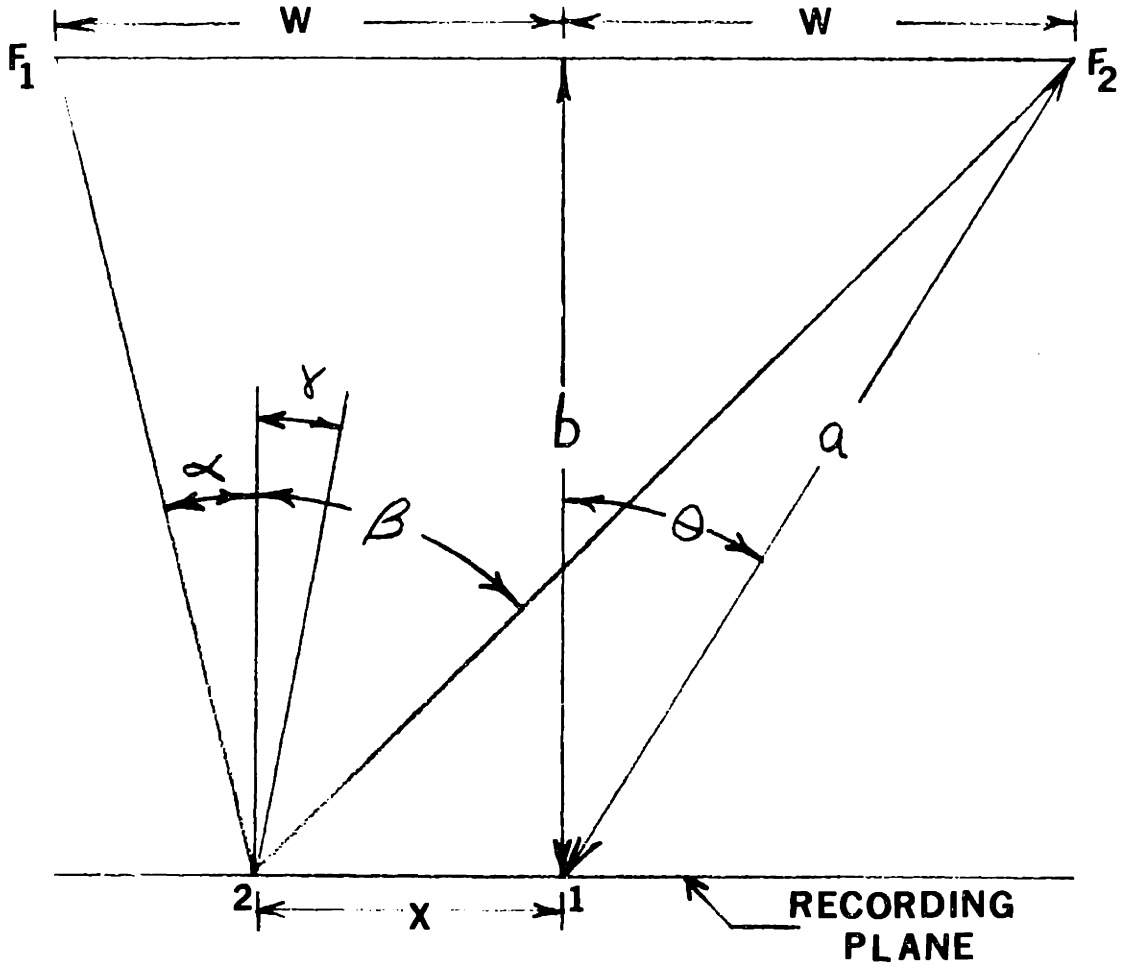

Figure E-2 F_1 and F_2 are two point sources, spaced 2W apart. The period of the exposed grating, both on axis and a distance "X" from the center (point 2), is calculated.

connecting the two sources, as shown in Figure E-2. The period of the grating on center (point 1) is simply:

$$p_1 = \frac{\lambda}{2 \sin \theta}$$

and the period of the interference pattern recorded at point 2 (located at distance X from point 1) is:

$$p_2 = \frac{\lambda}{2 \sin(\frac{\alpha+\beta}{2}) \cos \gamma}$$

where $\gamma = \frac{\alpha+\beta}{2} - \alpha = \frac{\beta-\alpha}{2}$

and α and β are defined in Figure E-2. The distortion in the grating is therefore:

$$\frac{\Delta p}{p} = \frac{\mathrm{Sin}(\theta) - \mathrm{Sin}(\frac{\alpha+\beta}{2}) \mathrm{Cos}(\gamma)}{\mathrm{Sin}(\frac{\alpha+\beta}{2}) \mathrm{Cos}(\gamma)}$$

For the 300 nm period gratings exposed with the helium-cadmium laser, a typical value for "a" in Figure E-2 was 50 cm. For the spectroscopic work reported in this dissertation, X = .015 cm, which results in a distortion, $\Delta p/p, < 1 \times 10^{-7}$.

To estimate the distortion out of the plane of the holographic system is more complicated, and has been treated by Schmahl and Rudolf.[19,84] A worst case estimate of the distortion can be calculated rather easily by putting the two sources in the plane of the recording plane, as depicted by the frontal view in Figure E-3. This has the effect of maximizing the curvature of the grating lines, and subsequently, the distortion in the grating.

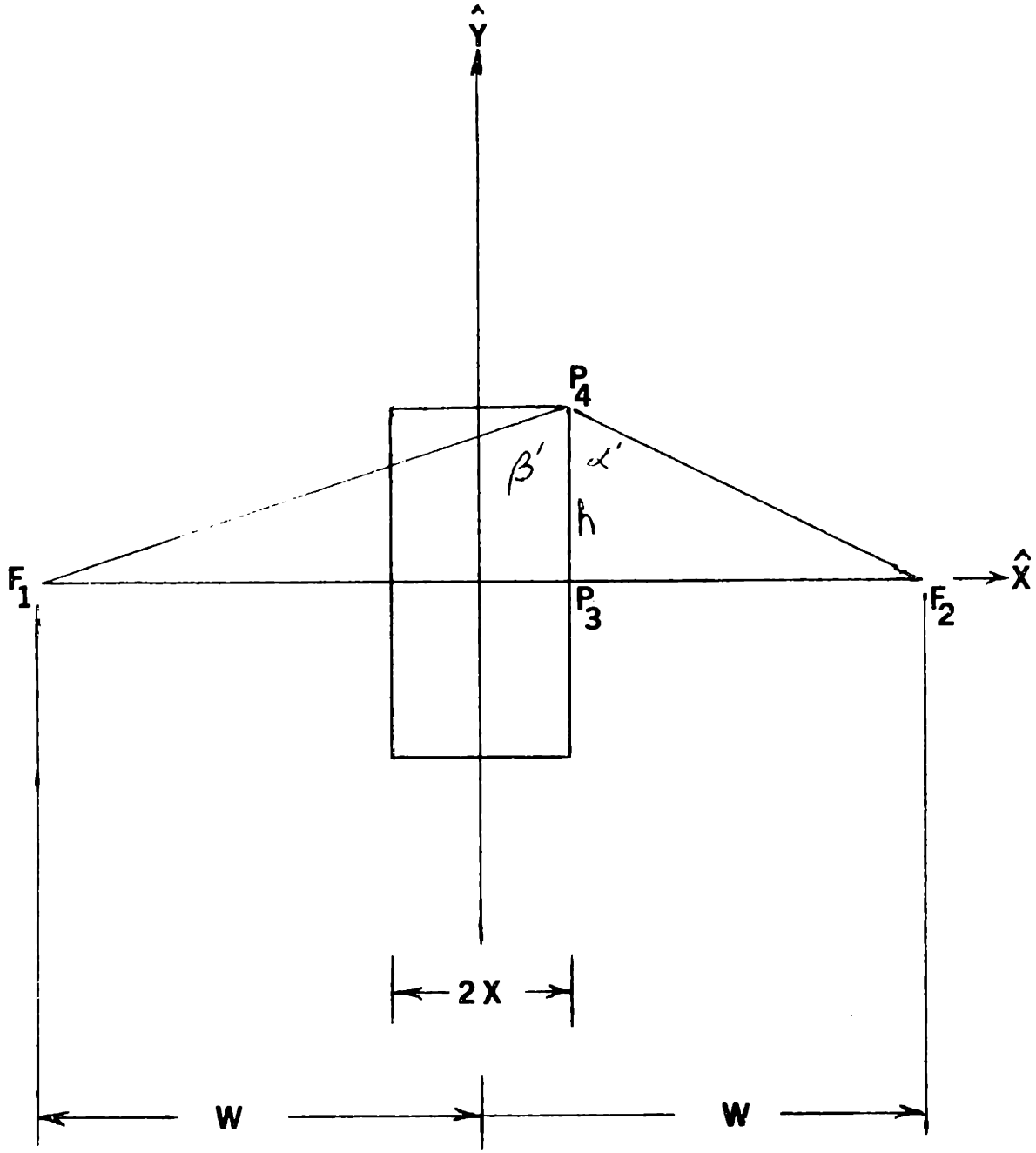

Figure E-3 Two point sources are in the plane of the grating to produce the maximum curvature in the grating lines. The grating period at points P_3 and P_4 are calculated.

The two point sources, F_1 and F_2, are placed 2W apart. At point P_4, the grating period, p_4, is:

$$p_4 = \frac{\lambda}{2 \sin\left(\frac{\alpha' + \beta'}{2}\right) \cos\left(\frac{\beta' - \alpha'}{2}\right)}$$

whereas at point P_3, the grating period, p_3, is:

$$p_3 = \frac{\lambda}{2}$$

The distortion in the grating is therefore:

$$\frac{\Delta p}{p} = \frac{1}{\sin\left(\frac{\alpha' + \beta'}{2}\right) \cos\left(\frac{\beta' - \alpha'}{2}\right)} - 1$$

For W = 50 cm, h = 0.35 cm, and x = 0.015 cm, the distortion is:

$$\frac{\Delta p}{p} \sim 2.5 \times 10^{-5}$$

As mentioned earlier, this is a worst case estimate of the distortion, and is only this bad at the corners of the grating area. In practice, the average distortion is less, and it can be easily stated that the distortion in the holographically produced gratings is expected to be $< 1 \times 10^{-4}$.

APPENDIX F

FABRICATION PROCEDURE TO PRODUCE A "PARENT" X-RAY MASK FOR SPATIAL PERIOD DIVISION

The following is a summary of the fabrication procedure that was used in this dissertation to produce a "parent" x-ray mask, which was suitable for spatial period division:

(1) clean 2-inch diameter, (100) silicon wafers;

(2) deposit onto the silicon wafers 20 nm of Si_3N_4 by chemical vapor deposition;

(3) deposit onto the Si_3N_4 ∿ 15 nm of chromium by electron beam evaporation;

(4) spin ∿ 60 nm of photoresist onto the sample;

(5) holographically expose a 199 nm period grating, with the grating lines oriented parallel to the silicon <110> direction;

(6) develop the photoresist in appropriate developer;

(7) use a wet chemical etch (ceric ammonium nitrate, perchloric acid and water)[72] to transfer the grating pattern into the 15 nm layer of chrome;

(8) strip off remaining resist in acetone;

(9) using the chromium as a mask, etch the 20 nm layer of Si_3N_4 in the reactive ion etcher, using CHF_3 as the gas. Continue etching until the Si_3N_4 is etched away in the monitor regions;

(10) strip remaining chromium in wet chemical etch;

(11) using the Si_3N_4 as a mask, anisotropically etch the exposed silicon in a 30% solution of KOH, saturated with isopropyl alcohol.

This will produce a "sawtooth"-type structure in the grating area in the silicon. Care must be taken not to over etch, as this will destroy the sawtooth structure.

(12) strip the remaining Si_3N_4 in a buffered HF solution. Check to see that all the Si_3N_4 is removed;

(13) re-clean the silicon wafers to remove any contamination;

(14) spin ∿ 1.5 μm of polyimide onto the silicon sawtooth structure, and cure it, as described in Appendix B;

(15) bond the polyimide to a 1-3/4" I.D., 2" O.D. polyvinylchloride tube with 5-minute epoxy;

(16) mask the epoxy and the "back" side of the silicon outside the grating area, with black wax;

(17) etch the silicon wafer in a solution of 97% HF, 3% HNO_3;

(18) bond the exposed polyimide membrane to a 1" O.D., 3/4" I.D. aluminum ring, with Bi-Pax TRA-BOND[83] BA-2115 epoxy. (Low viscosity epoxy - curing time ∿ 24 hours.);

(19) remove aluminum ring from the rest of the membrane by cutting through the polyimide outside of the ring;

(20) evaporate at an oblique angle ∿ 25 nm of tungsten so as to deposit the tungsten onto the tips of the sawtooth structure in the polyimide. The angle of deposition will determine the width of the x-ray absorptive region.

(21) evaporate ∿ 40 nm of aluminum onto the front surface of the mask, being certain to obtain electrical continuity between the aluminum ring and the evaporated aluminum layer;

(22) replicate into ∿ 150 nm PMMA on ∿ 1.5 μm polyimide on a silicon wafer;

(23) using the liftoff procedure for fabricating x-ray masks (Appendix C), liftoff 5 nm of Cr/60 nm of Au. Fabricate this into an x-ray mask, following Appendix C, to produce a high contrast x-ray mask with narrow spaces and broad lines;

(24) replicate this mask, as in step (22);

(25) using Appendix C, liftoff 5 nm of Cr/60 nm of Au to produce a high contrast x-ray mask with narrow lines. This mask will be used to expose PMMA on a plating base.

(26) using the mask produced in step 25, expose and develop ~ 0.25 to 0.3 μm PMMA on a plating base, on ~ 1.5 μm polyimide on a silicon wafer;

(27) "plasma-ash" the developed sample in oxygen for 5 seconds, to remove any organic contamination;

(28) electroplate gold in between the PMMA lines. Plating at a rate of ~ 10 to 20 nm/min gives the most uniform results.

(29) dissolve the PMMA in chlorobenzene;

(30) "plasma-ash" for 60 seconds in an oxygen plasma to remove any residual PMMA;

(31) fabricate this structure into an x-ray mask by using the procedure outlined in Appendix C.

REFERENCES

1. Miller, J.D. Physics Today, July 1976, p. 39.

2. Williams, R.C. and Smith, H.I. Elect. Lett 8, 401 (1972).

3. Yariv, A. Sci. Amer. 240, 64 (1979).

4. Yariv, A. and Nakamura, M. IEEE J. Quantum Electron. QE-13, 233 (1977).

5. Beuermann, K.P.; Lenzen, R. and Bräuninger, H. App. Optics 16(5), 1425 (1977).

6. Gursky, H. and Zehnpfenning, T. App. Optics 5(5). 875 (1966).

7. Giacconi, R.; Reidy, W.P.; Vaiana, G.S.; van Speybroeck, L.P. and Zehnpfenning Space Sci. Rev. 9, 3-57 (1969).

8. Canizares, C.R.; Clark, G.W.; Bardas, D. and Markert, T. SPIE 106, X-ray Imaging, 154 (1977).

9. Flanders, D.C.; Shaver, D.C.; Hawryluk, A.M. and Smith, H.I. Annals of the New York Academy of Sciences 342, 203-212 (1980).

10. Bräuninger, H.; Kraus, H.; Dangschat, H.; Beuermann, K.P.; Predehl, P. and Trümper, J. App. Optics 18(20), 3502 (1979).

11. Predehl, P.; Beuermann, K.P. and Bräuninger, H. App. Optics 19(2), 190 (1980).

12. Schnopper, H.W. et al. App. Optics 16(4), 1088 (1977).

13. Flanders, D.C. and White, A.E. J. Vac. Sci. and Technol., Nov./Dec. 1981.

14. Johnson, L.F. and Ingersoll, K.A. App. Phys. Lett 38(7), 532 (April 1981).

15. Delvaille, J. et al. Nuclear Instruments and Methods 172 (1980).

16. American Institute of Physics Handbook, 2nd edition, D.E. Grey, consulting editor. McGraw-Hill, 1963.

17. Hagemann, H.J.; Gudst, W. and Kunz, C. J. Opt. Soc. Am. 65, 742 (1975).

18. Smith, H.I. Proc. of the IEEE, 1361 (October 1974).

19. Schmahl, G. and Rudolph, D. Progress in Optics XIV, E. Wolf, ed. North Holland, 1976.

20. Smith, H.I. Proc. Symp. on Etching for Pattern Definition; H.G. Hughes and M.J. Rand, eds. (The Electrochemical Society, 1976).

21. Lehmann, H.W. and Widmer, R. J. Vac. Sci. and Technol. 15(2), 319 (1978).

22. Flanders, D.C. J. Vac. Sci. and Technol. 16(6), Nov./Dec. (1979).

23. Smith, H.I. and Flanders, D.C. Japan. J. App. Phys. 16 (1977); Supplement 16-1, pp. 61-65.

24. Smith, H.I.; Spears, D.L. and Bernacki, S.E. J. Vac. Sci. Technol. 10, 913, Nov/Dec (1973); Bernacki, S.E., Ph.D. Thesis, Harvard University, 1975.

25. Spears, D.L. and Smith, H.I. Electron. Lett, 8, 102 (1972).

26. Mayden, D.; Coquin, G.H.; Maldonado, V.R.; Somekh, S.; Lou, D.Y. and Taylor, G.N. IEEE Trans. Electron Devices ED-22, 429 (1975).

27. Romankiw, L.T. Proceedings of the Symposium on Etching for Pattern Definition, H.G. Hughes and M.J. Rand, eds., The Electrochemical Society, c 1976; Romankiw, L.T.; Hatzakis, M. and Castellani, E.E. Electrochemical Soc. Spring Meeting, Extended Abstract No. 208, San Francisco, May 12, 1974.

28. Flanders, D.C.; Hawryluk, A.M. and Smith, H.I. J. Vac. Sci. and Technol. 16(6), 1949, Nov./Dec. (1979).

29. Hawryluk, A.M.; Ceglio, N.M.; Price, R.H.; Melngailis, J. and Smith, H.I. J. Vac. Sci. and Technol., Nov./Dec. (1981).

30. Flanders, D.C., Ph.D. dissertation, Massachusetts Institute of Technology, 1978.

31. Henke, B.L. and Ebisu, E.S. Advances in X-ray Analysis, vol. 17 (Plenum Press, New York, 1974), p. 150.

32. Woodhouse, J.B.; Fields, A.L.A. and Bucklow, I.A. J. Phys. D. App. Phys. 7, 483-489 (1974).

33. Bassous, E.; Feder, R.; Spiller, E. and Toplian, J. Solid State Technol. 19(9), 55-58 (1976).

34. Hecht and Zajac Optics, Addison-Wesley, New York, 1974.

35. Mertz, L. Transformations in Optics, John Wiley & Sons, New York, 1966.

36. Flanders, D.C. and Smith, H.I. J. Vac. Sci. Technol. 15, 995 (1978).

37. Shank, C.V. and Schmidt, R.V. App. Phys. Lett 23, 154 (1973).

38. Efremow, N.N.; Economou, N.P.; Bezjian, K.; Dana, S.S. and Smith, H.I. J. Vac. Sci. Technol., Nov./Dec. (1981).

39. Lin, B.J. IBM J. Res. Develop., 213 (May, 1976).

40. Hawryluk, A.M.; Ceglio, N.M.; Price, R.H.; Melngailis, J. and Smith, H.I. Proceedings of the Low Energy X-Ray Diagnostics Conference, D. Attwood, ed. Monterey, CA, June 1981.

41. Andersen, C.A. The Electron Microprobe, T.P. McKinley, K.F.J. Heinrich and D.B. Wittry, eds. (Wiley, New York, 1966).

42. Feder, R.; Spiller, E. and Topalian, J. J. Vac. Sci. Technol. 12, 1332 (1975).

43. Harris, R.A. J. Electrochem. Soc. 120, 270-274 (1973).

44. Spiller, E. et al. IBM Research Report, R.C. 5675 (#24437) Physics (General), October 1975.

45. Hiraoka, H. IBM J. Res. Develop. 21, 121-131 (1977).

46. Hawryluk, R.J., Ph.D. dissertation, Massachusetts Institute of Technology, May 1974; also, Technical Report #511, Lincoln Laboratory.

47. The Kearns Group, Stamford, CT.

48. Woodson and Melcher, Electromechanical Dynamics, John Wiley and Sons, New York, 1968.

49. Wells, O.C. Scanning Electron Microscopy, McGraw-Hill, New York, 1974.

50. Oxy Metal Industries, Nutley, New Jersey.

51. DeGraff, P.D. and Flanders, D.C. J. Vac. Sci. Technol. 16(6), 1906 Nov./Dec. (1979).

52. Born and Wolf Principles of Optics, 5th Ed., Pergamon Press, 1975.

53. Price, R. Proceedings of the Low Energy X-Ray Diagnostics Conference, D. Attwood, ed. Monterey, CA, June 1981.

54. Henke, B. and Tester, M.A. Advances in X-Ray Analysis, vol. 18, W.L. Pickles et al., eds.

55. Handbook of Spectroscopy, vol. 1, J.W. Robinson, ed. CRC Press.

56. Flanders, D.C. App. Phys. Lett. 36(1), 94 (1980).

57. Ceglio, N.M.; Stone, G.F. and Hawryluk, A.M. J. Vac. Sci. Technol. Nov./Dec. (1981).

58. Wolter, H. Ann. Physik 10, 94 (1952).

59. Arakawa, E.T.; Caldwell, P.J. and Williams, M.W. "Soft X-ray Transmission Gratings", Periodic Structures, Gratings, Moire Patterns and Diffraction Phenomena, Proc. of SPIE 240, 52; C.H. Chi, E.G. Loewen and C.L. O'Bryan, eds., San Diego, CA, July 29 - August 1, 1980. c 1981, SPIE.

60. Shattenburg, M. (Physics Department, MIT), private communication.

61. Ceglio, N.M.; Roth, M. and Hawryluk, A.M. Proceedings of the Low Energy X-Ray Diagnostics Conference, D. Attwood, ed. Monterey, CA, June 1981.

62. Ceglio, N.M.; Price, R.H. and Hawryluk, A.M. Proceedings of the High Resolution Soft X-Ray Optics Conference; SPIE Proceedings 316, E. Spiller, ed. Brookhaven National Laboratory, Upton, New York, November 18-20, 1981.

63. Ceglio, N.M. Proceedings of the Low Energy X-Ray Diagnostics Conference, D. Attwood, ed. Monterey, CA, June 1981.

64. Bjorklund, G.C.; Harris, S.E. and Young, J.E. Appl. Phys. Lett 25, 451-452 (1974).

65. Winthrop, J.T. and Worthington, C.R. J. Opt. Soc. Am. 55(4), 373 (1965).

66. Rogers, G.L. Brit. J. Appl. Phys. 14, 657 (1963).

67. Hiedemann, E.A. and Breazeale, M.A. J. Opt. Soc. Am. 49(4), 372 (1959).

68. Cowley, J.M. and Moodie, A.F. Proc. Phys. Soc. (London) 70, 486-513, 1957.

69. Goodman, J.W. Introduction to Fourier Optics, McGraw-Hill, 1968.

70. Lin, B.J. J. Opt. Soc. Am. 62, 976 (1972).

71. Lin, B.J. Fine Line Lithography, R. Newmann, ed. Elsevier North-Holland, 1981.

72. Also known as Kodak-Chrome Etch, Eastman Kodak, Rochester, New York.

73. Bean, K.E. IEEE Trans. Elect. Devices ED25, 1185 (1978).

74. Corning Glass Works, Danville, VA.

75. Shaver, D.C.; Flanders, D.C.; Ceglio, N.M. and Smith, H.I. J. Vac. Sci. Technol. 16(6), 1626, Nov/Dec (1979).

76. Ceglio, N.M. Annals of the New York Academy of Sciences 342, 65 (1980).

77. Rudolph, D. and Schmahl, G. Annals of the New York Academy of Sciences 342, 94 (1980).

78. Barbee, T.W. Jr. Proceedings of the Low Energy X-Ray Diagnostics Conference, D. Attwood, ed. Monterey, CA, June 1981.

79. Spiller, E. Proceedings of the Low Energy X-Ray Diagnostics Conference, D. Attwood, ed. Monterey, CA, June 1981.

80. Esschem Corp., Essington, PA.

81. Selas Flotronics, Spring House, PA.

82. E.I. duPont de Nemours & Co., Wilmington, DE.

83. Tra-Con, Medford, MA.

84. Rudolph, D. and Schmahl, G. Umscheu Wiss. Tech. 67(7), 225 (1967).